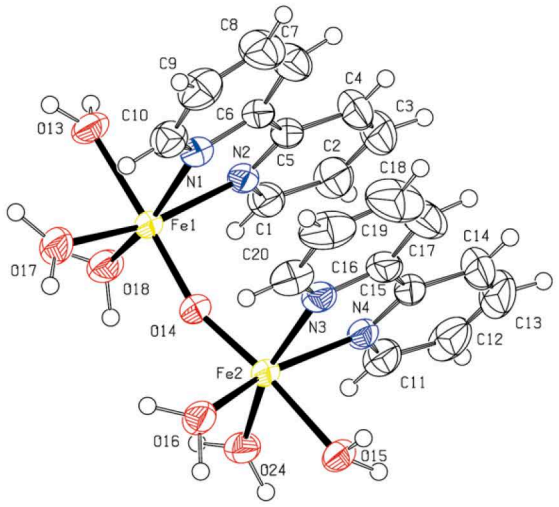

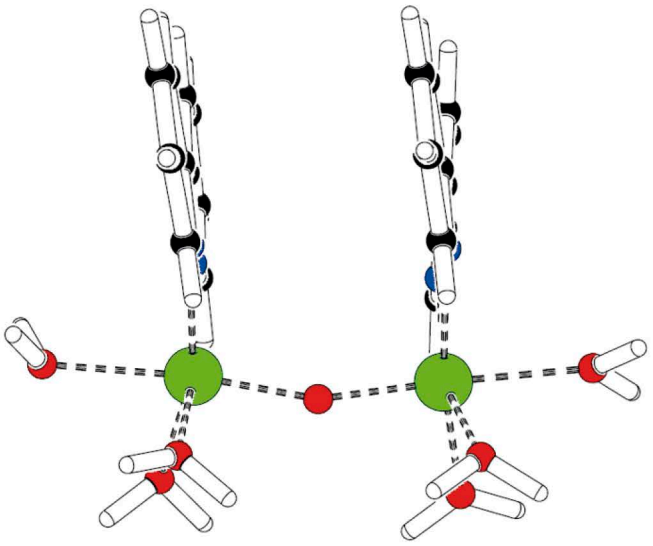

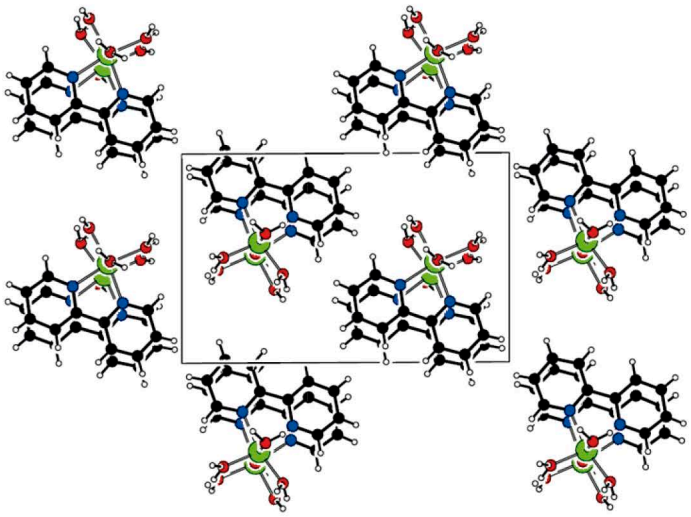

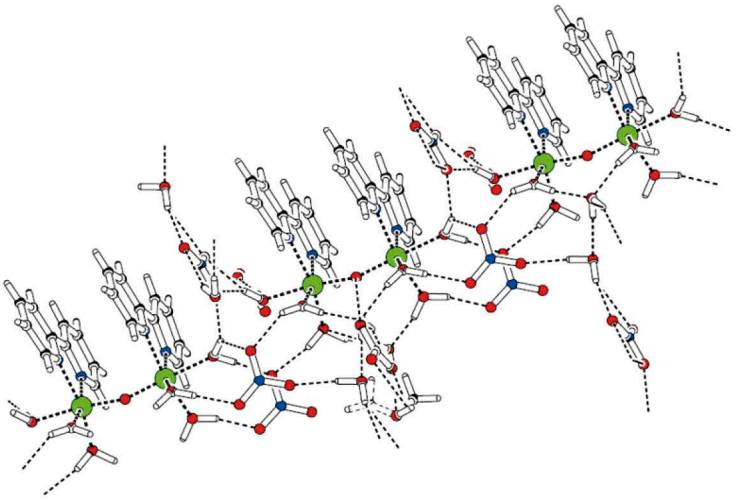

Rita Mendes da Silva

Physical Properties of Metallic Complexes

This dissertation is submitted for the degree of Master of Physics,
Supervised by Prof. Dr. Manuela Silva and presented to the Department of Physics of the Faculty of Science and Technology
University of Coimbra

September 2018

· U C ·

Universidade de Coimbra

Physical Properties of Metallic Complexes

Rita Mendes da Silva

Supervisor: Prof. Dr. Manuela Silva

Department of Physics
University of Coimbra

This dissertation is submitted for the degree of
Master of Physics

September 2018

Dedico esta tese aos meus dois irmãos mais novos, Sofia e Alvarino, que apesar de todas as brigas e discussões continuamos sempre a gostar uns dos outros. Amo-vos muito.

Agradecimentos

Em primeiro lugar, gostaria de agradecer à Professora Doutora Manuela Ramos Silva pelo seu apoio e orientação deste trabalho. Obrigado pela motivação em querer descobrir algo novo que pudesse ter ótimas aplicações.

Gostaria também de agradecer ao Professor Doutor Pedro Sidónio pela sua simpatia e disponibilização na parte experimental da difração em pó.

Ao Doutor Bruno Cardoso Vieira e ao Doutor João Carlos Waerenborgh pela sua importante colaboração nas medições de espectrocopia Mössbauer de uma das amostras realizadas no Centro Técnológico Nuclear (CTN) em Lisboa.

Quero também agradecer o acesso aos instrumentos do Departamento de Química e do acesso ao Difractómetro de Raios-X da Universidade de Aveiro para a análise de duas amostras.

Agradeço ainda o acesso aos instrumentos da plataforma TAIL-UC, financiados pelo programa QREN-Mais Centro ICT 2009-02-012-1890.

À Maria pela troca de ideias e sugestões e pela preparação experimental da espectroscopia UV-Visível.

À Marta, pela amizade e ajuda na parte experimental de Magnetometria, assim como em todos os momentos mais stressantes.

Às minhas amigas da ilha, Mariana e Adriana, obrigada pelos tantos anos de amizade.

Ao David, Ricardo e Tomás por estes dois últimos anos de ótimos momentos partilhados.

À Ana Maria, Fátima, Rita e Shea. Estes cinco anos passaram bastante rápido mas encontrei aqui amigas que ficaram para a vida.

Gostaria de agradecer às minhas duas avós pelo seu apoio icondicional. Espero que estes anos de estudo fora de casa tenham compensado as constantes preocupações e saudades.

Aos meus 26 primos, tios e tias pelas boas memórias de infância até hoje. E finalmente aos meus pais, pois sem o seu financiamento isto não teria sido possível.

Abstract

The field of Molecular Magnetism starts slowly and discreetly, in the 50s, with the investigation of the "anomalous" magnetic properties of dinuclear copper paddlewheel complexes. Unpredictably, the field evolved to extraordinary challenges and discoveries in coordination chemistry, in condensed matter physics, and even in molecular electronics, being the discovery of hysteresis in manganese acetate ($[Mn_{12}O_{12}(CH_3COO)_{16}(H_2O)_4] \cdot 2CH_3COOH \cdot 4H_2O$), with a quantum tunnelling between some of the magnetic substates, one of the most interesting breakthroughs.

This thesis reports the study of four transition metal coordination compounds, namely of their magnetic behaviour, using powerful techniques in experimental physics such as X-ray diffraction, Magnetometry, Mössbauer Spectroscopy. The metal ions, Fe^{3+} and Cu^{2+}, are bridged, coordinated or chelated by organic ligands (pyridine, bipyridine and phenanthroline), and arranged in low-dimensional elements like monomers, dimers and chains.

For one of the compounds, dichloro-bis(pyridine)-copper(II), a broad peak in the magnetisation is seen as the temperature of the sample decreases, accounting for a strong antiferromagnetic interaction between the neighbouring metal ions, bridged by the negative chlorine ions.

For another compound, a new iron coordination compound, not yet reported in the literature, in which two crystallographically distinct metal ions are assembled in dimers, Mössbauer Spectroscopy down to 4K was used to follow the possible onset of the magnetic ordering. The measured isomer shifts and the quadrupole splitting, are consistent with Fe^{3+}, S=5/2, octahedrally coordinated by six atoms.

Resumo

A área do Magnetismo Molecular começou discretamente nos anos 50 do século passado com a investigação do comportamento magnético, "anómalo", do acetato de cobre hidratado. Inesperadamente, esta área evoluiu revelando novos desafios para a Química de Coordenação e especialmente revelando novos fenómenos físicos como o tunelamento quântico da magnetização, sendo o acetato de manganésio ($[Mn_{12}O_{12}(CH_3COO)_{16}(H_2O)_4]\cdot 2CH_3COOH\cdot 4H_2O$) um dos compostos mais estudados neste campo do saber. Esta tese descreve o estudo de 4 compostos contendo metais de transição, nomeadamente o estudo das suas propriedades magnéticas, usando técnicas poderosas como a difração de Raios-X, a Magnetometria ou a Espectroscopia de Mössbauer. Nestes compostos, os iões metálicos, Fe^{3+} ou Cu^{2+}, são ligados ou coordenados por moléculas orgânicas neutras contendo anéis aromáticos (piridina, bipiridina e fenantrolina), formando, no sólido, elementos de baixa dimensão como monómeros, dímeros e cadeias.

A magnetização de um dos compostos (contendo a molécula de piridina e os iões de cloro e cobre) revela um pico largo na sua dependência com a temperatura, característico de um arranjo antiferromagnético dos spins.

Outro composto, do qual não existe relato na literatura científica actual, um dímero de Fe^{3+} com uma ponte oxo, mostra um estado de spin elevado para cada um dos iões, consistente com uma pequena separação de níveis causada pelo campo cristalino em ambientes octaédricos.

Table of contents

List of figures

List of tables

Nomenclature

Acronyms / Abbreviations

Δ	Ligand field splitting parameter
CFE	Counter-Flow Heat Exchanger
CFT	Crystal Field Theory
FC	Field Cooled
IS	Isomer Shifts
LFSE	Ligand Field Stabilization Energy
P	Pairing Energy
PPMS	Physical Property Measurement System
QS	Quadrupole Splitting
UV-Vis	Ultraviolet Visible
VSM	Vibrating Sample Magnetometer
XRD	X-ray Diffration
ZFC	Zero Field Cooled

Chapter 1

Introduction

1.1 Transition Metals

Transition elements, like all other naturally occurring elements, originate from nuclear reactions occurring within stars and supernovae.

Humanity has known transition metals for millenia. Archaeological evidences were found that indicated that the Sri Lanka habitants in the first millennium B.C. used wind for iron smelting furnaces in the production of steel [1]. The first metals to be discovered were those that exist in their elemental form such as silver, copper and gold. Soon, it was discovered that metals could also be obtained by separating them from the minerals through heating or reduction by hot charcoal. After aluminum, iron is the most abundant metal in the Earth's crust (6.2% in mass). Some of the most important iron ores are pirite (FeS_2), hematite (Fe_2O_3), siderite ($FeCO_3$) and magnetite (Fe_3O_4). The metalurgic process involves chemical reduction of the minerals through carbon [2].

$$3Fe_2O_3(s) + CO(g) \longrightarrow 2Fe_3O_4(s) + CO_2(g) \tag{1.1}$$

$$Fe_3O_4(s) + CO(g) \longrightarrow 3Fe_3O(s) + CO_2(g) \tag{1.2}$$

$$FeO(s) + CO(g) \longleftrightarrow Fe(l) + CO_2(g) \tag{1.3}$$

Copper is a rare element (6.8×10^{-3}% mass in the Earth's crust) and it can be found in its natural form or in copper ores such as calcopirite ($CuFeS_2$).

$$2CuFeS_2(s) + 4O_2(g) \longrightarrow Cu_2S(s) + 2FeO(s) + 3SO_2(g) \tag{1.4}$$

$$Cu_2S(s) + O_2(g) \longrightarrow 2Cu(s) + SO_2(g) \tag{1.5}$$

Copper is a good electric and thermal conductor and is used in alloys, electric cables, plumbing and coins.

Fig. 1.1 Some examples of transition metals.

The knowledge of transition metals increased in the 18th and 19th centuries through the discovery of chemical reactions and the improved separation methods of compounds. The end of the 19th and beginning of the 20th centuries brought more understanding of radioactivity and the nuclear and atomic structure.

The transition elements occupy groups 3 to 12 in the central region of the periodic table. One of the differences between the transition metals and other elements is that their d orbitals are partially occupied by electrons. This attribute is responsible for their magnificent properties, including a distinct coloration, formation of paramagnetic compounds, catalytic activity and an enormous tendency to form ionic complexes. They also play an important role in animals and plants.

Table 1.1 Functions of some transition metals in plants [3].

Micronutrients	Functions in higher plants
Manganese	Activates decarboxylase, dehydrogenase, and oxidase enzymes; important in photosynthesis, nitrogen metabolism, and nitrogen assimilation.
Iron	Present in several peroxidase, catalase, and cytochrome oxidase enzymes; found in ferredoxine which participates in oxidation reduction reactions; important in chlorophyll.
Cobalt	Essential for nitrogen fixation; found in vitamin B_{12}.
Nickel	Required as a component of the urease enzyme.
Zinc	Present in several dehydrogenase, proteinase and peptidase enzymes; promostes growth hormones and starch formation; promotes seed maturation and production.
Molybdenum	Present in nitrogenase (nitrogen fixation) and nitrate reductase enzymes; essential for nitrogen fixation and high oxidizing.
Boron	Activates certain dehydrogenase enymes; facilitates sugar translocation and synthesis of nucleic acids and plant hormones; essential for cell division and development.
Copper	Present in laccase and several other oxidase enzymes; important in photosynthesis, protein and carbohydrate metabolism, and probably nitrogen fixation.

1.2 Thesis Objectives

As the transition metals have so many applications both in industry and in medicine, the goal of this project was to discover new inorganic materials, using transition metals and organic ligands, and study their physical and chemical properties.

As applications are concerned, 3d metals can be used for gas separation [4]; environmentally friendly dyes [5]; as catalysts [6]; as additives for plastics [7]; as anti-cancer agents [8]; as conductive materials [9]; as magnetic materials [10], etc.

Chapter 2 of this dissertation is dedicated to the general physical and chemical properties of transition metals. It introduces concepts such as oxidation number, coordination compounds geometry and Crystal Field Theory. Chapter 3 explains the methods and calculations for crystal structure determination and refinement as this is a very important topic for all crystallographers. In chapter 4 molecular magnetism and its importance for characterizing

materials are discussed. Concepts such as the Brillouin Function and the Curie Law are also presented in this chapter. The chapter 5 consists of a description of the experimental methods, including the equipment used for the synthesis and characterization measurements. Chapter 6 includes the experimental technique used in the synthesis and growth of crystals. The reagents and solvents used in this project and their respective proportions are also mentioned. In chapter 7, a presentation and discussion of the results is reported. Finally, in chapter 8, the conclusions and suggestions for further work are presented.

Chapter 2

Physical and Chemical Properties of Complex Transition Metals

2.1 Coordination Compounds

A complex is a combination of a central metal atom, called the Lewis acid, with a number of ligands, known as Lewis bases. A Lewis base is a substance capable of donating one or more electron pairs. All ligands have at least one pair of non-shared valence electrons, so they play the role of the Lewis bases. On the other hand, the transition metal atom acts as a Lewis acid, accepting and sharing electron pairs from the Lewis bases. Thus, metal-ligand bonds are generally covalent coordinate bonds.

The number of donor atoms bonded to the metal center is known as the coordination number of a metal ion in a complex. For example, the coordination number of Cu^{2+} in $[Cu(NH_3)_4]$ is 4 and the coordination number in Fe^{3+} in $[Fe(CN)_6]^{3-}$ is 6.

2.1.1 Coordination Compounds Structure

In coordination compounds, the ligands can be arranged in many ways around the central ion. Due to this, they can exhibit quite different chemical and physical properties. Figure 2.1 shows that the geometric structure and the coordination number of the central atom are related.

Table 2.1 Coordination number of a complex and their possible geometries [2, 11].

Coordination Number	Structure
2	Linear
3	trigonal planar or pyramidal
4	Tetrahedral or square-planar
6	Octahedral

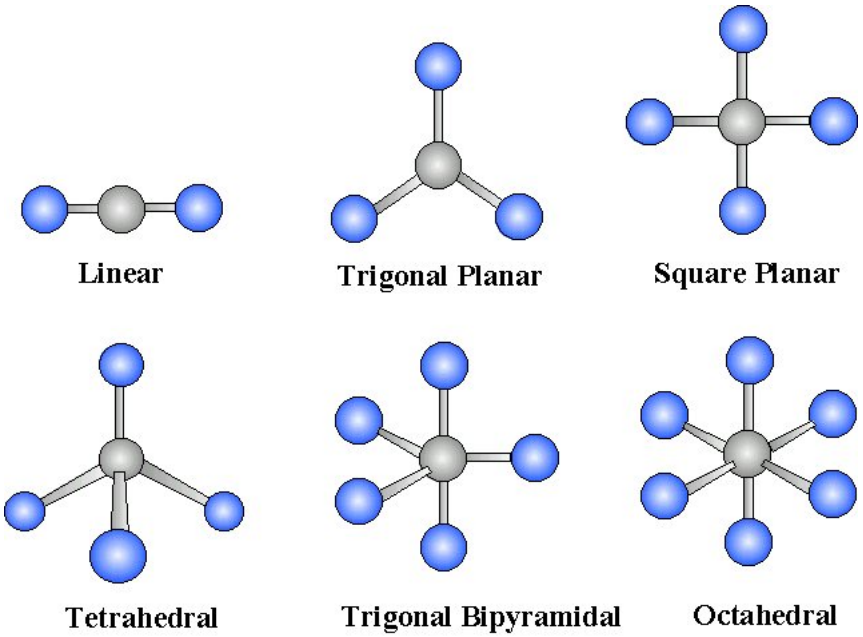

Fig. 2.1 Common geometries of complex ions [12].

2.2 Oxidation State

The oxidation state is a formal physical concept of an element that corresponds to the charge that an atom would have if the more electrically negative atom in the bond completely acquired the two electrons of the bond. For example, the metals Cu^{2+} and Fe^{3+} have oxidation state +2 and +3, respectively. The transition metals exhibit various oxidation states in their compounds.

The highest oxidation state for a transition metal is +7 for manganese ($4s^2 3d^5$). For the elements which are to the left of Mn (Fe to Cu), the oxidation numbers are lower. Generally, the transition elements exhibit oxidation states higher in compounds with very electrically negative elements, such as oxygen and fluorine, V_2O_5, CrO_3 and Mn_2O_7.

In coordination compounds, the net charge of the complex ion is the sum of the central atom charge and the ligands that surround it. For example, in $[PtCl_6]^{2-}$ each chloride ion has an oxidation number of -1, so the oxidation number of Pt must be +4.

Table 2.2 The oxidation state of the transition metals of the first series. The most stable oxidation numbers are in bold [2].

Sc	Ti	V	Cr	Mn	Fe	Co	Ni	Cu
				+7				
			+6	+6	+6			
		+5	+5	+5	+5			
	+4	+4	+4	**+4**	+4	+4		
+3	+3	+3	**+3**	+3	**+3**	**+3**	+3	+3
	+2	+2	+2	+2	**+2**	**+2**	**+2**	**+2**
								+1

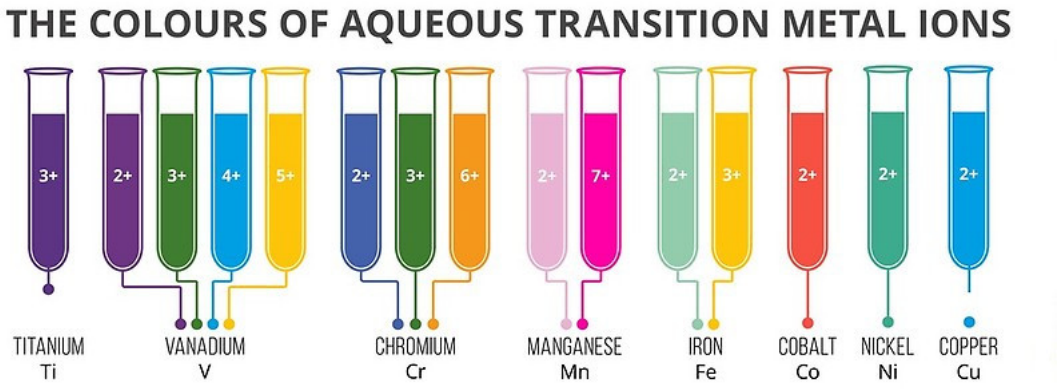

Fig. 2.2 Some examples of transition metals's color and oxidation number [13].

2.3 Crystal Field Theory

The color and the magnetic properties of complex metals can be understood through crystal field theory. This theory explains the bonds in complex ions in terms of electrostatic forces. In a complex ion, there are two types of electrostatic interactions: one is the attraction between the positive metallic ion and the ligands negatively charged and the other is the

electrostatic repulsion between the non-shared pairs in the ligands and the electrons in the d orbitals of the metal.

2.3.1 Crystal Field Splitting in Octahedral Complexes

The d orbitals have different orientations, but in the absence of an external perturbation they all have the same energy. In an octahedral complex, one atom of a metal is surrounded by six pairs of non-shared electrons, so the five d orbitals feel an electrostatic repulsion.

The orientation of d orbitals is related with the electrostatic repulsion intensity. The orbitals lobes of $d_{x^2-y^2}$ and d_{z^2} point directly to the octahedron vertices, where the non-shared electron pairs are. Therefore, a electron residing in one of these orbitals will experience a larger repulsion from the ligands than an electron in an orbital d_{xy}.

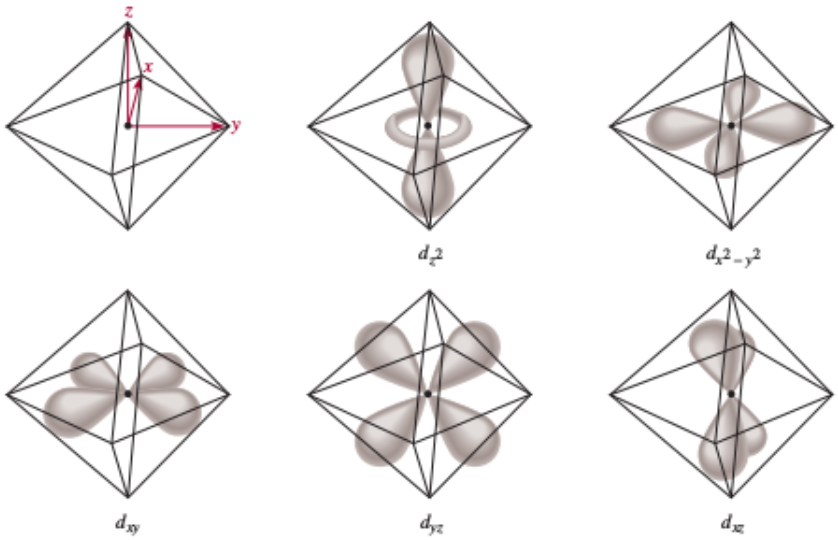

Fig. 2.3 The five d orbitals in an octahedron [2].

As a result of these metal-ligand interactions, the five d orbitals in an octahedral complex are split in two energy levels: one higher level with two orbitals ($d_{x^2-y^2}$ and d_{z^2}) that have the same energy and another, lower, level with three equally energetic orbitals (d_{xy}, d_{yz} and d_{xz}).

The splitting of the crystal field, known as Δ, is the energy difference between the two d orbital groups of a metal atom when the ligands are present. The magnitude of Δ depends on the nature of the metal and the ligands.

The ligand-field splitting parameter, Δ_o, varies systematically with the identity of the ligand. For example, in the series of complexes $[CoX(NH_3)_5]^{n+}$ with X = I^-, Br^-, Cl^-, H_2O, and NH_3, the colors range from purple (X = I^-) through pink ($X = Cl^-$) to yellow

($X = NH_3$). This indicates that the energy of the less energetic electronic transition increases as the ligands are varied along the series with the ligand order being the same regardless of the identity of the metal ion. As a result, ligands can be arranged in a spectrochemical series in which Δ_o increases:

$$I^- < Br^- < S^{2-} < SCN^- < Cl^- < NO_2^- < N^{3-} < F^- < OH^- < C_2O_4^{2-} < O^{2-} <$$

$$H_2O < NCS^- < CH_3C \equiv N < py < NH_3 < en < bpy < phen < PPh_3 < CN^- < CO$$

The series indicates that, for the same metal, the optical absorption of the cyano complex will occur at an higher energy than that of the corresponding chloride complex. For example, CO is considered a strong-field ligand, whereas one that gives rise to a low-energy transition, such as Br^-, is referred to as a weak-field ligand. Δ_o also depends on the identity of the central metal ion and it can be arranged in a spectrochemical series:

$$Mn^{2+} < Ni^{2+} < Co^{2+} < Fe^{2+} < V^{2+} < Fe^{3+} < Co^{3+} < Mo^{3+} < Rh^{3+} < Ru^{3+} < Pd^{4+} <$$

$$Ir^{3+} < Pt^{4+}$$

The value of Δ_O increases with increasing oxidation state of the central metal ion and along a group. The higher oxidation states reflect the smaller size of more highly charged ions and the consequently shorter metal-ligand distances and stronger interaction energies. The increase along a group reflects the larger size of the 4d and 5d orbitals compared with the compact 3d orbitals and the consequent stronger interactions with the ligands.

2.3.2 Ligand-Field Stabilization Energies

The d orbitals in a complex do not have all the same energy, so the ground-state electron configuration cannot be known with certainty. In an octahedral complex, the first three d electrons of a $3d^n$ complex occupy separate t_{2g} non-bonding orbitals and do so with parallel spins. The ions Ti^{2+} have electron configurations $3d^2$ and the ions V^{2+} have electron configurations $3d^3$. The energy of a t_{2g} orbital relative to the barycentre of an octahedron ion is $-0.4\Delta_o$ and the complexes are stabilized by $2 \times 0.4\Delta_o = 0.8\Delta_o$ for Ti^{2+} and $3 \times 0.4\Delta_o = 1.2\Delta_o$ for Vn^{2+}. This stability relative to the barycentre is called the ligand field stabilization energy (LFSE).

The ion Cr^{2+} has an electron configuration of $3d^4$. One of the four electrons may enter one of the t_{2g} orbitals and pair with the electron already there. In this case, it experiences a

strong Coulombic repulsion, known as the pairing energy, P. Another alternative is that the electron may occupy one of the e_g orbitals. In this case, even without the pairing energy, the orbital energy is higher. In the case of t_{2g}^4, there is a stabilization of $1.6\Delta_o$ countered by the pairing energy P giving a net LFSE of $1.6\Delta_o - P$. In the case of $t_{2g}^3 e_g^1$ the LFSE is $3 \times 0.4\Delta_o - 0.6\Delta_o = 0.6\Delta_o$, as there is no pairing energy to consider.

If $\Delta_o <$ P, which is called the weak-field case, a lower energy is achieved when the upper orbital is occupied, giving the configuration $t_{2g}^2 e_g^1$. If $\Delta_o >$ P (the strong-field case), a lower energy is achieved by occupying only the lower orbitals, despite the cost of the pairing energy. For this case, the configuration is t_{2g}^4.

Ground-state electron configurations of $3d^1$, $3d^2$ and $3d^3$ complexes are t_{2g}^1, t_{2g}^2 and t_{2g}^3 because there is no competition between the additional stabilization achieved by occupying the t_{2g} orbitals and the pairing energy. There are two possible configurations for $3d^n$ complexes, with n = 4, 5, 6 or 7. Thus, in a strong field, the lower orbitals are occupied preferentially, and in the weak-field, electrons avoid the pairing energy by occupying the higher orbitals. The chemical specie that has a smaller number of parallel electron spins is called a low-spin complex, while one with a large number of parallel electron spins is called a high-spin complex.

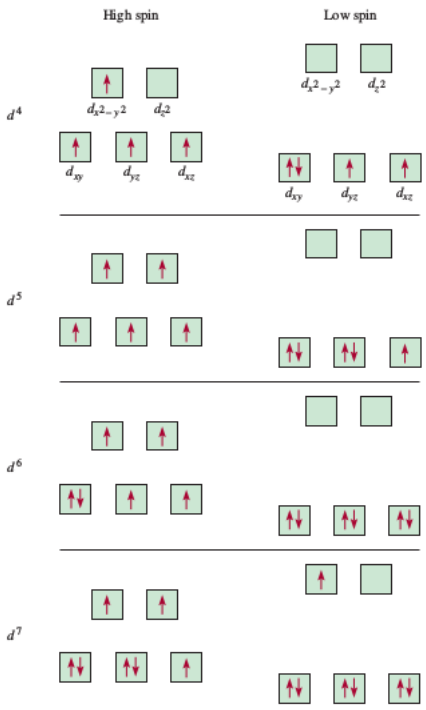

Fig. 2.4 d^4, d^5, d^6 and d^7 orbitals for high-spin and low-spin octahedral complexes [2].

Like the electron configurations of $3d^1$, $3d^2$ and $3d^3$, the ground-state electron configurations of $3d^8$, $3d^9$ and $3d^{10}$ complexes are also unambiguous and they are $t_{2g}^6 e_g^2$, $t_{2g}^6 e_g^3$ and $t_{2g}^6 e_g^4$.

The spin pairing energy (P) and the strength of the crystal field (given by Δ_o) depend on the identity of both the metal and the ligand so it is not possible to indicate with certainty the transition between high-spin and low-spin. For 3d metal ions, low spin complexes commonly occur for ligands that are high in the spectrochemical series while high-spin complexes are common for ligands that are low in the series. The values of Δ_o for complexes of 4d and 5d series metals are typically higher than for the 3d series metals. Pairing energies for the 4d and 5d series metals tend to be lower than for the 3d series metals since their orbitals are less compact and electron-electron repulsions are weaker. As a result, complexes of these metals have electron configurations that are characteristic of strong crystal fields with low spin.

2.3.3 Crystal Field Splitting in Tetrahedral and Square-Planar Complexes

The crystal field theory can also explain the energy levels splitting in tetrahedral and square planar complexes.

In tetrahedral complexes, the orbitals d_{xy}, d_{yz} e d_{xz} are closer to the ligands and so they have more energy than $d_{x^2-y^2}$ and d_{z^2} orbitals. The splitting of a tetrahedral ion is the opposite of the octahedral complexes. The tetrahedral arrangement reduces the magnitude of the metal-ligand interactions, resulting in a lower Δ ($\Delta_t \approx \frac{4}{9}\Delta_o$), as should be expected for complexes with fewer ligands. This can explain why most of tetrahedral complexes form high-spin complexes.

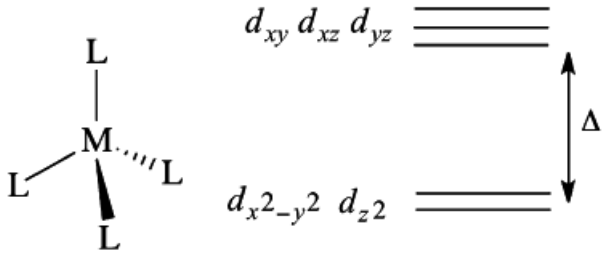

Fig. 2.5 Orbital splitting for a tetrahedral complex [14].

The splitting pattern for square-planar complexes is quite different. Some complexes with four ligands are in a higher energy square planar arrangement despite it being the least sterically demanding arrangement. A square-planar arrangement becomes energetically

favourable when there are eight d electrons and the crystal field is strong enough to favour the low-spin $d_{yz}^2\ d_{zx}^2\ d_{z^2}^2\ d_{xy}^2$ configuration, and the electronic stabilization energy can compensate any unfavourable steric interactions.

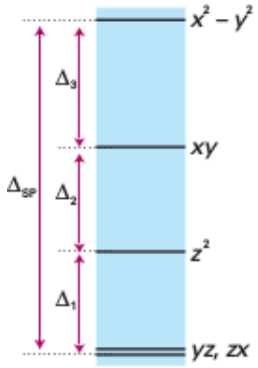

Fig. 2.6 Orbital splitting for a square-planar complex [11].

The square-planar complexes are found in $4d^8$ and $5d^8$ ions like Rh(I), Ir(I), Pt(II), Pd(II) and Au(III). On the contrary, small 3d series metal complexes such as $[NiX_4]$, whereX is an halogen, are mostly tetrahedral because the ligand field splitting parameter is usually small and will not sufficiently compensate for the unfavourable steric interactions. Because the pairing energies for 4d and 5d series metals tend to be lower than for the 3d, this can explain why most of square-planar complexes form low-spin complexes.

2.3.4 The Jahn-Teller Effect

If the ground electronic configuration of a nonlinear complex is orbitally degenerate and asymmetrically filled, then the complex distorts in a way that removes the degeneracy and achieves a lower energy. This phenomenon is known as the Jahn-Teller effect. For example, Mn^{3+} ions, which have a configuration $3d^4$ in an octahedral environment show this kind of behaviour. In contrast, Mn^{4+} ions ($3d^3$) would not show this effect because there is no net lowering of the electronic energy caused by a distortion.

A tetragonal distortion of an octahedron, which is an extension along the z axis and compression along the x and y axes, increases the energy of the $d_{x^2-y^2}$ orbital and lowers the energy of the d_{z^2} orbital. As a result, if one or three electrons occupy the e_g orbitals the tetragonal distortion may be energetically favorable.

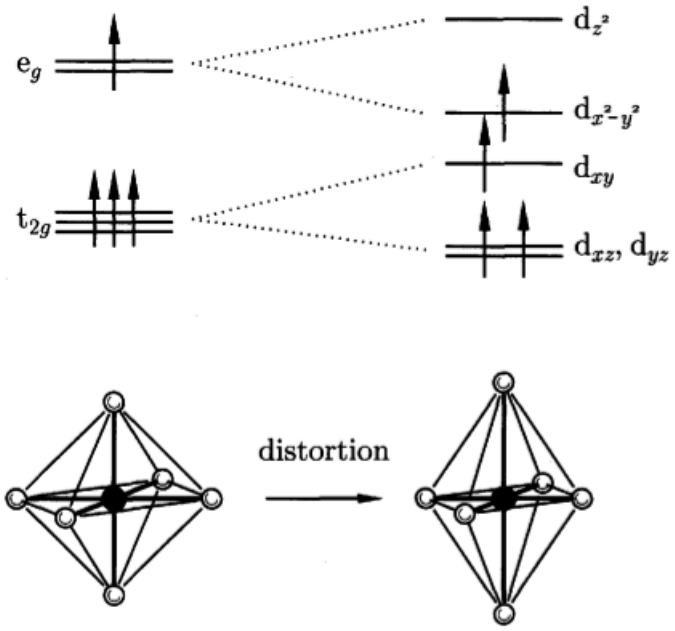

Fig. 2.7 The Jahn-Teller effect for an octahedral complex [15].

Instead of axial elongation and equatorial compression, the degeneracy of an octahedral complex can also be removed by axial compression and equatorial elongation. The distortion that occurs is a matter of energy, not symmetry. On the other hand, because axial elongation weakens two bonds but equatorial elongation weakens four, axial elongation is more common than axial compression. The Jahn-Teller effect is possible for other electron configurations.

For an octahedral complex:

- d^1, d^2, low spin d^4, low spin d^5, high spin d^6 and d^7 configurations.

For a tetrahedral complex:

- d^1, d^3, d^4, d^6, d^8 and d^9 configurations.

2.3.5 Color

White light is a combination of all colors. A substance is black if it absorbs all the visible light that hits it and white or colorless if it does not absorb any light. An object appears green if it reflects every color except red (the complement color of green). This also applies to transmitted light.

When the energy of a photon is equal to the difference between the fundamental and excited state, absorption occurs and one electron is promoted to a higher level. The energy of a photon is given by

$$E = h\nu \tag{2.1}$$

where h represents the Planck constant ($6.63 \times 10^{-34} J \cdot s$) and ν represents the radiation frequency.

The best way to measure the crystal field splitting is to use spectroscopy to determine the wavelength at which light is absorbed. The $[Ti(H_2O)_6]^{3+}$ ion absorbs light in the visible region of the spectrum. The wavelength corresponding to the maximum absorption is 498 nm and this information can be used to calculate the crystal field splitting, Δ:

$$\Delta = \frac{hc}{\lambda} = \frac{6.63 \times 10^{-34} \cdot 3 \times 10^{8}}{498 \times 10^{-19}} \tag{2.2}$$

$$\Delta = 3.99 \times 10^{-19} J \tag{2.3}$$

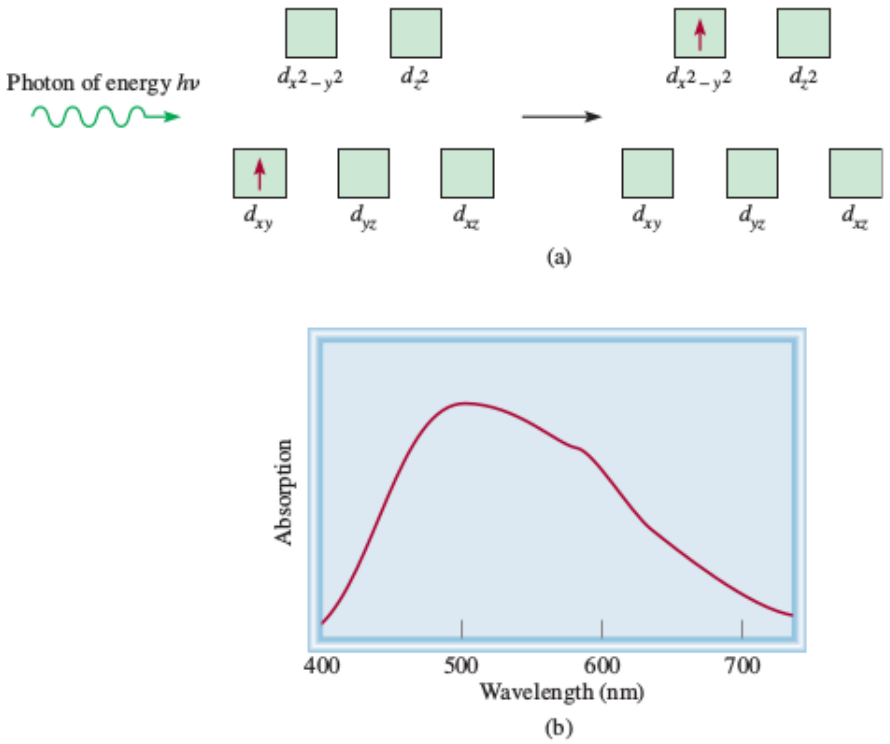

Fig. 2.8 (**a**) Absorption process of a photon. (**b**) Absorption spectrum of $[Ti(H_2O)_6]^{3+}$ ion [2].

$[Ti(H_2)O_6]^{3+}$ absorbs in the yellow region which gives it the purple color (see Fig. 2.8).

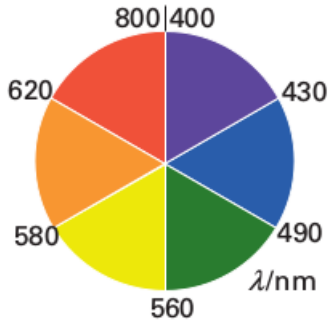

Fig. 2.9 Complementary colors lie opposite of each other in the color wheel [2].

2.3.6 Magnetic Properties

Paramagnetic substances have unpaired spins and are attracted to a magnet. Diamagnetic substances do not contain unpaired spins and are lightly repelled by a magnet.

Ions that have just one d electron are always paramagnetic. However, for an ion with many d electrons, the situation is more complicated. For example, the configuration of Fe^{3+} is [Ar]$3d^5$ and there are two possible ways to distribute the 5 electrons over d orbitals. The high-spin complexes are more paramagnetic than the low-spin complexes.

We can distinguish paramagnetic substances and diamagnetic substances experimentally by magnetometry. The magnitude of the paramagnetism is usually described in terms of the magnetic dipole moment. If the magnetic dipole of the complex is high, the substance will be more paramagnetic. The magnetic properties of a complex ion depend on the number of the unpaired electrons because the net electron spin angular momentum survives and gives rise to spin-only paramagnetism. The spin-only magnetic moment, μ, of a complex with total spin quantum number S is

$$\mu = 2(S(S+1))^{1/2}\mu_B \tag{2.4}$$

where μ_B is the Bohr magneton, $\mu_B = e\hbar/2m_e = 9.27 \times 10^{-4} J\ T^{-1}$. Since $S = \frac{1}{2}$N where N is the number of the unpaired electrons, each with spin $s = \frac{1}{2}$, we can rearrange the equation:

$$\mu = [N(N+1)]^{1/2}\mu_B \tag{2.5}$$

This measurement can be used to distinguish between high spin and low spin complexes, such as the magnetic measurements of a d^6 complex configuration. Through these measure-

ments, it can be easy to distinguish between a high spin $t_{2g}^4 e_g^2$ (N = 4, S = 2, $\mu = 4.90\mu_B$) and a low spin t_{2g}^6 (N = 0, S = 0, μ = 0) configuration.

The experimental values for most 3d complexes and some 4d complexes are close to the values of the spin-only predictions. As a result, it becomes possible to identify the number of unpaired electrons and assign the ground-state configuration. For example, $[Fe(OH)_2^6]^{3+}$ is paramagnetic with a magnetic moment of 5.9 μ_B. As shown in the table, this value is consistent with there being five unpaired electrons $\left(N = 5 \text{ and } S = \frac{5}{2}\right)$, which implies a high spin $t_{2g}^3 e_g^2$ configuration.

Table 2.3 Spin-only magnetic moments for some transition metals [11].

Ion	Electron Configuration	S	μ/μ_B Calculated	Experimental
Ti^{3+}	t_{2g}^1	$\frac{1}{2}$	1.73	$1.7-1.8$
V^{3+}	t_{2g}^2	1	2.83	$2.7-2.9$
Cr^{3+}	t_{2g}^3	$\frac{3}{2}$	3.87	3.8
Mn^{3+}	$t_{2g}^3\ e_g^1$	2	4.90	$4.8-4.9$
Fe^{3+}	$t_{2g}^3\ e_g^2$	$\frac{5}{2}$	5.92	5.9

The electronic state of the metal ion can also change with the temperature, pressure, light, etc. This leads to a change from high spin to low spin and consequently, a change in the magnetic moment. These complexes are called spin-crossover complexes.

Chapter 3

Crystal Structure Refinement

3.1 Diffraction Intensity

3.1.1 Electron Scattering

The scattering process of an X-ray beam by electrons gives the diffracted beam a certain degree of polarization. As a result, at a given point, the intensity of the wave scattered by an electron varies with the angle between the incident beam and the scattered beam, according to the Thomson equation,

$$I_e = I_0 \left(\frac{e^4}{m^2 c^4 r^2} \right) \left(\frac{1 + \cos^2 2\theta}{2} \right) \tag{3.1}$$

where I_0 is the intensity of the incident beam, e and m are the charge and the mass of the electron, respectively, c is the speed of light in the vacuum and r is the distance between the electron and the point considered. The expression $\left(\frac{1+\cos^2 2\theta}{2} \right)$ is known as the polarization factor.

3.1.2 Atom Scattering

When an X-ray beam strikes an atom, the atomic electrons absorb the energy of the beam and then scatter it in all directions. These electrons are located around the atomic nucleus, forming an electronic cloud. Therefore, the scattering is in fact due to the constituent electrons of this cloud, instead of the atom as whole. So, the regions of the electronic cloud in which there are phase differences between the scattered rays must be taken into account.

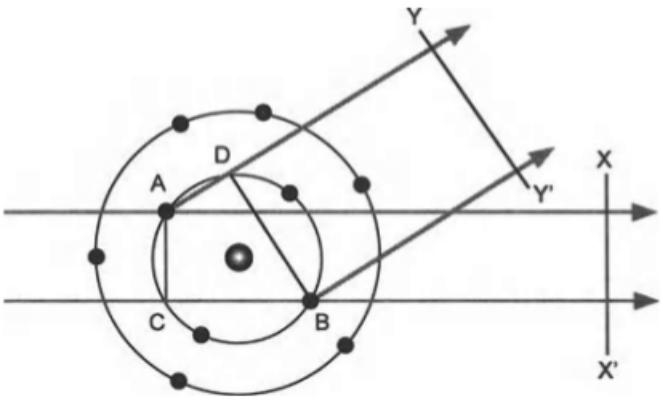

Fig. 3.1 Scattering of X-rays by an atom [16].

The scattering power of an atom can be measured by using the atomic scattering factor, defined as the ratio between the amplitude of a beam scattered by an atom and the amplitude of a beam scattered by an electron located at the center of the atom:

$$f_a = \int_V \rho(\vec{r})\ exp(i\vec{k}\cdot\vec{r})dV \tag{3.2}$$

where $\rho(\vec{r})$ is the atom's electronic density, so that $\rho(\vec{r})dV$ indicates the probability of finding an electron in the volume element dV, which has $\vec{r}$ as its positional vector. Finally, $\vec{k}$ is the diffraction vector defined by

$$\vec{k} = \vec{k}_f - \vec{k}_i \tag{3.3}$$

$$= \frac{2\pi}{\lambda}(\hat{s}_f - \hat{s}_i) \tag{3.4}$$

where λ is the radiation wavelength, $\vec{k}_f$ and $\vec{k}_i$ are the wave vectors of the scattered and incident radiation, respectively, and $\hat{s}_f$ and $\hat{s}_i$ are the unit vectors that define the directions of the scattered and incident beams.

3.1.3 Unit Cell Scattering

The scattering by a unit cell depends on how the atoms are distributed inside that cell, whereas the scattering by an atom depends on the electronic distribution. The various atoms of the unit cell scatter the incident radiation with phase differences that depend on their positions in the unit cell and the scattering power given by their atomic scattering factor.

The scattering power of the unit cell is expressed by the structure factor. The structure factor, $F(\vec{k})$, with k direction, is given by the ratio between the scattering power of the unit cell and the scattering power of an electron placed at the origin of the cell,

$$F\left(\vec{k}\right) = \sum_j f_j\left(\vec{k}\right) exp\left(\vec{k}\cdot\vec{r}_j\right) \tag{3.5}$$

where the summation is made for all the atoms of the unit cell and f_j is the atomic scattering factor of an atom j. The structure factor can also be written as

$$F(hkl) = A(hkl) + iB(hkl) \tag{3.6}$$

where

$$A(hkl) = \sum_j f_j(hkl)\cos 2\pi(hx_j + ky_j + zl_j) \tag{3.7}$$

$$B(hkl) = \sum_j f_j(hkl)\sin 2\pi(hx_j + ky_j + zl_j) \tag{3.8}$$

A phase Φ_{hkl} can be defined for each structure factor:

$$\tan\Phi_{hkl} = \frac{B(hkl)}{A(hkl)} \tag{3.9}$$

and the structure factor can be rewritten as

$$F(hkl) = |F(hkl)|exp\ i\Phi_{hkl}. \tag{3.10}$$

The electronic density function is the Fourier transform of the structure factor and is given by

$$\rho(hkl) = \frac{1}{V}\sum_{h=-\infty}^{\infty}\sum_{k=-\infty}^{\infty}\sum_{l=-\infty}^{\infty} F(hkl)exp[-2\pi(hx+ky+lz)] \tag{3.11}$$

where x, y and z are the coordinates of a given point of the unit cell with volume V. The maximum values of the electronic density function correspond to the atomic positions. So, if the structure factors are known, it is possible to determine the crystal structure.

3.2 Direct Methods

In this method, the relationships between the intensities of the various reflections from the X-ray diffraction experiment are used, leading directly to a solution to the phase problem. The unitary structure factor if given by:

$$U(hkl) = \frac{F(hkl)}{\sum_{j=1}^{N} f_j} \tag{3.12}$$

where N is the number of atoms in the unitary cell and f_j is the diffraction atomic factor of an atom j. The normalized structure factor $E(hkl)$ can be written as

$$|E(hkl)|^2 = \frac{|U(hkl)|^2}{\langle |U(hkl)|^2 \rangle} = \frac{|F(hkl)|^2}{\langle |F(hkl)|^2 \rangle} \tag{3.13}$$

which is normalized because $\langle |E|^2 \rangle = 1$.

As $\langle |U|^2 \rangle = \sum_{j=1}^{N} n_j^2$ and $\langle |F|^2 \rangle = \sum_{j=1}^{N} f_j^2$, the normalized structure factor can be rewritten as

$$|E(hkl)|^2 = \frac{|U(hkl)|^2}{\sum_{j=1}^{N} n_j^2} = \frac{|F(hkl)|^2}{\sum_{j=1}^{N} f_j^2} \tag{3.14}$$

and this equation involves a decomposition in the reciprocal lattice into layers, in such a way that the f_j are adapted to the $F(hkl)$ to reduce it.

In general, a wave's amplitude and phase are independent quantities that, in a X-ray diffraction, can be related through two properties of the probability density function:

- Positivity of the probability density function, that is, $\rho(\vec{r}) \geq 0$;
- Atomicity, that is, the probability density function is composed of discrete atoms.

In 1953, by considering the atomicity condition, Sayre concluded that for a structure formed by well-defined and almost equal atoms, the functions $\rho(\vec{r})$ and $\rho^2(\vec{r})$ are quite similar with the maximum values in the same position. The equation can be written as:

$$F_{\vec{h}} = \frac{\theta_{\vec{h}}}{V} \sum_{\vec{k}} F_{\vec{k}} F_{\vec{h}-\vec{k}} \tag{3.15}$$

where $\theta_{\vec{h}}$ is the ratio between the Fourier transform of $\rho(\vec{r})$ and $\rho^2(\vec{r})$. This equation is valid for both centrosymmetric and non centrosymmetric structures. Multiplying both members of the previous equation by $F_{-\vec{h}}$ gives

$$|F_{\vec{h}}|^2 = \frac{\theta_{\vec{h}}}{V} \sum_{\vec{k}} |F_{\vec{h}} F_{\vec{k}} F_{\vec{h}-\vec{k}}| exp[i|\phi_{\vec{h}} + \phi_{\vec{k}} + \phi_{\vec{h}-\vec{k}}|] \tag{3.16}$$

For high $|F_{\vec{h}}|$ values, the left side of the equation has high, real and positive values. Therefore, if both $F_{\vec{k}}$ and $F_{\vec{h}-\vec{k}}$ have high values:

$$\Phi_{\vec{h}\vec{k}} = \phi_{-\vec{h}} + \phi_{\vec{k}} + \phi_{\vec{h}-\vec{k}} \approx 0 \tag{3.17}$$

For a centrosymmetric structure:

$$S(-\vec{h}) \cdot S(\vec{k}) \cdot S(\vec{h}-\vec{k}) \approx + \tag{3.18}$$

where $S(\vec{h})$ represents the reflection signal and the symbol $\approx$ indicates probabilistic equality. The relationships between phases and magnitudes using probability techniques is an important approach for the practical use of direct methods. For non-centrosymmetic structures, the Sayre relation can be written by specifying the phases or the ratio between the real and imaginary parts, which leads to the formula of the tangent

$$\tan\phi(\vec{h}) \approx \frac{\sum_{\vec{h}} |F(\vec{k})| \cdot |F(\vec{h}-\vec{k})| \cdot \sin(\phi(\vec{k}) + \phi(\vec{h}-\vec{k}))}{\sum_{\vec{h}} |F(\vec{k})| \cdot |F(\vec{h}-\vec{k})| \cdot \cos(\phi(\vec{k}) + \phi(\vec{h}-\vec{k}))} \tag{3.19}$$

For structural factors with high modules:

$$\tan\phi(\vec{h}) \approx \tan[\phi(\vec{k}) + \phi(\vec{h}-\vec{k})] \tag{3.20}$$

3.2.1 Structure Invariants and Semi-Invariants

The observed amplitudes are independent of the chosen reference system while the phases depend on it. From the observed amplitudes, it is only possible to obtain information about the single phases or linear combinations of phases. They are known as **structure invariants** because their value depends only on the structure. The general structure invariant can be calculated from:

$$F_{h_1} F_{h_2} ... F_{h_m} = |F_{h_1} F_{h_2} ... F_{h_m}| exp[i(\phi_{h_1} + \phi_{h_2} + ... + \phi_{h_m})] \tag{3.21}$$

and

$$h_1 + h_2 + ... + h_m = 0 \tag{3.22}$$

This value does not change when the origin is moved by a general vector r_o. The structure factor of index h will be

$$F'_h = \sum_{j=1}^{N} f_j exp\{2\pi i h \cdot (r_j - r_o)\} \tag{3.23}$$

$$= F_h exp\{-2\pi i h \cdot r_o\} \tag{3.24}$$

$$= |F_h| exp[i(\phi_h - 2\pi h \cdot r_o)] \tag{3.25}$$

The modulus remains unchanged while the phase changes by $\Delta_\phi = 2\pi h \cdot r_o$. The variation of the phase of the product will be

$$\Delta_\phi = 2\pi r_o \sum_{i=1}^{m} h_i = 0 \tag{3.26}$$

because of the condition 3.22.

The simplest structure invariants are:

- $F_{000} = \sum_{j=1}^{N} Z_j$ giving the number of electrons in the unit cell; its phase is always zero.
- $F_h F_{-h} = |F_h|^2$, which does not contain any phase information.
- $F_{-h} F_k F_{h-k}$ with phase $\phi_{-h} + \phi_k + \phi_{h-k}$, known as triplet invariant.
- $F_{-h} F_k F_l F_{h-k-l}$ with phase $\phi_{-h} + \phi_k + \phi_l + \phi_{h-k-l}$, called quartet invariant.

The single phases or linear combinations of phases which are invariant with respect to a shift of origin are called **structure semi-invariants**. The structure semi-invariant has the capability of being transformed into a structure invariant by adding one or more pairs of symmetry-equivalent phases.

3.2.2 Structure Determination by Direct Methods

This subsection presents, in a general way, the structure determination process in direct methods.

1. The first step is to calculate the $|E|$'s from the values of |F|. A statistical study of the $|E|$'s is also performed to discover symmetry elements of the crystalline structure.
2. The relations between phases are established for reflections with high $|E|$ values. These relations are structural invariants and semi-invariants.

3. A start group is selected for the phases. This group contains phases that define the origin. Even if these phases are chosen among those involving a large number of triplets, they will not be sufficient to start the phase determination process. Two methods are used to determine the number of extra phases required to start the process:

   (a) In the symbolic addition method, symbols are attributed to unknown phases and the others are determined as combinations of these symbols. This method is best suited for centrosymmetric structures.

   (b) In the multisolution method, several random numerical values are attributed to the unknown initial phases. Initial errors of $40-50°$ do not affect the structure determination process. If the unknown phases have values between 0 and 2π, it is possible to discover them by testing several values in the four quadrants. One of these values will have an error less than 45°. This method is easier to automate and it is more widely used.

4. When the phases are assigned to the starter set, all others are determined in a chain process. The best starting process will be the one that will avoid as long as possible the determination of phases through low probability relationships. A great starting set can be defined by a process known as "convergence". In this process, for each step the reflections that are less related to the others are eliminated. The process has to converge in a set of reflections that must be more correlated and are therefore the most efficient to begin the phase determination process.

5. The phases are expanded with the tangent formula (3.19). This procedure is repeated for each of the permutations of the phases of the starter set. When a sufficiently high number of phases is already determined, they are refined. This refinement is also done using the tangent formula.

6. At this stage of the process, the program has several calculated solutions. To determine which is the most plausible, several metrics are determined. These metrics are usually then combined into a single one.

7. The solution with the best combined metric is used to calculate an electronic density map (E-map). In the electronic density map calculations, it is more convenient to use E's instead of F's as Fourier series coefficients. The high $|E|$'s reflections for which the phases were determined correspond to reflections with high $|F|$'s for small angles and reflections with small $|F|$'s for high angles. Using F's, the contribution of the smaller $|F|$'s would be obscured by the contribution of the larger ones. There is no such problem if E's are used. This way, the resolution of the density maps is improved.

8. After calculating the E-maps, the programs perform an automatic search of the density peaks, providing a list of these peaks ordered by height. This list can be analyzed in terms of distances and angles between peaks. The peaks related to a known geometry can be selected and identified as a possible molecular fragment.

3.3 Patterson Methods

The Patterson function [17] is defined as the self-convolution of the electron density $\rho(r)$.

$$P(u) = \rho(r) * \rho(-r) = \int_v \rho(r)\rho(r+u)dr \tag{3.27}$$

The Fourier transform of P(u) is $|F(r^*)|^2$ and vice versa.

$$P(u) = T^{-1}[|F(r^*)|^2] = \int_{v^*} |F(r^*)|^2 exp(-2\pi i r^* \cdot u)dr^* \tag{3.28}$$

$$= \frac{1}{V}\sum_h |F_h|^2 exp(-2\pi i h \cdot u). \tag{3.29}$$

Since $|F_h| = |F_{-h}|$, the Patterson function can be written as

$$P(u) = \frac{1}{V}\sum_h |F_h|^2 \cos(2\pi h \cdot u) \tag{3.30}$$

and then P(u) = P(-u), which means the Patterson function is always centrosymmetric even when $\rho(r)$ is not.

Since $|F_h|^2$ depends on the interatomic vectors, it is expected that P(u) will also give information about these quantities. Considering an idealized structure formed by n point-like atoms with an associated weight equal to their atomic number, the equation 3.27 becomes a summation over the n points

$$P(u) = \sum_{j=1}^{n} \rho(r_j)\rho(r_j+u) \tag{3.31}$$

The Patterson function will have maxima corresponding to all possible interatomic vectors within the unit cell and the height of each peak will be proportional to the product of the atomic numbers of the atoms. In addition, the Patterson function has the same periodicity as the electron density.

The density map will have prominent maxima when the structure contains a limited number of heavy atoms. The information about the coordinates of these heavy atoms represents a good initial model. Furthermore, the phase ϕ_h^c of the calculated structure factor is a good approximation and using the observed amplitudes it is possible to compute an electron density map. This map also shows other less heavier atoms of the structure. Using the atoms that are known, new electron density maps are computed from their phases, revealling new atoms until the structure is complete.

3.4 Completing and refining the structure

3.4.1 Difference Fourier Method

A convenient way of completing and refining a structural model is the **difference Fourier Synthesis Method**. A Fourier series having as coefficients the $|F_h^c|$s computed using equation

$$\rho_c(r) = \frac{1}{V}\sum_h F_h^c exp(-2\pi ih\cdot r) \tag{3.32}$$

will show maxima at the positions of the atoms of the given model, while a series with coefficients $F_h^o = |F_h^0|exp(i\phi_{true})$

$$\rho_o(r) = \frac{1}{V}\sum_h F_h^o exp(-2\pi ih\cdot r) \tag{3.33}$$

represents the true structure. The difference series can be calculated to see how much the initial model deviates from the real structure:

$$\Delta\rho(r) = \rho_o(r) - \rho_c(r) = \frac{1}{V}\sum_h (F_h^o - F_h^c)exp(-2\pi ih\cdot r) \tag{3.34}$$

The approximation $\phi_{true} \approx \phi_h^c$ is used because the values of ϕ_{true} are not known. The previous equation then becomes

$$\Delta\rho(r) = \frac{1}{V}\sum_h (|F_h^o| - |F_h^c|)exp(-2\pi ih\cdot r + i\phi_h^c) \tag{3.35}$$

This method can be very useful for different types of errors:

- **Missing Atoms:** When an atom is missing, $\rho_c(r)$ is zero at its corresponding position, while $\rho_o(r)$ shows a maximum. The difference Fourier synthesis also shows a peak at the same position but it is close to zero at the positions of the model atoms where $\rho_o(r) \approx \rho_c(r)$. This method allows the correct localization of light atoms even when

the model contains much heavier atoms. An example of this is the localization of hydrogen atoms, since they only have one electron, they do not contribute much to the X-ray diffraction, even in the presence of medium sized atoms.

- **Position Errors:** If ρ_o gives the correct position of the atom and ρ_c gives the wrong position in the model, in the $\Delta\rho$ map, ρ_c is close to a negative minimum, while the correct position is towards the neighboring positive maximum.
- **Errors in thermal parameters:** When the thermal motion has been neglected or underestimated in the model, the ρ_o density has a smaller and wider peak with respect to ρ_c. As a result, in the difference Fourier synthesis a negative depression appears, surrounded by a positive ring. When a high thermal motion has been assumed for one atom of the model, Δ_ρ shows a small positive maximum surrounded by a negative ring.

3.4.2 Least-squares Method

This method starts with a set of parameters of the initial model, X^0, and calculates variations of these parameters, with the new parameters, $\mathbf{X} = X^0 + \Delta\hat{\mathbf{X}}$, serving as an initial model, with which new variations are determined. This process is repeated until the variations $\Delta\hat{\mathbf{X}}$ are very small. In this interactive process, variations of the initial model that minimize the quantity

$$\sum_{\vec{h}} \omega_i \left(|F_o(\vec{h})|^2 - S|F_c(\vec{h})|^2 \right)^2 \tag{3.36}$$

are calculated, where ω_i are the weights to be assigned to each term of the sum and S is an adjustable scale factor in the refinement. In SHELXL program,

$$\omega_i = \frac{1}{\sigma^2(F_o^2) + (aP)^2 + bP} \tag{3.37}$$

where $\sigma^2(F_o^2)$ is the standard deviation of F_o^2, a and b are adjustable parameters and $P = \frac{(F_o^2 + 2F_c^2)}{3}$. In addition to the scaling factor, the other commonly refined parameters are the thermal vibration parameters.

3.5 SHELXL-97

This section mentions the crystal structure refinement program SHELXL [18], which is by far the most popular refinement program for small molecules. SHELXL-97 is part of the

SHELXS-97 program suite, which uses Patterson and classical direct methods for molecular structure solution. This program requires an input file with the diffraction data (h, k, l, F^2 e $\sigma(F^2)$) and another with instructions and information about the unit cell like cell parameters and cell symmetry. The file containing the structure solution can be used as an input file of SHELXS-97 program. The SHELXL-97 program is used to complete and refine structures. By using least square methods, this program does Fourier synthesis and structural refinements.

Chapter 4

Molecular Magnetism

4.1 Orbital and Spin Angular Momentum

The orbital angular momentum is the orbital motion of an electron around the nucleus. In an atom, it will depend on the quantum state occupied by the electron. The component of orbital angular momentum with a magnitude of $\sqrt{l(l+1)\hbar}$ along the z axis is $m_l\hbar$. The z component of the magnetic moment is $-m_l\mu_B$ and the magnitude of the total magnetic dipole moment is $\sqrt{l(l+1)}\mu_B$, where μ_B is the Bohr magneton, defined as $\mu_B = \frac{e\hbar}{2m_e}$.

Electrons have an intrinsic magnetic moment which depends on their intrinsic angular momentum, known as spin. The spin quantum number, s, for an electron is $\frac{1}{2}$.

The z component of spin angular momentum is $m_s\hbar$ and for an electron with s = $\frac{1}{2}$, two values are possible: $m_s = \pm\frac{1}{2}$. Therefore, the component of angular moment can be $\frac{\hbar}{2}$ or - $\frac{\hbar}{2}$ ('up' and 'down').

The total angular momentum J of an atom containing N electrons is given by

$$J = L + S \tag{4.1}$$

where the orbital angular momentum, $L = \sum_{i=1}^{N} L_i$, is the vector sum of the orbital angular momenta L_i of the N electrons and

$$S = \sum_{i=1}^{N} S_i \tag{4.2}$$

is the total spin angular momentum, which is vector sum of the spin angular momenta S_i of the N electrons.

In a magnetic field, the energy of the electron is

$$E = g\mu_B m_s B \tag{4.3}$$

In 1896, Zeeman observed that the spectral lines of atoms can split in the presence of an external magnetic field by an amount of $g\mu_B B$. This phenomenon is known as the Zeeman splitting.

4.2 Magnetic Susceptibility

The magnetization, M, is defined as the magnetic moment per unit volume. For a linear material, $M = \chi H$, where χ is the magnetic susceptibility and represents the magnetic moment induced by a magnetic field H per unit volume. Most often, it can be represented in terms of the molar magnetic susceptibility, χ_m,

$$\chi_m = \chi V_m, \tag{4.4}$$

where V_m is the volume occupied by 1 mole (6.022×10^{23} atoms) of the compound.

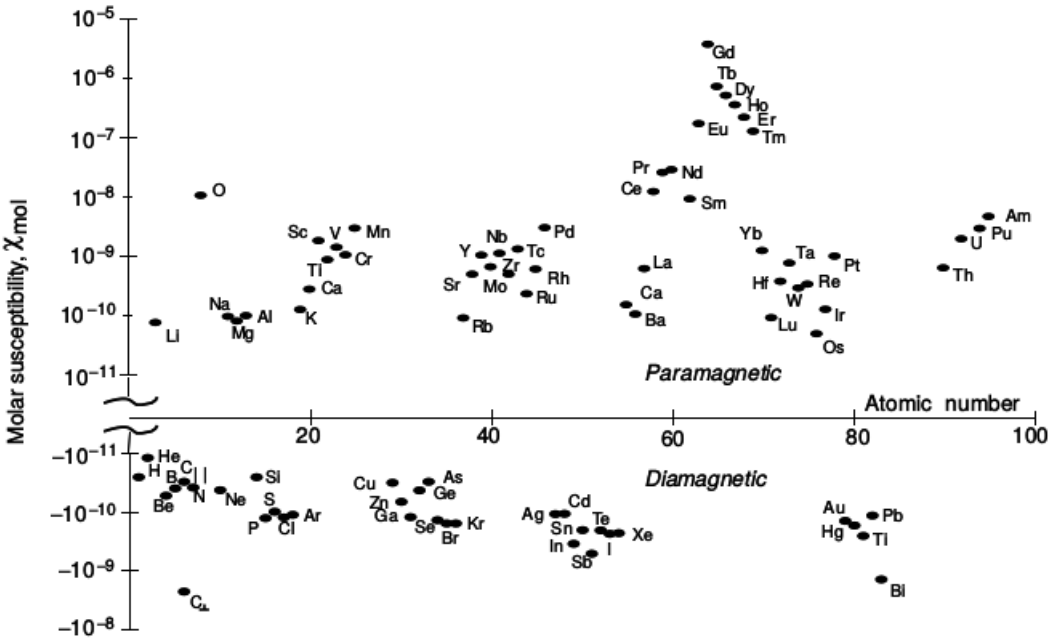

Fig. 4.1 Molar Susceptibility of the elements of the periodic table [19].

4.3 Diamagnetism

Diamagnetism corresponds to a repulsive effect in materials in the presence of a magnetic field. The magnetic substance shows a weak and negative magnetic susceptibility. All materials show some degree of diamagnetism, but it is a weak effect and can either be ignored or is a small correction to the applied field. This type of magnetization is the most common and it can be described using a quantum mechanical approach.

Table 4.1 Magnetic Susceptibility values for diamagnetic materials [20].

Material	Magnetic Susceptibility ($\times 10^{-5}$)
Water	-0.91
Copper	-1.0
Lead	-1.8
Silver	-2.6
Mercury	-2.9

4.4 Paramagnetism

Paramagnetic materials have a positive magnetic susceptibility and when they are in a magnetic field, the magnetization aligns parallel to the applied field.

In the paramagnetic effect, atoms with a non-zero magnetic moment are considered. Therefore, when there is no magnetic field, these magnetic moments point in random directions, and become parallel to the magnetic field when it is present.

The total angular momentum $\vec{J}$ is the sum of the orbital angular momentum $\vec{L}$ and the spin angular momentum $\vec{S}$

$$\vec{J} = \vec{L} + \vec{S} \tag{4.5}$$

and it is associated with the magnetic moment of an atom.

Paramagnetism is normally stronger than diamagnetism although diamagnetism is always present in materials with a negative contribution.

Table 4.2 Magnetic susceptibility values for paramagnetic materials [20].

Material	Magnetic Susceptibility ($\times 10^{-5}$)
Iron oxide	720
Iron amonium alum	66
Uranium	40
Platinum	26
Tungsten	6.8
Sodium	0.72

4.4.1 The Brillouin Function and the Curie Law

The general case, where J can take any integer or half-integer value, is considered. The partition function is the sum of the Boltzmann factors weighted by any degeneracy and is given by

$$Z = \sum_{m_J=-J}^{J} \exp(m_J g_J \mu_B B / k_B T). \tag{4.6}$$

If $x = g_J \mu_B B / k_B T$,

$$\langle m_J \rangle = \frac{\sum_{m_J=-J}^{J} m_J e^{m_J x}}{\sum_{m_J=-J}^{J} e^{m_J x}} = \frac{1}{Z}\frac{\partial Z}{\partial x} \tag{4.7}$$

$$M = n g_J \mu_B \langle m_J \rangle = \frac{n g_J \mu_B}{Z}\frac{\partial Z}{\partial B}\frac{\partial B}{\partial x} = n k_B T \frac{\partial lnZ}{\partial B}. \tag{4.8}$$

The partition function Z is a geometric progression with multiplying term $r = e^x$ and initial term $a = e^{-Jx}$, so that

$$a + ar + ar^2 + ... + ar^{M-1} = \sum_{j=1}^{M} ar^{j-1} = \frac{a(1-r^M)}{1-r}, \tag{4.9}$$

where $M = 2J+1$ is the number of terms in the series. After some manipulations,

$$Z = \frac{\sinh[(2J+1)\frac{x}{2}]}{\sinh[\frac{x}{2}]}. \tag{4.10}$$

The maximum magnetization that can be obtained when all the magnetic moments are aligned is called the saturation magnetization M_s. With the substitution

$$y = xJ = g_J \mu_B JB/k_B T, \tag{4.11}$$

it is found that

$$M = M_s B_J(y) \tag{4.12}$$

$$M_s = n g_J \mu_B J \tag{4.13}$$

where n is the number of magnetic moments per unit volume and $B_J(y)$ is the Brillouin function given by

$$B_J(y) = \frac{2J+1}{2J} \coth\left(\frac{2J+1}{2J} y\right) - \frac{1}{2J} \coth\frac{y}{2J}. \tag{4.14}$$

For small y, y « 1,

$$B_J(y) = \frac{(J+1)y}{3J} + O(y^3). \tag{4.15}$$

Hence, for small magnetic fields ($\chi << 1$, so $B \approx \mu_0$H) the susceptibility is given by

$$\chi = \frac{M}{H} \approx \frac{\mu_0 M}{B} = \frac{n\mu_0 \mu_{eff}^2}{3k_B T} \tag{4.16}$$

This equation, called Curie's law, shows that the magnetic susceptibility is inversely proportional to the temperature. The value of the effective moment is given by

$$\mu_{eff} = g_J \mu_B \sqrt{J(J+1)} \tag{4.17}$$

Curie's law is often written as $\chi = \frac{C}{T}$, where C is the Curie constant.

4.5 Ferromagnetism

The materials that have ferromagnetic properties (ferromagnets), their magnetic moments aligned parallel to the magnetic field, if applied. Even when no magnetic field is present, a ferromagnet has a spontaneous magnetization.

4.5.1 The Weiss Model of a Ferromagnet and the Curie Weiss Law

The effect of ferromagnetism is mostly due to exchange interactions and is equivalent to an effective molecular field B_{mf} produced by the neighboring spins. The molecular field is given by

$$B_{mf} = \lambda M, \tag{4.18}$$

where λ is a constant which characterizes the strength of the molecular field. For a ferromagnet, $\lambda > 0$.

At low temperatures, the magnetic moments are aligned to the internal molecular field, even when no applied magnetic field is present. As the temperature increases, thermal fluctuations begin to destroy the magnetization and at a critical temperature it is destroyed. This model is known as the Weiss Model of Ferromagnetism. The transition temperature, the Curie temperature T_C, is written as

$$T_C = \frac{g_J \mu_B (J+1) \lambda M_s}{3k_B} = \frac{n\lambda \mu_{eff}^2}{3k_B} \tag{4.19}$$

The molecular field is thus

$$B_{mf} = \lambda M_s = \frac{3k_B T_C}{g_J \mu_B (J+1)} \tag{4.20}$$

For a ferromagnet with $J = \frac{1}{2}$ and $T_C \approx 10^3 K$, $B_{mf} = \frac{k_B T_C}{\mu_B} \approx 1500\ T$. The molecular field is extremely large in ferromagnets due the Coulomb energy involved in the exchange interaction.

Applying a small B field at $T \geqslant T_C$, the approximation for the Brillouin function (y « 1)

$$\frac{M}{M_s} \approx \frac{g_J \mu_B (J+1)}{3k_B} \left(\frac{B + \lambda M}{T} \right). \tag{4.21}$$

can be used.

The magnetic susceptibility can be written as

$$\chi = \frac{C}{T - T_C} \tag{4.22}$$

which is known as the Curie Weiss law.

4.6 Antiferromagnetism

In Antiferromagnetic materials, the magnetic moments lie anti-parallel to one another. The crystalline structure of the material can be represented as a sum of two sub-lattices, one with spin up and the other with spin down, in which the magnetization is zero.

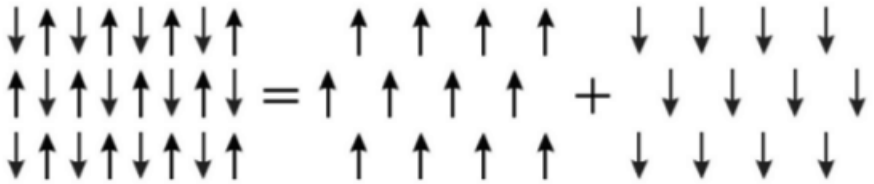

Fig. 4.2 A schematic representation of the antiferromagnetic effect [21].

In most cases, antiferromagnetism disappears for temperatures above a transition temperature, known as the Néel temperature T_N, defined as

$$T_N = \frac{g_J \mu_B (J+1)|\lambda| M_s}{3k_B} = \frac{n|\lambda|\mu_{eff}^2}{3k_B}, \tag{4.23}$$

where λ is the molecular field constant and has a negative value. In this case, for small fields, the Brillouin function can also be used and the magnetic susceptibility can be fitted to a Curie Weiss dependence given by

$$\chi = \frac{1}{T-\theta}, \tag{4.24}$$

where θ is the Weiss temperature, which can give important information about the material. If

- $\theta < 0$ the material is a antiferromagnet.
- $\theta = 0$ the material is a paramagnet.
- $\theta > 0$ the material is a ferromagnet.

Table 4.3 Properties of some antiferromagnetic materials [15].

Material	T_N (K)	θ (K)	J
MnF_2	67	-80	$\frac{5}{2}$
MnO	122	-610	$\frac{5}{2}$
CoO	292	-330	$\frac{3}{2}$
FeO	198	-507	2
Cr_2O_3	307	-485	$\frac{3}{2}$
$\alpha - Fe_2O_3$	950	-2000	$\frac{5}{2}$

4.7 Isotropic Interactions in Dinuclear Compounds

Considering two copper(II) ions (A and B), each one with local spins $S_A = S_B = 1/2$. If the two ions don't interact with one another, then the quantum numbers S_A and S_B are used and the Curie-Weiss law is applied. But, if the two ions interact with one another, the quantum numbers S=0 or S=1 are used to describe the system.

Let E(S=0) and E(S=1) be the energy difference between an S=0 state and an S=1 state. J, the energy gap separating E(S=0) and E(S=1) can be written as

$$J = E(S=0) - E(S=1) \tag{4.25}$$

When the ground state is S=0, the interaction is **antiferromagnetic** and J (the isotropic interaction parameter) is negative. On the other hand, when the ground state is S=1, the interaction is **ferromagnetic** and J is positive.

The Hamiltonian accounting for this effect can be defined as

$$\hat{H} = -J\hat{S_A} \cdot \hat{S_B} \tag{4.26}$$

The energy of the S_{Total} state, due to the interaction of species with S_A and S_B states, can be written as

$$E_{Total} = -\frac{1}{2}J_{AB}[S_{Total}(S_{Total}+1) - S_A(S_A+1) - S_B(S_{B+1})] \tag{4.27}$$

When a magnetic field H is present, the microstates of the S=1 state (M_S=-1,0,1) will no longer have the same energy (E(S=1; M_S=0)) and Zeeman effect is considered:

$$E_n = E_n^{(1)} = M_S g\beta \tag{4.28}$$

and the Hamiltonian that describes this effect is

$$\hat{H} = g\beta\hat{S}\cdot H \tag{4.29}$$

So, the total spin taking into account magnetic coupling and Zeeman perturbation is

$$\hat{H} = -J(\hat{S}_A\cdot\hat{S}_B) + \beta(\hat{S}_A g_A + \hat{S}_B g_B)\cdot H \tag{4.30}$$

The local g-tensors, g_A and g_B, are equal and it is assumed that they are isotropic with the g principal value.

Using the zero order energy from magnetic coupling and the first order energy from Zeeman splitting:

$$E_n = E_n^{(0)} + E_n^{(1)}H \tag{4.31}$$

where

$$E_n^{(0)} = E(S) \tag{4.32}$$

$$= -\frac{J}{2}[S(S+1) - S_A(S_A+1) - S_B(S_B+1)] \tag{4.33}$$

and $E_n^{(1)} = M_S g\beta$. So, the Van Vleck equation can be written as

$$\chi = \frac{N}{K_B T}\frac{\sum_n {E_n^{(1)}}^2 \exp(-E_n^0/K_B T)}{\sum_n \exp(-E_n^{(0)}/K_B T)} \tag{4.34}$$

$$= \frac{N}{K_B T}\frac{\sum_S \sum_{M_S=-S}^{M_S=+S}(M_S g\beta)^2 \exp(-E(S)/K_B T)}{\sum_S (2S+1)\exp(-E(S)/K_B T)} \tag{4.35}$$

$$= \frac{Ng^2\beta^2}{K_B T}\frac{\sum_S \sum_{M_S=-S}^{M_S=+S}(M_S)^2 \exp(-E(S)/K_B T)}{\sum_S (2S+1)\exp(-E(S)/K_B T)} \tag{4.36}$$

$$= \frac{Ng^2\beta^2}{3K_B T}\frac{\sum_S S(S+1)(2S+1)\exp(-E(S)/K_B T)}{\sum_S (2S+1)\exp(-E(S)/K_B T)} \tag{4.37}$$

For the Cu(II)−Cu(II) system, the Van Vleck equation can be simplified to the Bleaney-Bowers equation:

$$\chi = \frac{2Ng^2\beta^2}{K_BT[3+\exp(-J/K_BT)]} \tag{4.38}$$

For the Fe(III)−Fe(III) system the local spins are $S_A = S_B = 5/2$. Using all the possible values of S (0, 1, 2, 3, 4, 5) and their resulting energy values E(S), the Van Vleck equation can be rewritten as

$$\chi = \frac{2Ng^2\beta^2}{K_BT}\frac{e^x + 5e^{3x} + 14e^{6x} + 30e^{10x} + 55e^{15x}}{1 + 3e^x + 5e^{3x} + 7e^{6x} + 9e^{10x} + 11e^{15x}} \tag{4.39}$$

with $x = \frac{|J|}{K_BT}$.

4.8 Chains of Copper(II) Ions: Bonner and Fisher's Model

Bonner and Fisher in 1964 calculated the magnetic susceptibility of ring chains up to n=11 for Cu(II) and extrapolated for the infinite ring [22]. The spin Hamiltonian in zero-field adapted to describe the isotropic interaction between copper (II) ions, each one with S=1/2, is:

$$H = -J\sum_{i=1}^{n-1} S_{A_i}S_{A_{i+1}} \tag{4.40}$$

Bonner and Fisher's results have been fitted by the following numerical expression:

$$\chi = \frac{Ng^2\mu_B^2}{K_BT}\frac{0.25 + 0.074975x + 0.075235x^2}{1.0 + 0.9931x + 0.172135x^2 + 0.757825x^3} \tag{4.41}$$

with $x = \frac{|J|}{K_BT}$

Chapter 5

Experimental Techniques

5.1 Single Crystal

5.1.1 Introduction

The X-Rays, discovered in 1895 by W. C. Roentgen, are electromagnetic waves whose wavelength is in the order of Å(10^{-8}cm). This order of magnitude coincides with the spacing of the atoms in a crystalline lattice, as this is the typical interatomic distance in crystalline solids.

X-Ray diffraction occurs when a non-polarized beam of light, called incident radiation, strikes an electron and vibrates at the same frequency as the light beam, absorbing and emitting energy in all directions as X-rays. This radiation has the same frequency as the incident radiation, which is the same as saying it has the same wavelength [23].

X-Ray diffraction is one of the most used techniques to study and determine the crystalline phases present in materials, allowing the identification of the chemical composition and structure of the present compounds, being essential to a better understanding of the structural organization of crystalline compounds.

5.1.2 Elementary Theory of XRD

The diffraction from a crystalline sample can be explained and visualized by using the simplified version, described by Bragg father and son, of the theory developed by Von Laue, in which an incident X-ray beam would be reflected by sets of parallel planes (h,k,l) of atoms, equally spaced by a distance d [24]. The condition for diffraction from such set of planes is

$$2d\sin(\theta) = n\lambda \tag{5.1}$$

which states that in order to get a constructive interference condition, the path length difference between two incident waves in consecutive planes must be a multiple number of the wavelength, λ. The angle θ is the incident angle of the beam to the planes and n is the order of reflection such that for $n = 1, 2, \ldots$, we get reflections of first, second order, etc., relative to the same set of planes (h,k,l).

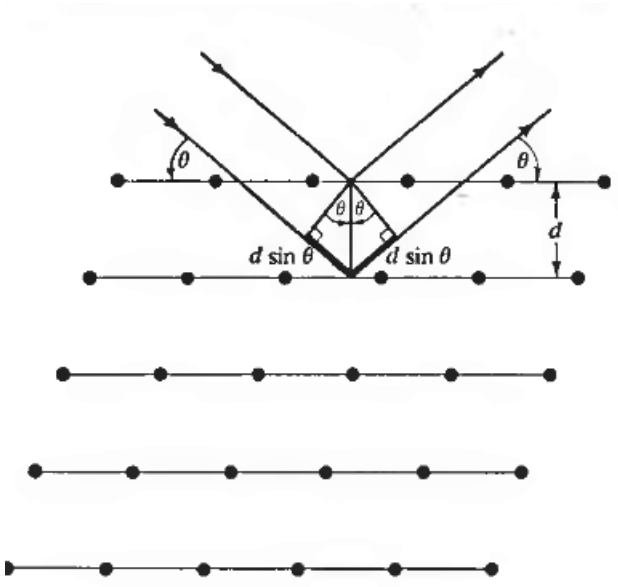

Fig. 5.1 Schematic representation of Bragg's law [24].

As the diffracted beam exits the sample with the same angle θ with respect to the reflecting planes, 2θ is the diffracted angle, that is, the angle between the diffracted and incident beams. The intensity of the diffracted beam, I_{hkl}, is proportional to the square of the magnitude of the structure factor as mentioned above:

$$I_{hkl} \propto |F_{hkl}|^2 \tag{5.2}$$

5.1.3 XRD Equipment

The equipment used in this work was a Bruker AXS APEX II diffractometer [25]. Important components of this material include:

- APEX II CCD Detector;

- 4-axis Kappa goniometer;
- K780 X-ray generator;
- Radiation safety enclosure;
- D8 controller;
- Refrigerated recirculator for the detector;
- Instrument control (BIS) and crystallographic software (Apex 2) computer;
- Video Microscope;
- Timing shutter and incident beam collimator.

A shilded X-ray tube, an X-ray safety shutter and a graphite crystal monochromator are three components of the X-ray source. The sealed-tube X-ray source produces the X-ray beam used by the system and the X-ray safety shutter is built into the X-ray tube shield. The status lamps indicate when the shutter is open (red) or closed (green). The shutter is also connected to the controller and to the safety interlocks. The K_α line ($\lambda_{avg} = 0.710730$ Åfor Mo radiation, λ_{avg} = 1.541838 Åfor Cu radiation) is selected and emitted from the X-ray source and passes it down the collimator system.

The k780 X-ray generator provides a source of power for operations up to 60 kV and 50 milliamps (mA). Typical maximum power settings for the APEX II system are:

- 50 kV, 40 mA for Mo radiation
- 40 kV, 30 mA for Cu radiation

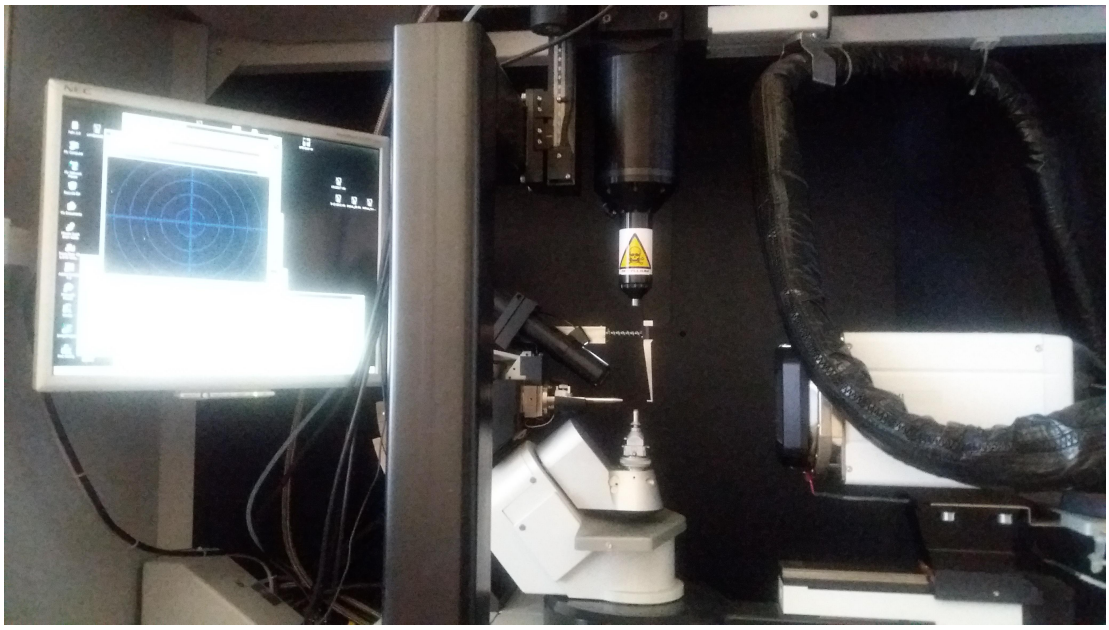

Fig. 5.2 Bruker AXS APEX II diffractometer.

The monochromatic X-ray beam passes through a small labyrinth, the timming shutter, a secondary labyrinth and the incident beam collimator before iluminating the crystal. The labyrinth is a device that ensures that the collimator and shutter are tightly connected to prevent X-ray leakage. The timming shutter is a device, which controls the exposure time for each frame during data collection. The incident beam collimator has pinholes near the crystal and the source. These pinholes help to define the shape and size of the incident X-ray beam that strikes the crystal. The beamstop catches the remainder of the X-ray beam after it has passed the crystal and minimize scattered X-rays and to prevent the direct X-ray beam from hitting the detector. The collimator is supported by a collimator support assembly that is aligned so that the X-ray beam passes through the center of the goniometer.

The Kappa APEX II system uses a horizontally-oriented kappa goniometer with 2θ, ω, κ and ϕ drives and a motorized DX track for setting the detector distance. The Kappa APEX II also includes mounting points for attachments such as the optional low-temperature attachment and for the video microscope. The crystal can be oriented at χ from $-92°$ to $92°$ and this can leave the instrument open for easy access. The ϕ drive has unlimited rotation and κ can be positioned so that the ϕ drive can be swung under the incident beam collimator. As a result, ω can have free rotation.

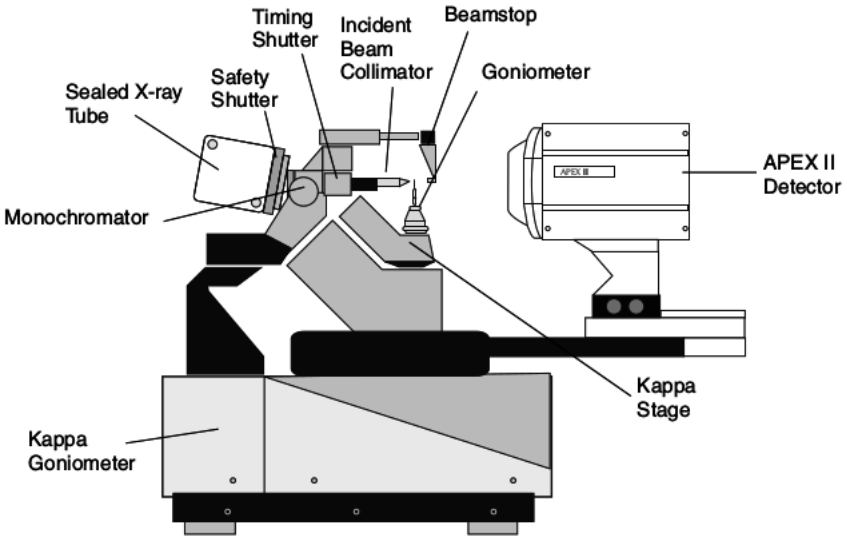

Fig. 5.3 Kappa-4axis goniometer components [25].

The video microscope allows to visualize the crystal to align it in the direct beam and measure the crystal's dimensions. Peltier devices are used to cool the CCD detector to approximately $-50°$, so they can minimize dark current. The refrigerator recirculator uses a mixture containing ethylene glycol/water to absorb the heat. The D8 controller is an electronic module that contains all of the electronics and firmware for controlling the generator and monitoring other instruments.

5.1.4 Intensity Correction of the Diffracted Beams

During the diffraction experiment, the intensity values must be corrected according to the experimental conditions, in order to obtain correct structure factors [26, 27]. Examples of this corrections include:

- **Lorentz Factor:** The intensity of a reflection is proportional to the time that a point of the reciprocal lattice with finite dimensions takes to travel through the sphere of reflection. The Lorentz factor is a geometric factor that takes into account the different velocities in which the points of the reciprocal lattice pass through the reflection sphere. If w is the crystal angular velocity and v_n is the velocity component of a point of the reciprocal lattice according to the radius of the sphere, the Lorentz factor is defined as

$$L = \frac{w}{v_n} = \frac{1}{\sin 2\theta} \tag{5.3}$$

For small Bragg angles, L is large since the point of the reciprocal lattice is close to the origin. For high θ, L is high because the point of the reciprocal lattice passes tangentially across the surface of the reflection sphere. The maximum decrease of the diffracted intensity due to the Lorentz factor occurs when $\theta = 45°$.

- **Polarization Correction:** In X-ray diffraction, the polarization factor comes from the dependence of the amplitude diffracted with the orientation of the electric field vector of the X-ray beam. The value of the polarization factor depends on the degree of polarization of the diffracted X-ray beam. The characteristic radiation of the ampoule is non-polarized. When the incident radiation is monochromatic and the geometry is equatorial, the incident beam in the sample is partially polarized due to diffraction by the monochromator crystal. The polarization factor is defined by:

$$p = \frac{1 + \cos^2 2\theta_M \cos^2 2\theta}{\cos^2 2\theta_M} \tag{5.4}$$

where θ_M is the monochromator angle (Bragg angle of the crystal used as monochromator). In order to minimize the correction of the polarization factor of the various monochromator crystals available, the one with a Bragg angle closer to 0° or 90°, such that p is minimum, should be chosen.

- **Multiplicity Factor:** In some X-ray diffraction methods, such as X-ray diffraction by polycrystalline samples, it is impossible to measure separately certain reflections $h_1k_1l_1$, $h_2k_2l_2$; the energy of the diffracted beam is the sum of the energies of each of the reflections:

$$E_{\text{total}} = E_{h_1k_1l_1} + E_{h_2k_2l_2} + ... = \sum E_i \tag{5.5}$$

If all the reflections are equivalent by symmetry, their energy is equal, the total energy begin equal to

$$E_{\text{total}} = mE_{hkl} \tag{5.6}$$

where m is the multiplicity factor (integer number). The same is valid for the intensity, so the measured intensity must be divided by the multiplicity factor.

- **Absorption Factor:** The intensity of an X-ray beam passing through a material is attenuated by absorption, which corresponds to the partial transfer of the energy of the electromagnetic radiation to the atoms of the material. When an X-ray beam of

intensity I penetrates a crystal of thickness dx, its intensity is reduced by a value dI. The intensity variation, dI, is proportional to the original intensity, the thickness dx and the absorption coefficient μ:

$$-dI = \mu I dx \Longleftrightarrow -\frac{dI}{I} = \mu dx \tag{5.7}$$

Integrating the previous expression, knowing that I_0 is the intensity of the incident beam passing through a crystal of thickness x,

$$I = I_0 e^{-\mu x} \tag{5.8}$$

This equation shows that the intensity of the radiation passing through a thickness x of the sample is reduced by a factor $e^{-\mu x}$. The quantity μ is called the linear absorption coefficient and its units are the inverse of the distance. For any crystal, μ depends on the chemical composition, the density, the mass absorption coefficients and the radiation used. The linear absorption coefficient, μ, is calculated from the mass absorption coefficients $\left(\frac{\mu}{\rho}\right)$ of the various elements A, B, C of the crystal

$$\mu = D\left[p_A\left(\frac{\mu}{\rho}\right)_A + p_B\left(\frac{\mu}{\rho}\right)_B + p_C\left(\frac{\mu}{\rho}\right)_C + ...\right] \tag{5.9}$$

where D is the crystal density, p_A is the fraction of element A in compound ABC and ρ is the density. When μ is high, the absorption factor significantly reduces the intensities, so it is necessary to consider this correction.

- **Primary Extinction:** The phenomenon of extinction results from the attenuation of the primary beam when penetrating the crystal, reducing the intensity of the diffracted beam. This effect depends on the degree of perfection of the crystal. The phase of the diffracted radiation differs by $\pi/2$ with respect to the primary beam. The beams that are reflected twice differ in phase by π with respect to the direct beam and will therefore interfere destructively, causing their attenuation. As the primary beam penetrates the crystal, it is continuously attenuated.

  The primary extinction effect, when significant, is important for high structure factors F_{hkl} and for high interplanar distances. On the other hand, it is independent of the wavelength λ of the incident radiation. The correction of primary extinction is difficult and even if some correction is made, it still introduces an important imprecision.

Therefore, it is usually avoided by using less perfect crystals or polycrystalline samples with grain size less than 10^{-4} cm.

- **Secondary Extinction:** When an X-ray beam passes through a crystal whose orientation is such that the Bragg condition is not satisfied for any set of planes, its intensity is reduced due to normal absorption. However, if the Bragg condition is satisfied for any set of planes, there is an additional attenuation of the primary beam. The intensity of the primary beam incident on a given plane is less than the intensity of the original beam since part of the primary beam was reflected by the previous planes. The decrease of the primary beam intensity due to this kind of attenuation is called **secondary extinction**.

  The secondary extinction behaves in a similar way to absorption, being possible to add the two,

$$\mu = \mu_0 + aE' - bE'^2 \tag{5.10}$$

  where the first term is the absorption coefficient, the second term is the secondary extinction (a = Constant, E' = energy removed from the reflected beam) and the third term corresponds to the primary extinction (b depends on several parameters, including the perfection degree). The phenomenon of secondary extinction is difficult to eliminate, but can be reduced by increasing the degree of imperfection of the crystal. Reflections with low $\frac{\sin\theta}{\lambda}$ values and high intensities are the most affected by secondary extinction. In polycrystalline samples, there is practically no secondary extinction, since at each moment only a small fraction of crystallites is in conditions of diffraction.

- **Temperature Factors:** Each atom in a crystal is connected to other atoms by binding forces of various types and the equilibrium position of the atoms corresponds to the minimum potential energy. If the atom is removed from its equilibrium position, the elastic force tends to move it back, making the atom oscillate around that position. The vibrations on an atom simulate a larger volume than it would occupy if the atom were at rest by reducing the value of the atomic diffraction factor f_a to a new value f'_a:

$$f'_a = f_a e^{-B\frac{\sin^2\theta}{\lambda^2}} \tag{5.11}$$

  The temperature coefficient is given by $B = 8\pi^2(\bar{u})^2$, where $\bar{u}$ is the average vibration amplitude of the atom perpendicular to the reflection planes. It was assumed that the

vibration motion of the atom was spherical. However, sometimes the anisotropy of the molecular arrangement implies that $\bar{u}$ changes with direction. The temperature factor is then:

$$e^{-B_{11}h^2+B_{22}k^2+B_{33}l^2+B_{12}hk+B_{23}kl+B_{31}lk} \tag{5.12}$$

where the B_{ij} values depend on the directions of vibration.

- **Anomalous Scattering:** The diffraction power of an electron in the solid may be greater or less than that of a free electron. This effect, called anomalous scattering, is particularly important when the frequency of the incident radiation is close to the resonance frequency of the atom. The tabulated values for atomic diffraction factors f_0 are altered to take into account this effect by the addition of a real term $\Delta f'$ and an imaginary term $\Delta f''$. This can be shown by the following equation:

$$f = f_0 + \Delta f' + i\Delta f'' \tag{5.13}$$

Both terms depend on the wavelength of the radiation used, increasing as λ increases. For light elements (up to Mg or Al with CuK_α) the effect is very small, but for heavier elements it is necessary to consider this correction.

5.2 Powder X-Ray Diffraction

A polycrystalline sample contains a large number of small crystallites typically 0.1 to 10 μm in dimension and with a random orientation. When an X-ray beam strikes a polycrystalline sample, the beam is scattered in all directions. In addition, each set of planes of atoms gives rise to a cone of diffraction intensity, each one representing diffraction from a single crystallite within the powder sample.

A powder diffractometer uses an electronic detector to measure the angles of the diffracted beams and the intensity of the X-rays detected is recorded as a function of the detector angle. The number and positions of the reflections depend on the crystal form, cell parameters and lattice type.

The peak intensities depend on the types of atoms present and their positions. All crystalline solids have a unique powder X-ray diffraction pattern and this can be used as a fingerprint library to identify an unknown substance [11].

5.2.1 XRD Equipment

The Diffractometer

The powder diffractometer (ENRAF NONIUS FR 590) is used to obtain spectra of polycrystalline samples in a Debye-Scherrer geometry or horizontal geometry. The principal components are:

- A monochromator, which has a curved quartz crystal ($2\theta_M = 26.64°$).
- Copper X-ray ampoule (CuK_{α_1} radiation, $\lambda = 1.5405981$ Å).
- The goniometer in which the glass capillary containing the sample is placed. During data collection, the goniometer rotates at a constant speed in order to avoid effects due to a possible preferential orientation of microcrystals.
- The curved detector, INEL CPS 120 (Curved Position Sensitive Detector), which covers an angular region of 120°.
- Set of slits placed before and after the monochromator to set the height and width of the incident beam in the sample.

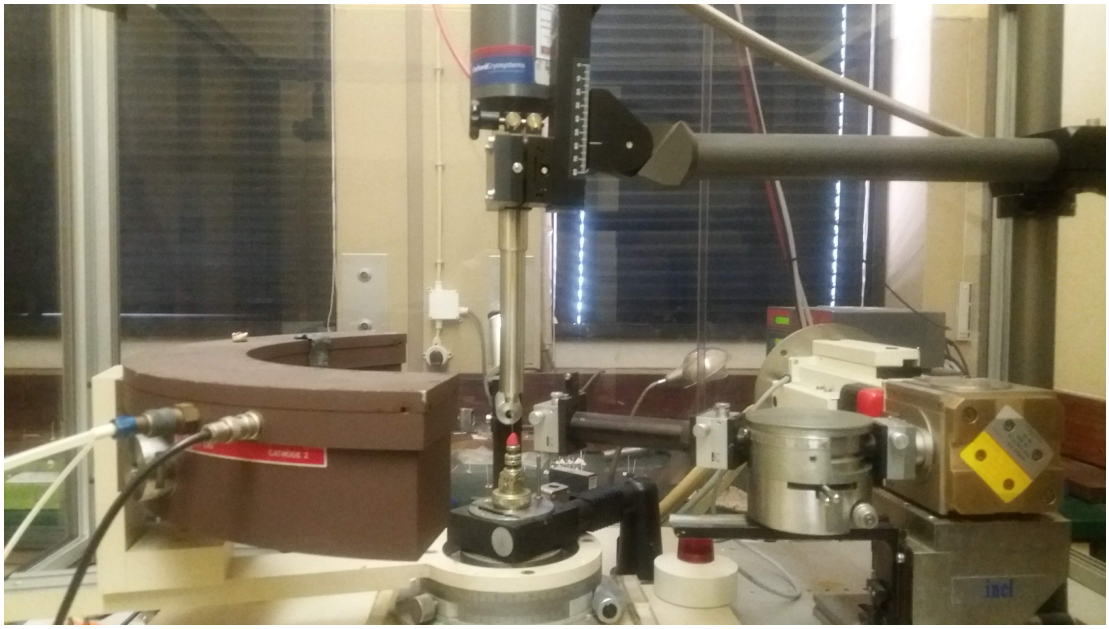

Fig. 5.4 Powder Diffractometer.

The Detector

The detector (INEL CPS 120) has a beryllium entrance window with a height of 10 mm and is 25 μm thick. The detector is filled with a gaseous mixture of 15% ethane and 85% argon at a pressure of 6.2×10^5 Pa and there are two cathodes and one anode. The first cathode, made of copper, is in front of the anode, with a width of 2 mm. The anode, made of steel, was designed as a very thin curved sheet to maximize mechanical stability. The second cathode is formed by several copper strips 2 mm wide separated by a distance of 2.54 mm [28].

Potential differences are applied between the cathodes and the anode. As a result, there is an electric field inside the detector. When a photon interacts with the atoms of the gas, they are accelerated by the electric field and ionize other atoms. In this region of high electric field, the number of released electrons increases very rapidly in an "avalanche" phenomenon. The electric charges created by this process are then collected by the cathode. The different sections of the cathode are connected by a delay line which determines the position of the photons entering the detector.

The difference between the arrival times at each end of the delay line is related to the position of the avalanche in the anode. The charges propagate to the left and right along the line of delay towards the two ends and are collected by two preamplifiers which transform them into current impulses. Following the preamplifiers, there are two constant fraction discriminators that eliminate noise. An amplitude time converter module receives the first signal that activates a clock, while the arrival of the second signal stops the clock, generating a signal with amplitude proportional to the difference between arrival times. This module is connected to a counter, which controls the detector counts. In addition to these modules, the diffractometer also has a high voltage module (9.7 KV) and a PC module that controls the pressure and gas flow in the detector. The acquisition of the diffractogram and its transfer to a computer is performed with a multichannel analyzer (SILENA "VARRO" MCA).

Fig. 5.5 The multichannel analyzer SILENA “VARRO” MCA.

Detector Calibration and Linearization

The detector and other components of the diffractometer are susceptible to changes in position due to shocks and vibrations. For this reason, it is recommended that calibrations and linearity studies be performed with some regularity. In the calibration process, a substance whose diffraction maximum angles are known with precision and that are related to the channels where the diffraction maximum occurs is used.

5.3 Magnetometry

5.3.1 DynaCool Physical Property Measurement System (PPMS)

Fig. 5.6 PPMS Dynacool Magnetometer [29].

In this work, a Physical Property Measurement system (PPMS), the 9T PPMS Dynacool from Quantum Design, was used. This equipment measures properties such as the magnetic moment, resistivity, specific heat, etc., from 1.8 K up to 400 K under magnetic fields up to 9 T, with no need to be supplied with any liquid cryogens as it operates using a closed-cycle He cryostat. A two-stage pulse tube cryocooler is used for both the superconducting magnet and the temperature control system, providing a low vibration environment for sample measurements. The sample chamber's temperature is controlled by a minimum amount of liquid helium produced by the cryocooler, which flows up to cool the sample chamber. The main flow mode and the low temperature mode are two cooling flow modes available in DynaCool.

In the main flow mode, helium gas at 4.2 K in the bucket flows up through the counter-flow heat exchanger (CFE), reaches the mass flow controller and then back down the CFE into the cooling annulus. In this case, temperatures of 10 K are possible. When lower temperatures are needed and the system reaches this temperature, the low temperature mode

is activated instead and the liquid at 4.2 K from the bucket is expanded. Since there are different pressures at the inlet (1 atm) and outlet (10 Torr) of the impedance, some of the helium evaporates resulting in a mixture of liquid and gas that flows to the bottom of the cooling annulus. As the pot begins to fill, the system is simultaneously controlling the level of liquid in the pot as well as the flow rate of gas. The helium is returned to the bucket, being cooled again by the cryocooler so that it be reused [30, 29].

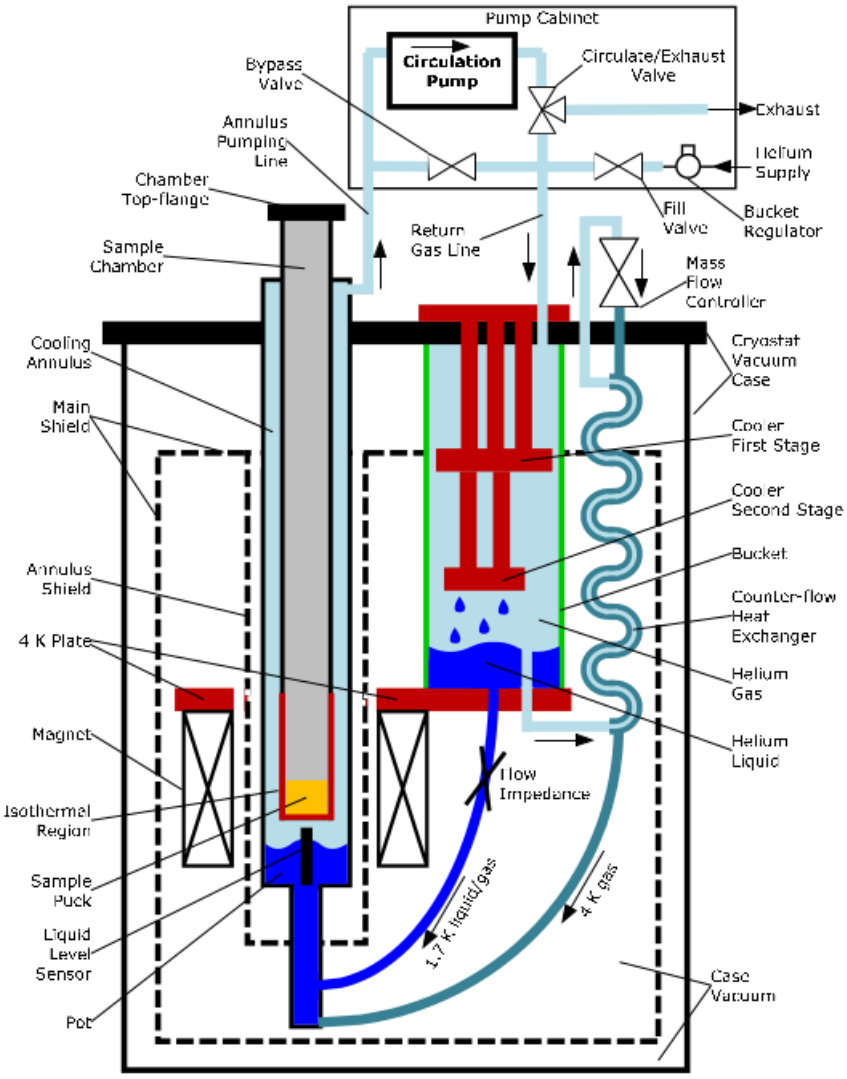

Fig. 5.7 Schematic representation of the Dynacool Cryostat [29].

The magnet system is a TiNb 9 T superconducting coil, whose current is controlled by a hybrid magnet controller. Both the temperature of the magnet and of the cryostat are monitored with the help of thermometers located at different places of the PPMS.

5.3.2 Magnetometry Measurements

Using a vibrating sample magnetometer, it was possible to do the magnetometry measurements, such as the zero-field-cooled/field cooled ZFC/FC susceptibility curves, $M(T)$, and the applied field dependence of the magnetization, $M(H)$.

In a VSM, a sample is vibrated in the vicinity of a set of pick-up coils. The moving magnetic sample causes a flux change. This flux change in turn causes an induction voltage across the terminals of the pick-up coils that is proportional to the magnetization of the sample [31], this is,

$$V(t) = -\frac{d\phi}{dt} \tag{5.14}$$

$$V(t) = -\frac{\partial\phi}{\partial z}\frac{\partial z}{\partial t} \tag{5.15}$$

$$\tag{5.16}$$

where $\phi(t)$ represents the changing flux in the pick-up coils caused by the moving magnetic sample. $z(t)$ is the vertical position of the sample with respect to the coil. If the sample vibrates with frequency ω and amplitude A, the signal will be proportional to the magnetic moment, m, of the sample, this is,

$$V(t) = -kmG(z)\omega A\cos(\omega t) \tag{5.17}$$

Magnetic moments as small as $5\times10^{-4}\,\mathrm{A\,m^2}$ (5×10^{-5} emu) are measurable with a VSM and its accuracy is better than 2% [32]. This method is well suited for the determination of the saturation magnetization M_s.

In this work, all samples were measured with the same frequency, 40 Hz, and oscillation amplitude $A \approx 2\,\mathrm{mm}$, at the central position of coils. $G(z)$ is approximately constant, due to an optimal choice of the value of the ratio of the distance between coils and their radius, $2z_0/a_0 = \sqrt{3}$. The moment is usually reported in emu units (1 emu = 10^{-3} J/T).

5.4 Mössbauer Spectroscopy

5.4.1 Elementary Theory

Mössbauer effect uses recoilless absorption and emission of γ radiation by a nucleus. A source containing ^{57}Co nuclei decays by electron capture to produce an excited state of ^{57}Fe, denoted as Fe**. This nuclide decays to another excited state, denoted Fe*.

These decays to the ground state via a gamma ray cascade which includes a 14.4 keV gamma ray [33]. This gamma ray can excite a transition in the sample being studied if it is absorbed resonantly, so that its energy matches the energy gap in the sample.

However, normally there are changes in the electronic and magnetic environment and these affect the nuclear energy levels by a small ammount, and so resonant absorption occurs only if the environment of the sample ^{57}Fe is chemically identical to that of the emitting ^{57}Fe* nucleus.

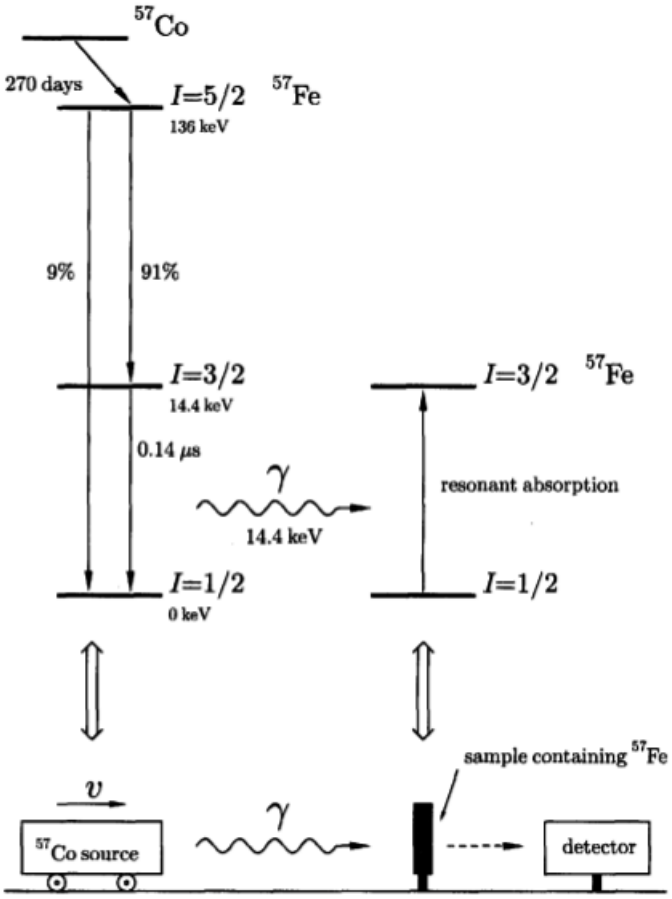

Fig. 5.8 Mössbauer experimental technique [15].

At first, it seems that the energy of γ-ray cannot easily be varied but by moving the source at speed υ it is possible to very slightly adjust the frequency of the γ-ray due to the Doppler effect. The photon has a high frequency and so the Doppler shifts can be quite significant. For example, a velocity of $\upsilon = 1\,\mathrm{m\,s^{-1}}$ leads to a shift of $\mu\upsilon \approx 12\,\mathrm{MHz}$.

A Mössbauer spectrum is a portrait of the resonant absorption peaks that occur as the velocity of the source is changed. The Mössbauer spectrum of a sample containing iron in a single chemical environment is expected to consist of a single line due to absorption of radiation at the energy ΔE required to excite the nucleus from its ground state to the excited state. The isomer shift is the difference between ΔE of the sample and that of metallic ^{57}Fe and is expressed in terms of the velocity that is required to achieve resonance by the Doppler shift.

The value of ΔE depends on the magnitude of the electron density at the nucleus and this effect is essentially due to *s* electrons. As a result, different oxidation states such as Fe(II), Fe(III) and Fe(IV) can be distinguished, as well as ionic and covalent bonding.

Furthermore, we can see from the Mössbauer spectrum that not one but multiple lines are present. This can be due to quadrupole splitting or magnetic splitting. The first effect is due to the electric quadrupole moment of the excited ^{57}Fe nucleus. Although the ground state of ^{57}Fe has $I = \frac{1}{2}$ and thus no electric quadrupole moment, the excited state of interest has $I = \frac{3}{2}$ and nuclei with $I > \frac{1}{2}$ and so can have a non-zero quadrupole moment. If an electric field gradient is present in the nucleus, two lines are produced in the Mössbauer spectrum because the interaction between the electric quadrupole moment and the electric field gradient splits the excited $I = \frac{3}{2}$ state into a doublet.

The second effect is due to the interaction between the magnetic field and the nucleus. The $I = \frac{1}{2}$ ground state is split into a doublet, and the excited state $I = \frac{3}{2}$ into a quadruplet, leading to six lines in the Mössbauer spectrum [15].

5.4.2 Mössbauer Equipment

Mössbauer spectra were collected in transmission mode using a conventional constant-acceleration spectrometer and a 25 mCi ^{57}Co source in a Rh matrix. The velocity scale was calibrated using $\alpha - \mathrm{Fe}$ foil. The absorber was obtained by gently packing single crystals of the samples into a perspex holder ($\sim 4\,\mathrm{mg/cm^2}$ of natural Fe). Low-temperature spectra were collected using a bath cryostat with the sample immersed in liquid He for measurements at 4.1 K. The spectra were fitted to Lorentzian lines using a nonlinear least-squares method [34]. Isomer shifts relative to metallic $\alpha - Fe$ at room temperature are given.

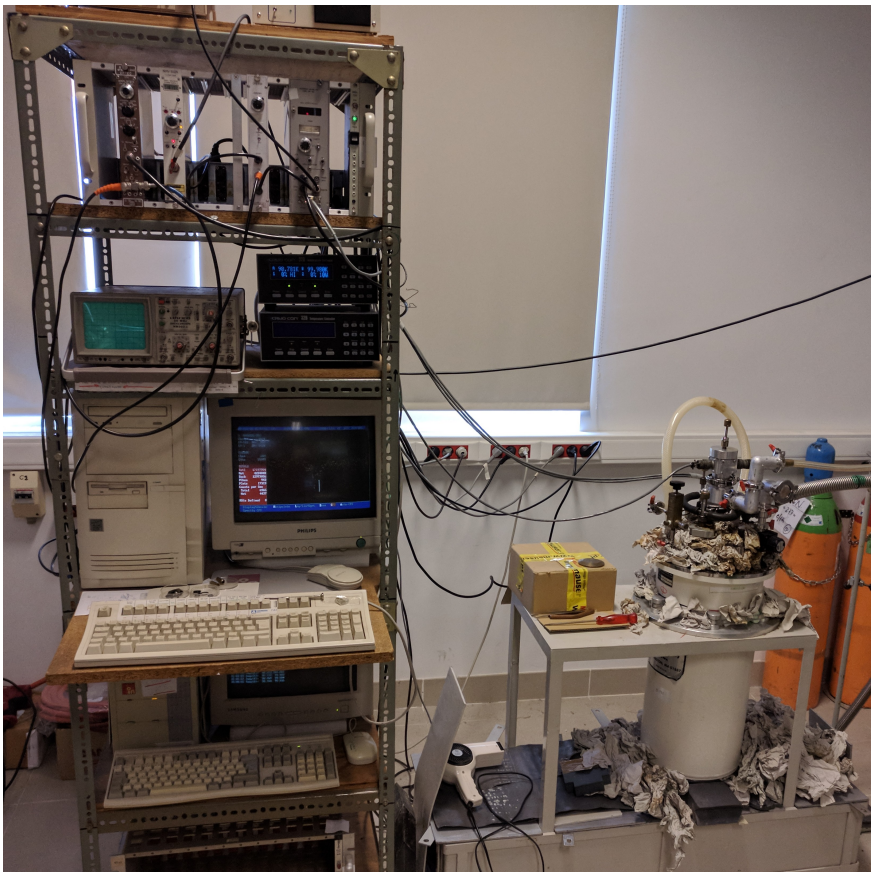

Fig. 5.9 Mössbauer Equipment at CTN.

5.5 Ultraviolet-Visible Spectroscopy

5.5.1 Elementary Theory

Ultraviolet-Visible spectroscopy is the result of electromagnetic radiation absorption by electrons in the UV and visible regions.

The sample is normally a solution but it can also be a gas or solid, which is contained in a cell, known as cuvette, made of an optically transparent material, such as glass, for example.

The beam of the electromagnetic radiation is split into two. One beam of the incident radiation passes through the sample and the other beam through a identical cuvette without a sample [11].

The detector, a photodiode, compares the emerging beams and the UV-Visible absorption is obtained as a function of wavelength.

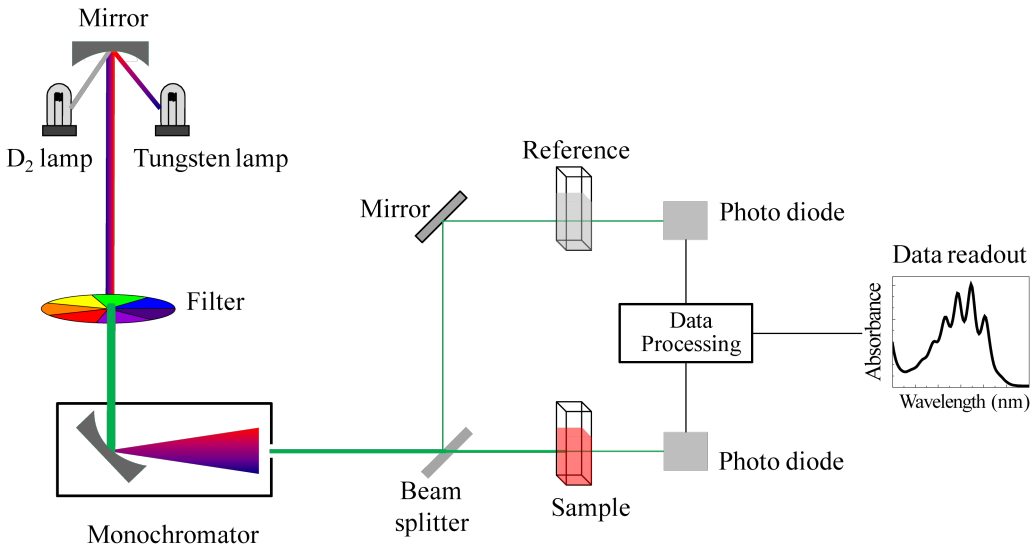

Fig. 5.10 A simple schematic representation of UV-Vis spectroschopy [35].

The intensity of absorption is measured as the absorbance, A, and it can be written as

$$A = \log_{10}\left(\frac{I_0}{I}\right), \tag{5.18}$$

where I_0 is the incident intensity and I is the measured intensity after passing through the sample.

The relation between the absorbance to the molar concentration of the absorbing species and the optical pathlength L is given by the Beer-Lambert law

$$A = \varepsilon cL, \tag{5.19}$$

where ε is the molar absorption coefficient.

5.5.2 UV-Vis Equipment

The source of the spectrophotometer used was a DH-2000-BAL (*Balanced Deuterium Halogen Light Source for the UV-Vis-NIR*) [36]. The DH-2000 is ideal for measuring a variety of different samples. Source details:

- A filtering that eliminates D-alpha line.

- A balanced output from 215 to 2500 nm that eliminates problems associated with saturation.
- A powerful and stable deuterium (25 W) and halogen lamps (20 W) in a single light source.
- An integrated shutter that helps to protect light-sensitive samples.

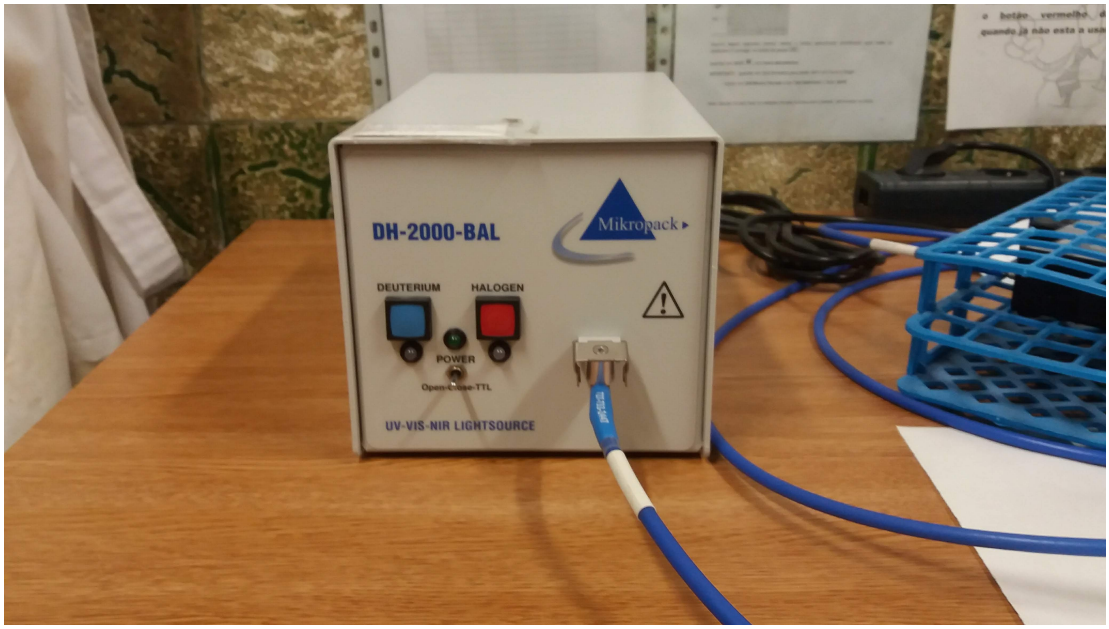

Fig. 5.11 Source DH-2000-BAL of the spectrophotometer.

The absorption plots were observed in the SpectraSuite program. The SpectraSuite can perform three spectroscopic experiments – absorbance, reflectance and emission – as well as absolute irradiance, color and chemical concentration. The program has also signal-processing functions like electrical dark-signal correction and stray light correction. The software provides real-time display of data that allows users to evaluate the effectiveness of their experimental setups, change the parameters and save data [36].

Chapter 6

Crystal Synthesis and Growth

In this chapter, the syntheses of various transition metal compounds with different types of organic ligands will be described. The experimental technique used for the synthesis of crystals was the process of evaporation of the solvent at room temperature. Besides the cases where it was possible to synthesize good quality crystals, some of the failed attempts, which did not form single crystals, will be described.

6.1 Experimental Technique

The evaporation of the solvent at room temperature is one of the simplest crystal growth techniques. In this process, the reagents are mixed in a solvent or a mixture of solvents, until their dissolution. Once homogeneously mixed in a clear solution, solvent evaporates until crystals are obtained, without allowing total evaporation.

Once the crystals are obtained, a perfect single crystal is selected from the obtained material. This single crystal is selected using optical microscopy. Thereafter, it is necessary to mount it so as not to interfere with the diffraction pattern during the X-ray incidence. To overcome this obstacle, the holder of the single crystal is made of plasticine with a glass needle. The sample is then ready to be placed on the diffractometer.

6.2 Synthesis

The objective of this project is to obtain metallic complexes which display magnetic interactions. For this to happen, it is necessary that within the solution, the organic ligand binds to the metallic ion and that the counterion is also aggregated. Metal compounds of manganese, copper, iron and cobalt, known to originate new complexes exhibitting interesting

magnetic properties, were used. The choice of the neutral organic ligands was mainly due to factors such as possible coordination modes and the number of known success cases. All the reagents used were bought from Sigma-Aldrich. The most used solvents were distilled water (H_2O) and methanol (CH_3OH), but ethanol (C_2H_6O), dichloromethane (CH_2Cl_2) and benzene (C_6H_6) were also used in some cases. In other cases, some drops of nitric acid (HNO_3) were added to the solution. **The metal salts (mostly hydrated) used were:**

- Ferric (III) Chloride Hexahydrate ($FeCl_3 \cdot 6H_2O$)
- Iron (III) Nitrate Nonahydrate ($Fe(NO_3)_3 \cdot 9H_2O$)
- Iron (II) Oxalate Dihydrate ($FeC_2O_4 \cdot H_2O$)
- Iron (III) Sulphate Hydrate ($Fe_2(SO_4)_3 \cdot xH_2O$)
- Manganese (II) Chloride ($MnCl_2$)
- Manganese (II) Chloride Tetrahydrate ($MnCl_2 \cdot 4H_2O$)
- Manganese (II) Acetate Tetrahydrate ($C_4H_6MNO_4 \cdot 4H_2O$)
- Cobalt (II) Nitrate Hexahydrate ($Co(NO_3)_2 \cdot 6H_2O$)
- Copper (II) Chloride ($CuCl_2$)
- Copper (II) Hydroxyfluoride ($Cu(OH)F$)
- Copper (II) Carbonate Monohydrate ($CuCO_3 \cdot Cu(OH)_2$)
- Copper (II) Sulfate ($CuSO_4$)
- Copper (II) Perchlorate Hexahydrate ($Cu(ClO_4)_2 \cdot 6H_2O$)
  (**Attention:** perchlorate salts can be explosive and should be handled with care)
- Copper (II) Nitrate Hydrate ($Cu(NO_3)_2 \cdot 2.5H_2O$)

Fig. 6.1 Transition metal salts used in the synthesis described below.

The neutral organic ligands used in this project were:

- 1,2 - Di(4-pyridyl) ethylene ($C_{12}H_{10}N_2$)
- Nitroterephthalic acid ($C_8H_5NO_6$)
- 2,4,6 - Tri(4-pyridyl)-1,3,5-triazine ($C_{18}H_{12}N_6$)
- 2,2'- Bipyridyl ($C_{10}H_8N_2$)
- Pyridine (C_5H_5N)
- 2,3 - Pyrazine dicarboxylic acid ($C_6H_4N_2O_4$)
- Phenanthroline ($C_{12}H_8N_2$)

Table 6.1 Synthesis using $Cl_3Fe \cdot 6H_2O$ and organic ligands in different proportions.

Reagents	**Solvent**	**Crystals**
0.05 mmol $Cl_3Fe \cdot 6H_2O$ 3×0.05 mmol 1,2 Di (4-pyridyl) ethylene	Methanol and H_2O	White and orange crystals
0.05 mmol $Cl_3Fe \cdot 6H_2O$ 0.05 mmol Nitroterephthalic acid	Methanol, H_2O and HNO_3	Dark orange crystals
0.05 mmol $Cl_3Fe \cdot 6H_2O$ 3×0.05 mmol Nitroterephthalic acid	Methanol, H_2O and CH_2Cl_2	Orange crystals
0.05 mmol $Cl_3Fe \cdot 6H_2O$ 0.05 mmol 2,4,6 -Tri (4-pyridyl)-1,3,5-triazine	Methanol, H_2O and HNO_3	White Crystals
0.05 mmol $Cl_3Fe \cdot 6H_2O$ 6×0.05 mmol 2,4,6 - Tri(4-pyridyl)-1,3,5-triazine	Methanol, H_2O and HNO_3	White Crystals
0.05 mmol $Cl_3Fe \cdot 6H_2O$ $6 \times 0.05 mmol$ 2,2' - Bipyridyl	Methanol, H_2O and HNO_3	Yellow and orange crystals
0.05 mmol $Cl_3Fe \cdot 6H_2O$ 0.05 mmol 2,3 - Pyrazine dicarboxylic acid	Methanol	Did not crystallize
0.05 mmol $Cl_3Fe \cdot 6H_2O$ 0.05 mmol Phenanthroline	Methanol	Orange crystals

Table 6.2 Synthesis using $Fe(NO_3)_3 \cdot H_2O$ and organic ligands in different proportions.

Reagents	**Solvent**	**Crystals**
0.05 mmol FeN_3O_9 0.05 mmol 2,2' - Bipyridyl	Methanol	Red crystals
0.05 mmol FeN_3O_9 3×0.05 mmol 2,2'-Bipyridyl	Methanol	Dark red crystals
3×0.05 mmol FeN_3O_9 0.05 mmol 2,2' - Bipyridyl	Methanol	Red crystals
0.05 mmol FeN_3O_9 0.05 mmol phenanthroline	Methanol	Did not crystallize
0.05 mmol FeN_3O_9 3×0.05 mmol phenanthroline	Methanol	Dark red crystals
3×0.05 mmol FeN_3O_9 0.05 mmol phenanthroline	Methanol	Did not crystallize
0.05 mmol FeN_3O_9 0.05 mmol 2,3 - Pyrazine dicarboxylic acid	Methanol and H_2O	Orange crystals
0.05 mmol FeN_3O_9 3×0.05 mmol 2, 3 - Pyrazine dicarboxylic acid	Methanol and H_2O	Dark red crystals

Table 6.3 Synthesis using $CuCl_2$ using organic ligands in different proportions.

Reagents	**Solvent**	**Crystals**
0.05 mmol $CuCl_2$ 0.05 mmol 2,2' - bipyridyl	Methanol and H_2O	Green crystals
6×0.05 mmol $CuCl_2$ 0.05 mmol 2,2' - bipyridyl	Ethanol and H_2O	Green crystals
0.25 mmol $CuCl_2$ 0.25 mmol Pyridine	Ethanol	Blue crystals
0.05 mmol $CuCl_2$ 0.05 mmol 2,3 - Pyrazine dicarboxylic acid	Ethanol	Did not crystallize
2×0.05 mmol $CuCl_2$ 0.05 mmol 2,3 - Pyrazine dicarboxylic acid	Ethanol	Did not crystallize
0.25 mmol $CuCl_2$ 0.25 mmol Phenanthroline	Methanol	Green crystals formed inside the solution
2×0.25 mmol $CuCl_2$ 0.25 mmol Phenanthroline	Ethanol	Still in solution

Fig. 6.2 Some of the flasks containing the prepared solutions within this project.

Table 6.6 Synthesis of manganese compounds and organic ligands in different proportions.

Reagents	**Solvent**	**Crystals**
0.05 mmol $MnCl_2$ 0.05 mmol 2,2' - Bipyridyl	CH_2Cl_2 and H_2O	Did not crystallize
0.25 mmol $MnCl_2$ 0.25 mmol Pyridine	Ethanol	White crystals
0.25 mmol $MnCl_2$ 0.25 mmol 2,3 - Pyrarzine dicarboxylic acid	Methanol	Yellow crystals
2×0.25 mmol $MnCl_2$ 0.25 mmol 2,3 - Pyrarzine dicarboxylic acid	Methanol	Yellow crystals
0.25 mmol $MnCl_2$ 0.25 mmol Phenanthroline	Methanol and H_2O	Still in solution
2×0.25 mmol $MnCl_2$ 0.25 mmol Phenanthroline	Methanol	Yellow crystals formed inside the solution
2×0.25 mmol $MnCl_2$ 0.25 mmol Phenanthroline	Methanol	Yellow crystals
0.05 mmol $MnCl_2 \cdot 4H_2O$ 0.05 mmol 2,3 - Pyrarzine dicarboxylic acid	Methanol	Still in solution
2×0.05 mmol $MnCl_2 \cdot 4H_2O$ 0.05 mmol 2,3 - Pyrarzine dicarboxylic acid	Methanol	Yellow crystals
0.25 mmol $MnCl_2 \cdot 4H_2O$ 0.25 mmol Phenanthroline	Methanol	Yellow crystals
2×0.25 mmol $MnCl_2 \cdot 4H_2O$ 0.25 mmol Phenanthroline	Methanol	Yellow crystals
0.25 mmol $MnCl_2 \cdot 4H_2O$ 2×0.25 mmol Phenanthroline	Methanol	Yellow crystals formed in major quantity
0.05 mmol $C_4H_6MnO_4 \cdot 4H_2O$ 0.05 mmol 2,3 - Pyrarzine dicarboxylic acid	Methanol	Did not crystallize
0.05 mmol $C_4H_6MnO_4 \cdot 4H_2O$ 2×0.05 mmol 2,3 - Pyrarzine dicarboxylic acid	Ethanol and H_2O	Did not crystallize
0.25 mmol $C_4H_6MnO_4 \cdot 4H_2O$ 0.25 mmol Phenanthroline	Methanol	Still in solution
0.25 mmol $C_4H_6MnO_4 \cdot 4H_2O$ 2×0.25 mmol Phenanthroline	Methanol	Did not crystallize

Table 6.4 Synthesis of copper compounds using phenanthroline and 2,3-pyrazine dicarboxylic acid ligands.

Reagents	**Solvent**	**Crystals**
0.05 mmol $CuSO_4$ 0.05 mmol 2,3 - Pyrazine dicarboxylic acid	Methanol	Did not crystallize
0.05 mmol $CuSO_4$ 2×0.05 mmol 2,3 - Pyrazine dicarboxylic acid	Ethanol	Did not crystallize
2×0.05 mmol $CuSO_4$ 0.05 mmol Phenanthroline	Methanol	Did not crystallize
0.05 mmol $CuSO_4$ 2×0.05 mmol Phenanthroline	Ethanol and H_2O	Blue crystals formed inside the solution
0.05 mmol $CuCO_3 \cdot Cu(OH)_2$ 0.05 mmol 2, 3 - Pyrazine dicarboxylic acid	Methanol	Did not crystallize
0.05 mmol $CuCO_3 \cdot Cu(OH)_2$ 0.05 mmol Phenanthroline	Methanol	Did not crystallize
0.25 mmol $Cu(OH)F$ 0.25 mmol 2,3 - Pyrazine dicarboxylic acid	Ethanol and H_2O	Did not crystallize
2×0.25 mmol $Cu(OH)F$ 0.25 mmol 2,3 - Pyrazine dicarboxylic acid	Methanol	Did not crystallize
2×0.25 mmol $Cu(OH)F$ 0.25 mmol Phenanthroline	Methanol	Did not crystallize
0.05 mmol $Cu(NO_3)_2 \cdot 2.5H_2O$ 2×0.05 mmol 2,3 - Pyrazine dicarboxylic acid	H_2O and C_6H_6	Blue Crystals
0.05 mmol $Cu(NO_3)_2 \cdot 2.5H_2O$ 2×0.05 mmol Phenanthroline	Methanol	Green crystals

Table 6.5 Synthesis with $CoN_2O_6 \cdot 6H_2O$, $FeC_2O_4 \cdot 2H_2O$ and $Fe_2SO_4 \cdot xH_2O$ and organic ligands in different proportions.

Reagents	**Solvent**	**Crystals**
0.05 mmol $CoN_2O_6 \cdot 6H_2O$ 0.05 mmol 2,3 - Pyrazine dicarboxylic acid	Methanol and H_2O	Orange crystals
2×0.05 mmol $CoN_2O_6 \cdot 6H_2O$ 0.05 mmol 2,3 - Pyrazine dicarboxylic acid	Methanol	Orange crystals
2×0.05 mmol $CoN_2O_6 \cdot 6H_2O$ 0.05 mmol Phenanthroline	Methanol	Orange crystals
2×0.05 mmol $CoN_2O_6 \cdot 6H_2O$ 0.05 mmol Phenanthroline	Methanol and H_2O	Still in solution
2×0.05 mmol $FeC_2O_4 \cdot 2H_2O$ 0.05 mmol 2,3 - Pyrazine dicarboxylic acid	Methanol and H_2O	Red crystals formed inside the solution
0.05 mmol $FeC_2O_4 \cdot 2H_2O$ 0.05 mmol Phenanthroline	Methanol	Red crystals
0.05 mmol $Fe_2(SO_4) \cdot xH_2O$ 0.05 mmol 2,3 - Pyrazine dicarboxylic acid	Methanol and H_2O	Black crystals
0.05 mmol $Fe_2SO_4 \cdot xH_2O$ 0.05 mmol Phenanthroline	Methanol	Red crystals on yellow background
0.05 mmol $Fe_2SO_4 \cdot xH_2O$ 3×0.05 mmol Phenanthroline	Methanol and H_2O	Red crystals formed inside the solution

Table 6.7 Synthesis using $Cu(ClO_4)_2 \cdot 6H_2O$ and organic ligands in different proportions.

Reagents	**Solvent**	**Crystals**
0.05 mmol $Cu(ClO_4)_2 \cdot 6H_2O$ 0.05 mmol 2,3 - Pyrazine dicarboxylic acid	Methanol	Blue Crystals
2×0.05 mmol $Cu(ClO_4)_2 \cdot 6H_2O$ 0.05 mmol 2,3 - Pyrazine dicarboxylic acid	CH_2Cl_2 and H_2O	Blue Crystals
0.05 mmol $Cu(ClO_4)_2 \cdot 6H_2O$ 2×0.05 mmol 2,3 - Pyrazine dicarboxylic acid	Methanol	Blue crystals
0.25 mmol $Cu(ClO_4)_2 \cdot 6H_2O$ 0.25 mmol Phenanthroline	Methanol	Green Crystals
2×0.25 mmol $Cu(ClO_4)_2 \cdot 6H_2O$ 0.25 mmol Phenanthroline	Methanol and H_2O	Blue crystals
0.25 mmol $Cu(ClO_4)_2 \cdot 6H_2O$ 2×0.25 mmol Phenanthroline	Methanol and H_2O	Green crystals formed inside the solution

Of these various experiments, four gave good quality crystals confirmed by X-ray diffractometry or by powder diffractometry:

- $FeCl_3 \cdot 6H_2O + C_{12}H_8N_2$ + Methanol
- $FeN_3O_9 + C_{10}H_8N_2$ + Methanol
- $Cu(ClO_4)_2 \cdot 6H_2O + C_{12}H_8N_2 + H_2O$ + Methanol
- $CuCl_2 + C_5H_5N$ + Ethanol

In some of the other flasks, the evaporation was not complete and some solution remained. In other flasks, totally evaporated, some residual powder remained but with a matt thin look that indicated amorphous characteristics. In some other flask there was concomitant crystallization of several phases, most likely of the initial reagents. Other samples seemed to have crystallized, but it was not possible to search and check the small crystals since the in-house X-ray diffractometer was not working for most the year. Of these four samples, three had already been reported in literature while the one with the iron nitrate was not. In one of the synthesis (the iron (III) chloride with 1,2 -Di(4-pyridyl) ethylene) single crystals were studied but they did not incorporated the metal ion, and it will be described on the Appendix.

Chapter 7

Results and Discussion

7.1 Introduction

The purpose of this project is the development of new molecular compounds with interesting magnetic properties, based on 3d transition metals. Its execution implies a multitude of tasks, starting from the synthesis and ending up in the modelling of the magnetic properties.

The studies with powder diffraction were made essentially to verify if the compounds were crystalline or amorphous, if they contained one or several phases and if they could be identified by comparison with an international database. Using the powder diffractometer, it was possible to identify two phases that were in the database: Aqua-bis(1,10 - phenanthroline)-copper(II) diperchlorate and Aqua-(1,10 - phenanthroline-N,N')-trichloro iron (III). Dichloro-bis(pyridine-N)-Copper(II) and μ-oxo-bis[bis(2,2'-bipyridyl-N,N'-triaqua-iron(III))] tetranitrate trihydrate methanol solvate were solved using the Bruker Advanced X-ray - APEX II diffractometer. For these two samples, a small crystal was placed on a glass needle and later on the goniometer of the Bruker Advanced X-Ray - APEX II diffractometer. The data was collected using monochromatic Molybdenum radiation, $K_\alpha = 0.71973$ Å. The unit cell was determined within a 10-15 minute collection. The structure was resolved after a collection strategy of approximately 12 hours. Using SHELXS-97 [18], it was possible to determine the structure in question and refine it using the SHELXL-97 [18] program. With the help of the PLATON program [37], an analysis of the structure was carried out as well as the production of images. Most of the hydrogen atoms have been placed in idealized positions and refined together with the atoms to which they are attached.

This chapter is divided into four sub-chapters, consisting of the study of the four synthesized samples.

7.2 Aqua-bis(1,10 - Phenanthroline)-copper(II) diperchlorate

The crystals of this compound were obtained by adding 0.05 mmol of phenanthroline in 20 ml of distilled water and methanol, which were subsequently added to 0.25 mmol of copper(II) perchlorate hexaydrate. After a few weeks, single crystals of green color were obtained.

Fig. 7.1 Crystals of Aqua-bis(1,10 - phenanthroline)-copper(II) diperchlorate.

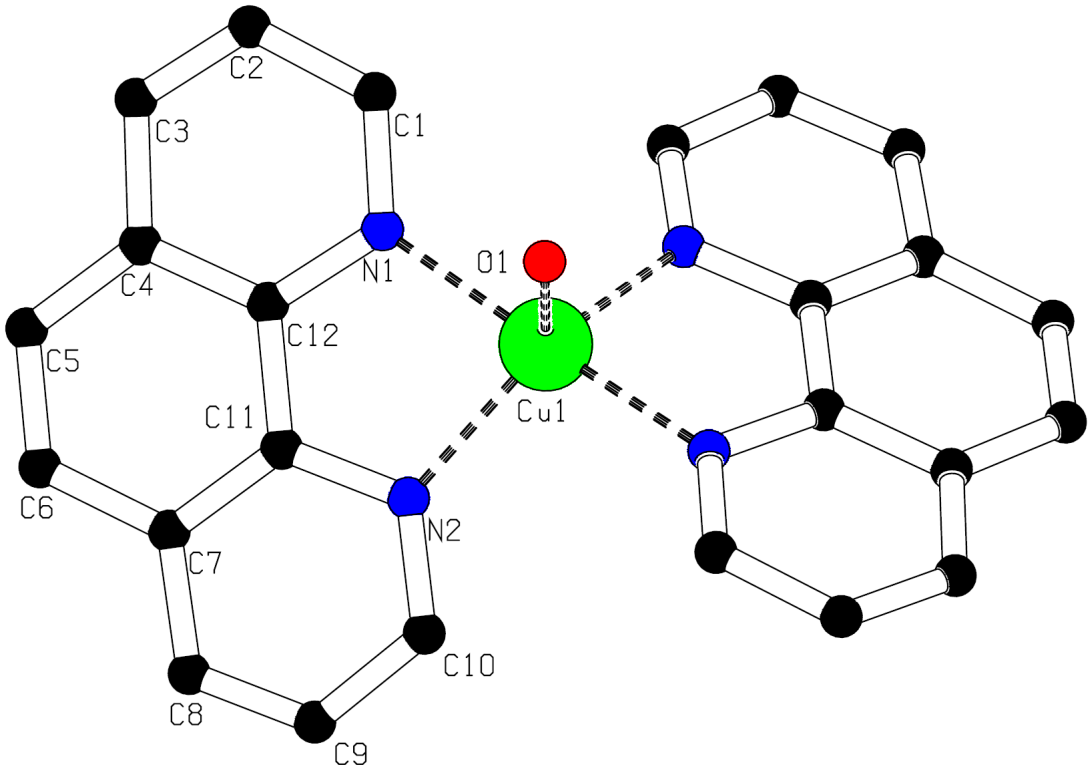

Fig. 7.2 Representation of Aqua-bis(1,10 - phenanthroline)- copper(II) diperchlorate using the PLATON program. Hydrogen atoms and disordered perchlorate ions were omitted for clarity.

Table 7.1 Data collection, refinement and crystal parameters of Aqua-bis(1,10-phenanthroline)-copper(II) diperchlorate as reported in [38].

Compound	$C_{24}H_{20}Cl_2CuN_4O_{13}$
Molecular Weight (g/mol)	706.89
Temperature (K)	283-303
Lattice Type	Monoclinic
Space Group	C2/c
Crystal Data (Å)	
a	19.078(2)
b	8.173(3)
c	16.239(2)
α	90
β	100.14(2)
γ	90
Cell Volume ($Å^3$)	2492.5(10)
Z	4
Density ($g\,cm^{-3}$)	1.8838(8)
$\mu(MoK_\alpha)(mm^{-1})$	1.176
R [I > 2σ(I)]	0.0741

The complex consists of a $[Cu(phen)_2(OH_2)]^{2+}$ cation and two $[ClO_4]^-$ anions and its structure had been reported before by other authors [38]. The metal ion is surronded by 5 atoms: 4 nitrogen atoms and 1 oxygen atom, in a geometry between square-based pyramid and trigonal bipyramid, see figure below. The copper and the water oxygen atom lie on a crystallographic two-fold axis, and the two coordinating organic molecules are symmetry dependent. Two disordered perchlorate ions are associated with each $[Cu(phen)_2(OH)_2]^{2+}$ cation and bonded by hydrogen bonds involving the water H atoms (also disordered). The metal ions are therefore very far apart to allow magnetic interaction and the measured magnetic moment should reflect an isolated paramagnetic behaviour.

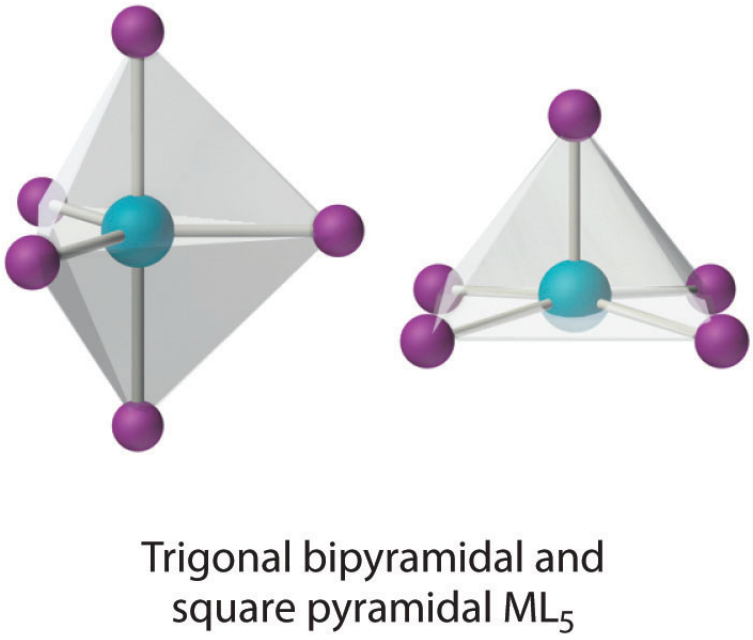

Fig. 7.3 Trigonal bipyramid (left) and Square-based pyradimd (right) geometry [39].

Table 7.2 Atomic coordinates of the atoms.

Atom	x	y	z	Atom	x	y	z
Cu1	0.000000	0.0643(9)	0.250000	O4	-0.14(11)	-0.52(25)	0.1086(8)
N1	0.0943(2)	0.0510(4)	0.3235(2)	O5	-0.236(6)	-0.39(14)	0.159(12)
C1	0.1549(2)	-0.007(5)	0.3043(3)	O6	0.187(13)	0.612(14)	0.3895(7)
C2	0.2176(2)	-0.011(6)	0.3645(3)	O7	0.081(10)	-0.54(21)	0.311(19)
C3	0.2172(2)	0.0412(6)	0.4421(3)	H10	0.010000	-0.28140	0.1972000
C4	0.1541(2)	0.1056(5)	0.4645(3)	N1A	-0.094(2)	0.0510(4)	0.1765(2)
C5	0.1491(3)	0.1676(7)	0.5439(3)	C1A	-0.155(2)	-0.073(5)	0.1954(3)
C6	0.0869(3)	0.2293(7)	0.5600(3)	C2A	-0.218(2)	-0.011(6)	0.1355(3)
C7	0.0237(3)	0.2289(5)	0.4972(3)	C3A	-0.217(2)	0.0412(6)	0.0579(3)
C8	-0.043(3)	0.2878(7)	0.5103(3)	C4A	-0.154(2)	0.1056(5)	0.0355(3)
C9	-0.099(3)	0.2796(8)	0.4470(4)	C5A	-0.149(3)	0.1676(7)	-0.044(3)
C10	-0.091(3)	0.2147(6)	0.3693(3)	C6A	-0.087(3)	0.2293(7)	-0.060(3)
C11	0.0278(2)	0.1656(4)	0.4189(2)	C7A	-0.024(3)	0.2289(5)	0.0028(3)
C12	0.0938(2)	0.1048(5)	0.4017(2)	C8A	0.0428(3)	0.2878(7)	0.0530(4)
N2	-0.029(2)	0.1575(4)	0.3553(2)	C9A	0.0985(3)	0.2796(8)	0.1307(3)
O1	0.00000	-0.210(5)	0.250000	C10A	0.0909(3)	0.2147(6)	0.1307(3)
H1	0.15620	-0.05190	0.241900	N2A	0.0288(2)	0.1575(4)	0.1448(2)

H2	0.26590	-0.05870	0.347600	H9A	0.031700	-0.28140	0.214100
H3	0.26550	0.037700	0.488100	C11A	-0.028(2)	0.1656(4)	0.0811(2)
H4	0.19500	0.165700	0.593500	C12A	-0.094(2)	0.1048(5)	0.0983(2)
H5	0.08420	0.283000	0.620100	H8A	0.136400	0.21190	0.180900
H6	-0.0483	0.333500	0.571200	H7A	0.149100	0.32790	0.043200
H7	-0.1490	0.327900	0.456800	H6A	0.048300	0.33350	-0.07120
H8	-0.1364	0.211900	0.319100	H5A	-0.08420	0.28300	-0.12010
H9	-0.0317	-0.28140	0.285900	H4A	-0.19500	0.16570	-0.09350
Cl1	-0.164(8)	-0.48(16)	0.1832(7)	H3A	-0.26550	0.03770	0.011900
O2	-0.193(3)	-0.625(6)	0.1998(3)	H2A	-0.26590	-0.0587	0.152400
O3	-0.136(5)	-0.38(10)	0.2490(4)	H1A	-0.15620	-0.0519	0.258100

Table 7.3 Bond distances (Å).

Cu1−O1	2.245(4)	N1−C12	1.346(5)
Cu1−N1	1.979(4)	N2−C11	1.359(5)
Cu1−N2	2.033(3)	N2−C10	1.331(7)
Cu1−N1D	1.979(4)	C1−C2	1.406(6)
Cu1−N2D	2.033(3)	C2−C3	1.332(7)
Cl1−O5	1.53(12)	C3−C4	1.419(6)
Cl1−O6A	1.38(12)	C4−C12	1.397(6)
Cl1−O7B	1.66(12)	C4−C5	1.404(7)
Cl1−O2	1.387(5)	C5−C6	1.357(8)
Cl1−O3	1.339(7)	C6−C7	1.436(8)
Cl1−O4	1.41(16)	C7−C8	1.408(8)
O4−O7B	1.590(3)	C7−C11	1.388(6)
O4−O6A	1.370(3)	C8−C9	1.344(8)
O5−O6A	1.330(3)	C9−C10	1.400(8)
N1−C1	1.337(5)	C11−C12	1.426(5)

Table 7.4 Bond angles (°).

O1−Cu1−N1	86.86(10)	Cl1C−O6−O4C	61.60(9)
O1−Cu1−N2	112.0(10)	Cl1C−O6−*O5C*	68.90(9)
O1−Cu1−N1D	86.86(10)	Cl1B−O7−O4B	51.2(10)
O1−Cu1−N2D	112.0(10)	Cu1−N1−C1	127.6(3)
N1−Cu1−*N*2	82.25(15)	Cu1−N1−C12	113.2(3)
N1−Cu1−N1D	173.7(14)	C1−N1−C12	119.1(4)
N1−Cu1−N2D	100.1(15)	Cu1−N2−C11	111.2(3)
N1D−Cu1−N2	100.1(15)	C10−N2−C11	117.7(4)
N2−Cu1−N2D	136.0(14)	Cu1−N2−C10	131.1(3)
N1D−Cu1−N2D	82.25(15)	N1−C1−C2	120.7(4)
O4−Cl1−O7B	61.70(13)	C1−C2−C3	120.4(4)
O5−Cl1−O6A	54.00(12)	C2−C3−C4	120.5(4)
O5−Cl1−O7B	165.6(11)	C5−C4−C12	119.5(4)
O6A−Cl1−O7B	111.9(14)	C3−C4−C12	116.0(4)
O3−Cl1−O4	132.3(10)	C3−C4−C5	124.6(4)
O3−Cl1−O5	99.400(7)	C4−C5−C6	121.0(5)
O2−Cl1−O3	117.20(4)	C5−C6−C7	121.1(5)
O2−Cl1−O4	99.20(10)	C8−C7−*C*11	117.6(4)
O2−Cl1−O5	95.000(5)	C6−C7−C11	118.4(5)
O2−Cl1−O6A	122.90(8)	C6−C7−C8	124.0(4)
O2−Cl1−O7B	96.100(7)	C7−C8−C9	118.7(5)
O3−Cl1−O7B	83.70(10)	C8−C9−C10	121.0(5)
O4−Cl1−O5	107.4(11)	N2−C10−C9	121.7(5)
O3−Cl1−O6A	114.70(6)	C7−C11−C12	120.2(4)
O4−Cl1−O6A	58.90(12)	N2−C11−C7	123.4(4)
Cl1−O4−O7B	67.10(10)	N2−C11−C12	116.4(3)
Cl1−O4−O6A	59.50(10)	C4−C12−C11	119.8(3)
O6A−O4−O7B	117.0(15)	N1−C12−C4	123.3(4)
Cl1−O5−O6A	57.200(8)	N1−C12−C11	116.9(3)
O4C−O6−O5C	122.8(13)		

7.2.1 Powder X-ray Diffraction

Using the rotating capillary technique, in a Debye Scherrer geometry, diffraction data from the powder sample was collected in a few hours. Figure 7.4 shows the intensity versus two-theta measured for this sample. As it is noticeable there is an huge background, that dominates most of the diffractogram, which is common for samples with transition metals, studied with Cu radiation. Since the equipment cannot discriminate in energy all photons are accounted for, those who come from the diffraction beam, those scattered by air and glass and those coming from the metal ions fluorescence.

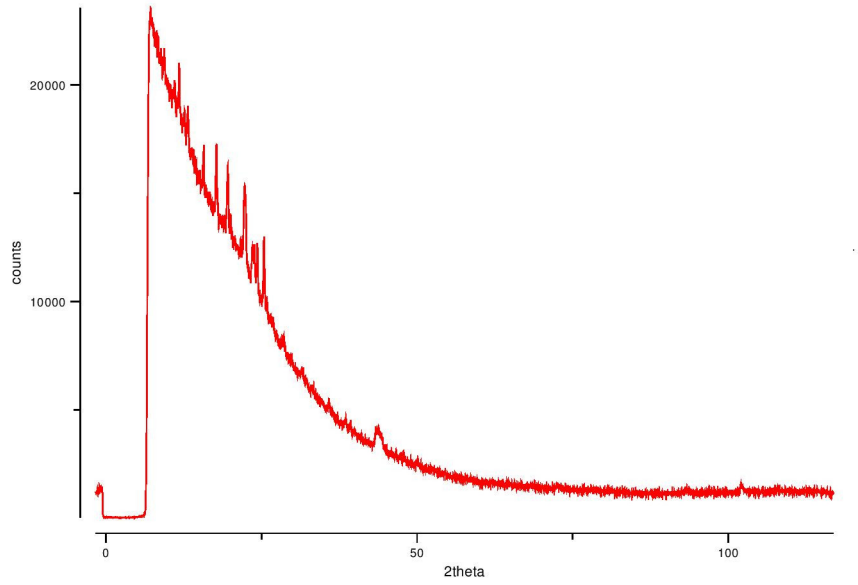

Fig. 7.4 Powder spectra of Aqua-bis(1,10-phenanthroline)-copper(II) diperchlorate.

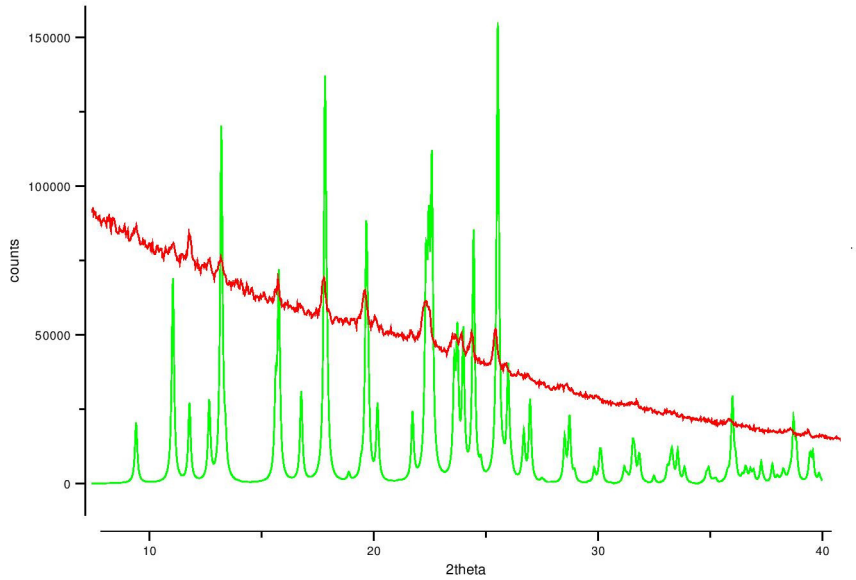

Fig. 7.5 Powder simulation spectra (green) and experimental spectra (red) of Aqua-bis(1,10 -phenanthroline)-copper(II) diperchlorate.

Although the experimental results have a significant background radiation, one can see that the peak positions match those of the powder simulation predicted using single-crystal data.

7.2.2 Magnetometry

X-ray diffraction data elucidate the complex structure and shows that the environment around the Cu^{2+} ion is between a square pyramid and a trigonal bipyramid. Such environments cause a splitting of the crystal field levels as described in the figure below.

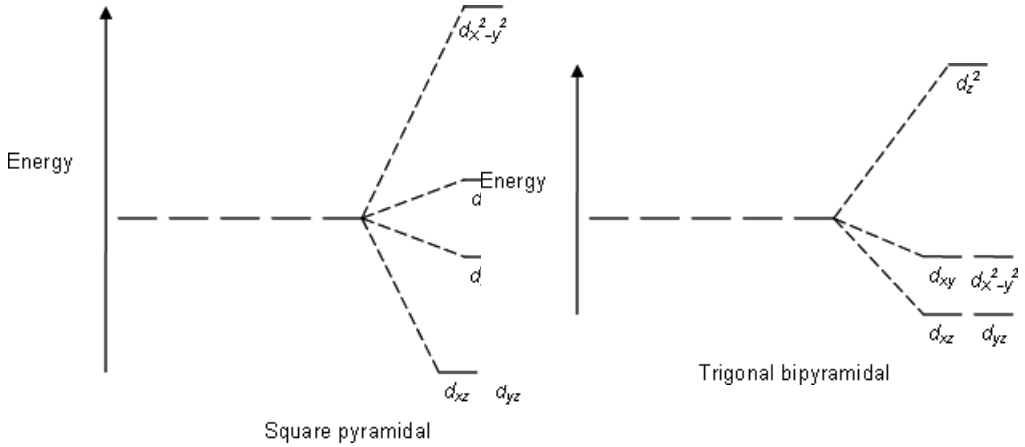

Fig. 7.6 Crystal field splitting for a square pyramidal and a trigonal bipyramidal complex [40, 41].

Since Cu^{2+} contains 9 electrons in the 3d level, all CF levels will contain two electrons with opposite spins, exception for the highest one that it will bare only one electron. Therefore, the total spin of the ion is S=1/2 and should not change with temperature decreasing. In fact in figure 7.11, one can see the stability of the magnetic moment corresponding to a S=1/2 and to a quenching of the angular moment (L=0), as usual in coordinated 3d transition metals.

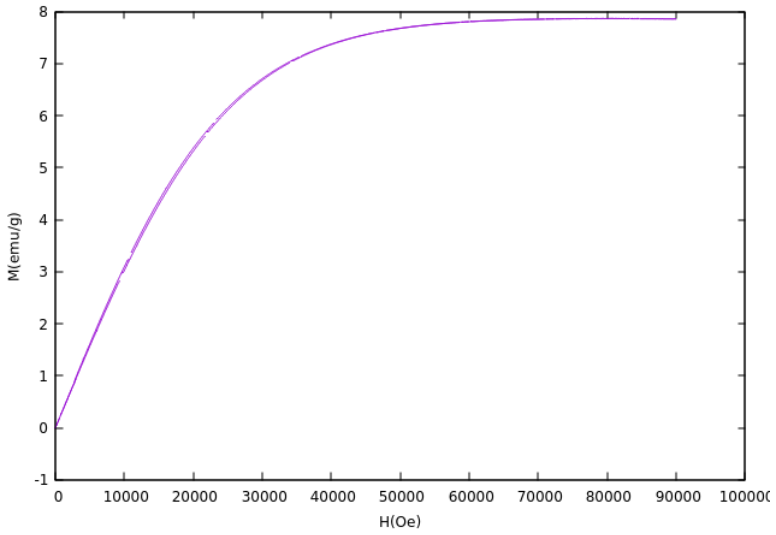

Fig. 7.7 Magnetization (emu/g) as function of field (Oe) at 1.8 K.

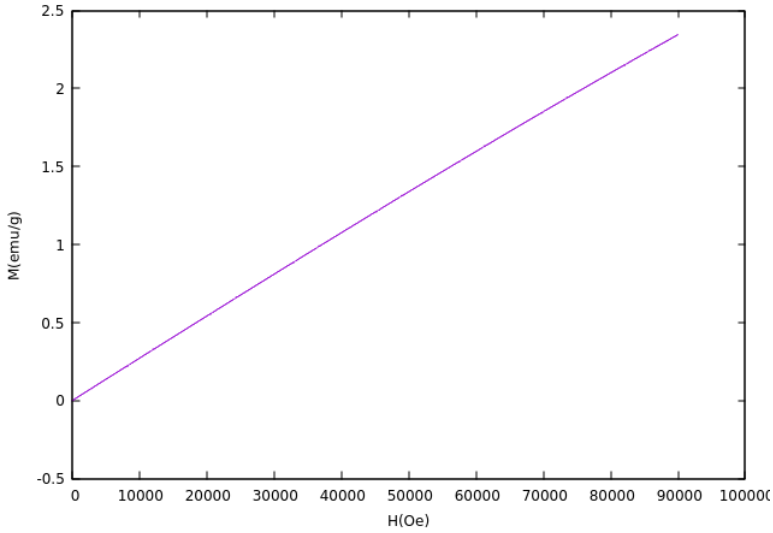

Fig. 7.8 Magnetization (emu/g) as function of field (Oe) at 20 K.

Figure 7.7 and 7.8 show that, in the solid at very low temperature, all the magnetic moment follow the magnetic field, saturating the solid response. With an increasing of the temperature the moments disorder and the saturation value is not achieved.

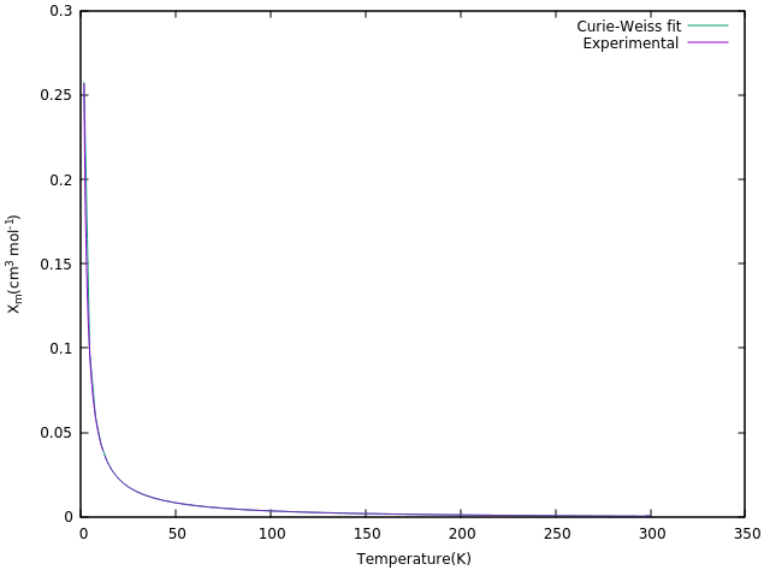

Fig. 7.9 Molar magnetic susceptibility ($cm^3\,mol^{-1}$) as function of temperature (K) measured with an applied magnetic field of 0.5 T.

The sample shows a paramagnetic behaviour. From the Curie-Weiss fit:

$$C = 0.4815 \pm 2.0 \times 10^{-4}\ cm^3 mol^{-1} K \tag{7.1}$$

$$\theta = -0.1123 \pm 0.010\ K \tag{7.2}$$

$$\chi_0 = -0.0014 \pm 1.26 \times 10^{-6}\ cm^3 mol^{-1} \tag{7.3}$$

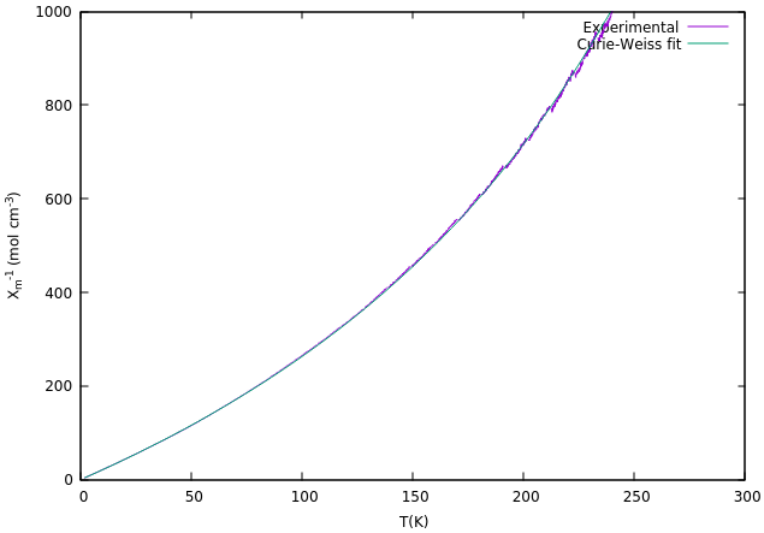

Fig. 7.10 Inverse of molar magnetic susceptibility (mol cm^{-3}) as function of temperature (K).

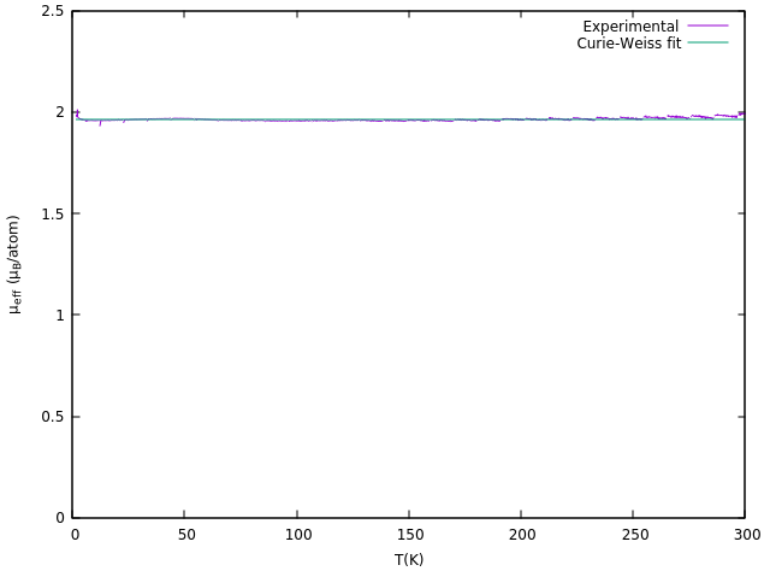

Fig. 7.11 The effective magnetic moment (μ_B/atom) as function of temperature (K) measured with an applied magnetic field of 0.5 T.

The graphic 7.11 shows that the sample has an effective magnetic moment of $\sqrt{\frac{8C}{n}} = 1.96\mu_B$, which is in agreement with the μ_{eff} usually observed for Cu^{2+} [1.70 − 2.20].

Table 7.5 Calculated and experimental magnetic moments [23].

Metallic Ion	$\mu_{\text{eff}_{\text{calc}}}/\mu_B$	$\mu_{\text{eff}_{\text{ob}}}/\mu_B$
Cu^{2+}	1.73	1.70 - 2.20
Fe^{3+}	5.92	5.65 - 6.10

7.3 Dichloro-bis(pyridine-N)-copper(II)

The crystals of this compound were obtained by adding 0.25 mmol of pyridine in 10 ml of ethanol, which were subsequently added to 0.25 mmol of copper(II) chloride. After a few weeks, crystals of blue color were obtained.

Fig. 7.12 Crystals of Dichloro-bis(pyridine-N)-copper(II).

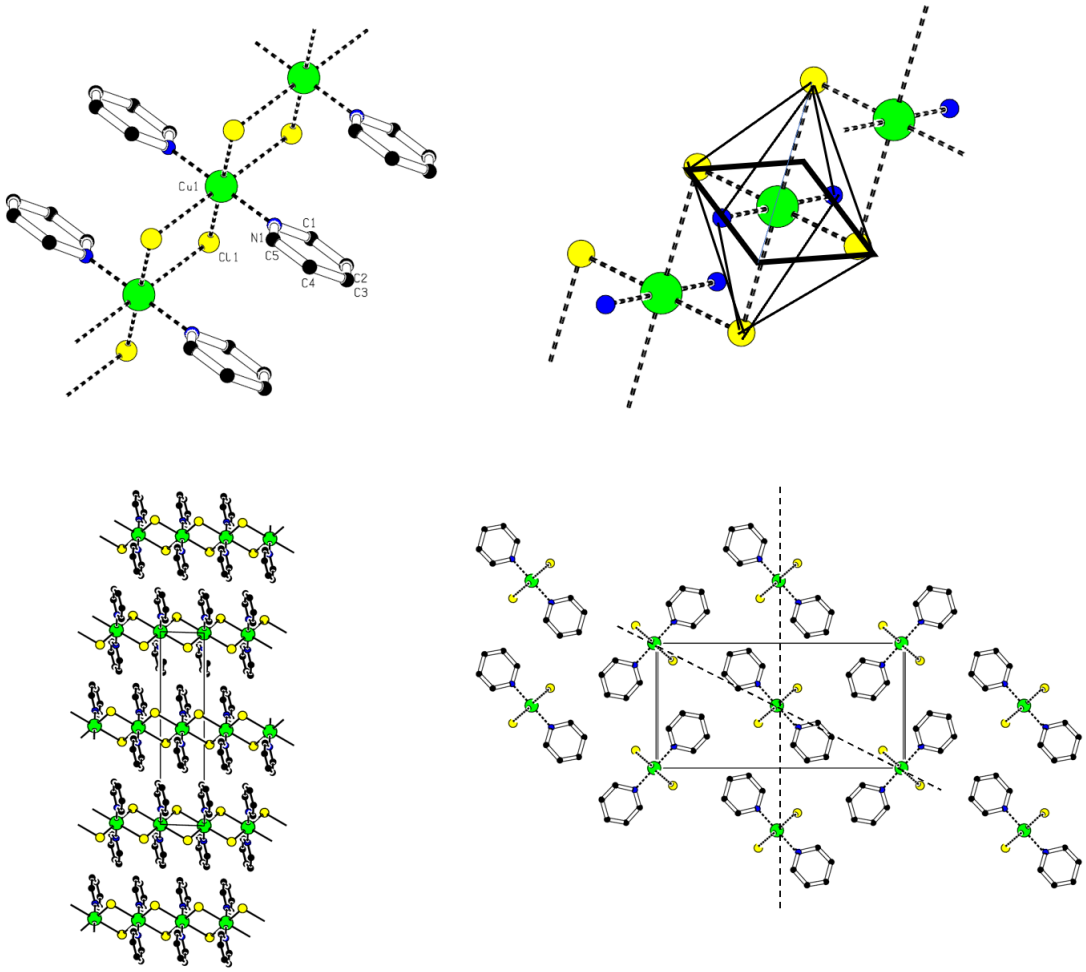

Fig. 7.13 Representation of Dichloro-bis(pyridine-N)-copper(II) using the PLATON *software*. Top left: a portion of the chain with the atomic labelling; Top Right: scheme of the polyhedron around the metal ions. Bottom left: packing of the unit cell viewed along the b axis; Bottom right: the unit cell viewed along the axis with the dashed lines along the 011 and 002 planes.

Table 7.6 Data collection, refinement and crystal parameters of Dichloro-bis(pyridine-N)-Copper(II).

Compound	$C_{10}H_{10}Cl_2CuN_2$
Molecular Weight (g/mol)	292.64
Temperature (K)	293(2)
Lattice Type	Monoclinic
Space Group	P21/c
Crystal Data (Å)	
a	3.854(2)
b	8.547(5)
c	17.278(10)
α	90°
β	100.57°(3°)
γ	90°
Cell Volume ($Å^3$)	559.5(5)
Z	2
Density ($g\,cm^{-3}$)	1.7371(16)
$\mu(MoK_\alpha)(mm^{-1})$	2.394
Diffractometer	Bruker APEX II CCD
Number of reflections	2636
h interval	-4 < 4
k interval	-9 < 10
l interval	-20 < 17
θ interval	2.40 < 26.09
Computing Structure Solution	SHELXS-97
Computing Structure Refinement	SHELXL-97
Number of refined parameters	71
Minum Density ($e^-Å^{-3}$)	-0.436
Maximum Density ($e^{-1}Å^{-3}$)	0.979
χ^2	1.103
R [I > 2σ(I)]	0.0367
wR^2 [I > 2σ(I)]	0.0993

One single crystal was selected under a microscope and diffraction data collected over a few hours. The structure solution and refinement showed an arrangement of the molecules

and ions in linear chains, in a monoclinic system, that has been already reported by others [42–44].

The structure of copper bipyridine dichloride thus consists of polymeric chains in which each metal is surronded by four chlorine atoms and two nitrogen atoms. The coordination around the metal is a distorted octahedron with four bonds in a square coplanar arrangement ($2.0 - 2.3$ Å) and two weaker bonds normal to the plane (3.05 Å). This type of distortion is related to the Jahn-Teller effect (with 9d electrons, the structure is unstable for Cu^{2+} and there is a gain in stability if four coplanar bonds contract and the other two expand).

Each copper ion is bridged to other two copper ions by a double chlorine bridge, the Cl−Cu−Cl angle is circa 92°. The intrachain nearest-neighbor copper ions are separated by 3.87 Åmuch less than the neighbor interchain separation of 8.58 Å, so the magnetic interaction, if any, must be predominantly within each chain.

The chains follow the c-axis as seen in figure 7.13.

Table 7.7 Atomic coordinates.

Atom	x	y	z
Cu1	1.000000	0.5000000	0.000
Cl	0.3027(2)	0.35722(8)	-0.0786(5)
N1	1.0651(7)	0.3271(3)	0.0803(16)
C1	1.2191(9)	0.3537(3)	0.1542(2)
H1	1.304400	0.453800	0.1675000
C2	1.2597(9)	0.2431(4)	0.2118(2)
H2	1.373200	0.266300	0.262800
C3	1.1272(9)	0.0950(4)	0.1922(2)
H3	1.147700	0.016700	0.230200
C4	0.9654(9)	0.0650(3)	0.1163(3)
H4	0.875300	-0.033900	0.101900
C5	0.9386(9)	0.1830(3)	0.0621(2)
H5	0.828300	0.162500	0.010500

Table 7.8 Bond distances (Å).

Cu1 – N1	2.011(3)
Cu1 – N1	2.011(3)
Cu1 – Cl	2.296(11)
Cu1 – Cl	2.296(11)
Cl – Cu1	2.296(11)
N1 – C5	1.341(4)
N1 – C1	1.326(4)
C1 – C2	1.361(5)
C2 – C3	1.383(5)
C3 – C4	1.369(6)
C4 – C5	1.368(5)

Table 7.9 Angles between the bonds (°).

N1 – Cu1 – N1	180.000
N1 – Cu1 – Cl	90.27(8)
N1 – Cu1 – Cl	89.73(8)
N1 – Cu1 – Cl	89.73(8)
N1 – Cu1 – Cl	90.27(8)
Cl – Cu1 – Cl	180.000
C5 – N1 – C1	117.6(3)
C5 – N1 – Cu1	121.3(2)
C1 – N1 – Cu1	121.1(2)
N1 – C1 – C2	123.8(3)
C3 – C2 – C1	118.0(4)
C2 – C3 – C4	119.3(3)
C5 – C4 – C3	118.8(3)
N1 – C5 – C4	122.5(3)

7.3.1 Powder X-ray Diffraction

A portion of the obtained crystals and powder were crushed into a thin powder and placed in a cylindrical glass capillary. The capillary was placed at the center of a Debye-Scherrer diffractometer and the powder diffractogram collected over a few hours, see figure 7.14.

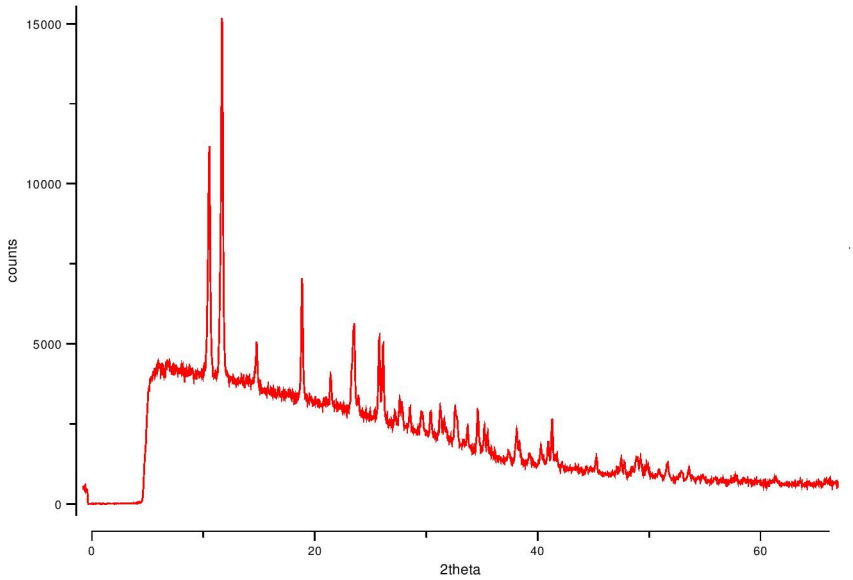

Fig. 7.14 Powder spectra of Dichloro-bis(pyridine-N)-copper(II).

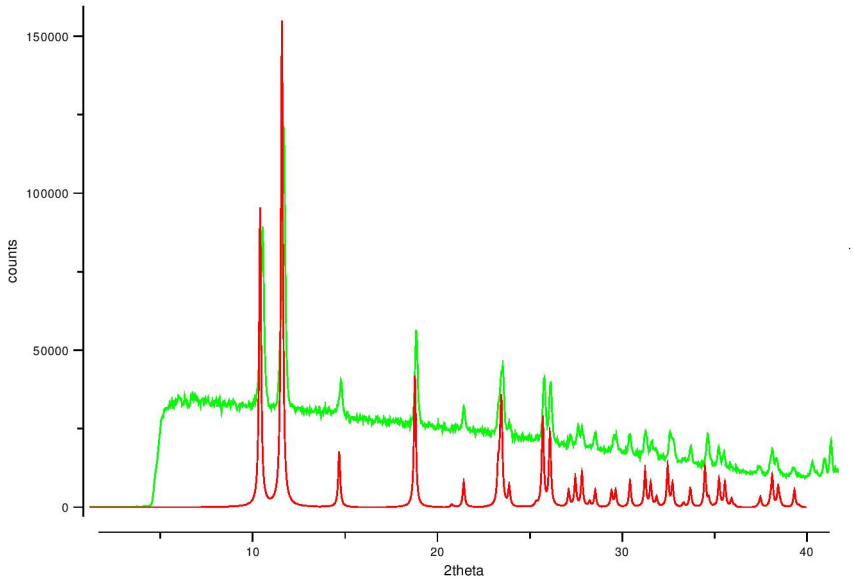

Fig. 7.15 Powder simulation spectra (red) and experimental spectra (green) of Dichloro-bis(pyridine-N)-copper(II).

The experimental results are in agreement with the simulation of the powder diffraction based on single crystal data. The synthesized material is thus a single phase. The two preeminent peaks at low theta [10.41°, 11.54°] correspond to the (002) and (011) reflections,

matching the two families of planes with the highest electron density. The (001) and (010) reflections are absent in the P21/c space group and consequently are not seen in the diffractogram (5.2°; 10.3° respectively).

7.3.2 Magnetometry

An octahedral ligand field surronding the Cu^{2+}, causes a splitting of the 3d orbitals as shown in the following figure:

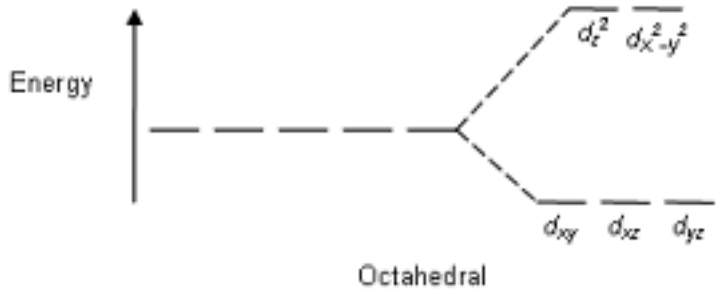

Fig. 7.16 Crystal field splitting for an octahedral complex [45].

With the 9 electrons to distribute to the orbitals, the total spin of the ion S=1/2 and should not change with temperature and applied field, regardless of the ligand field being strong or weak.

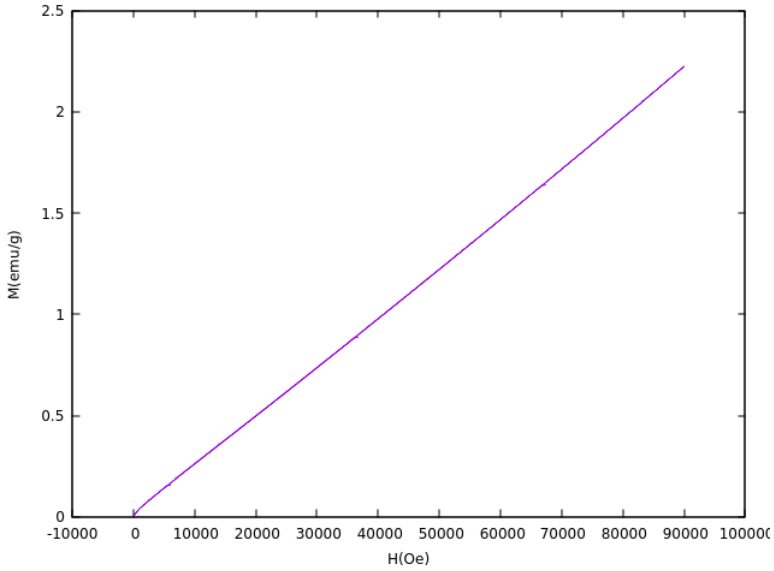

Fig. 7.17 Magnetization (emu/g) as function of field (Oe) at 1.8K.

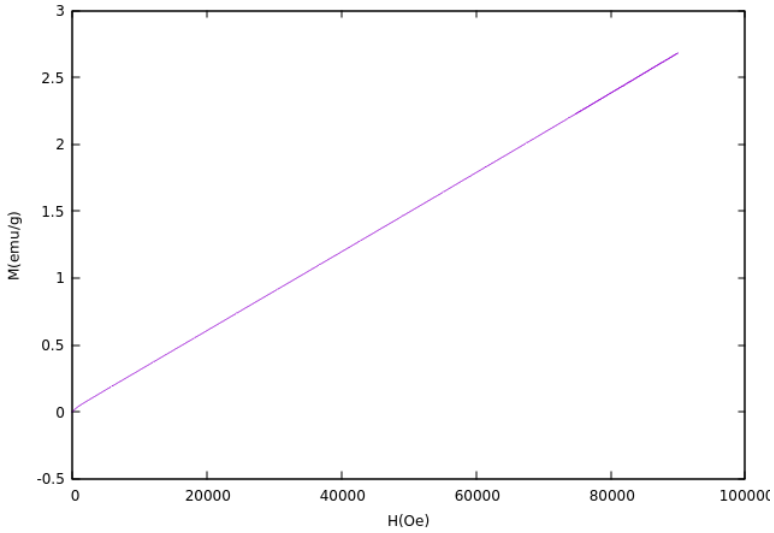

Fig. 7.18 Magnetization (emu/g) as function of field (Oe) at 15K.

The two previous figures show the measured magnetization of the sample as the external magnetic applied field was varied. There is a linear increase without reaching a maximum at the highest applied field.

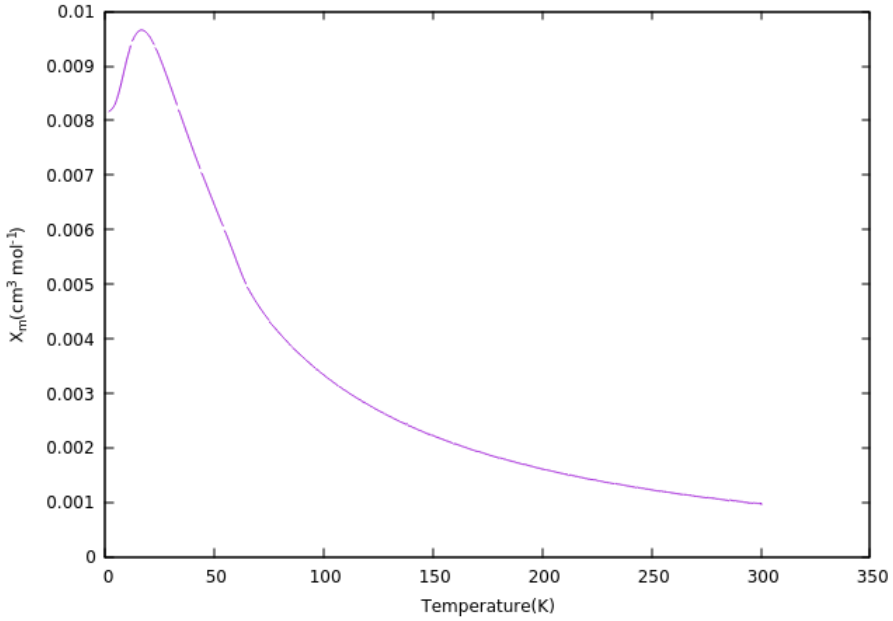

Fig. 7.19 Molar magnetic susceptibility ($cm^3\,mol^{-1}$) as function of temperature (K).

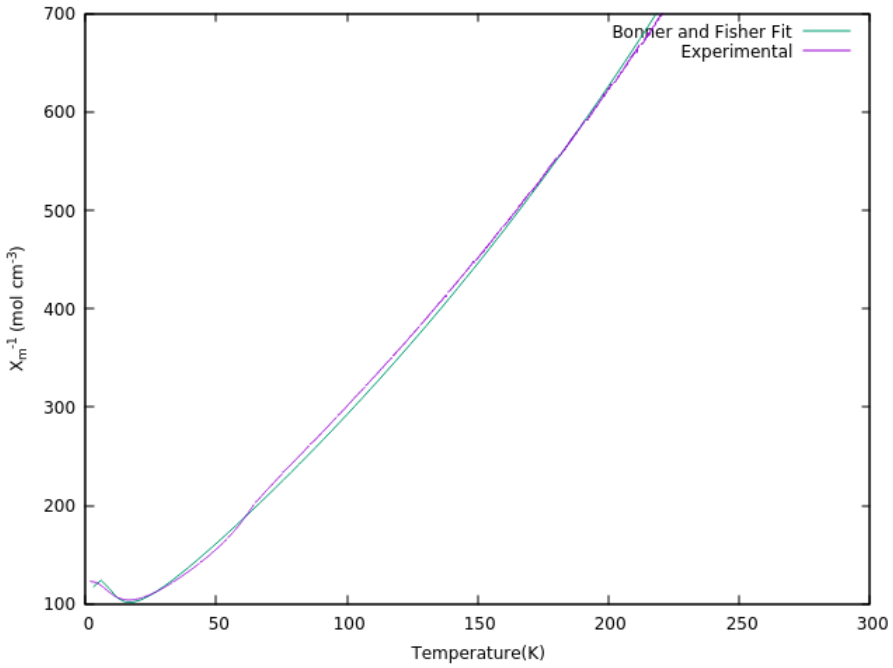

Fig. 7.20 Inverse of molar magnetic susceptibility ($mol\,cm^{-3}$) as function of temperature (K).

From the Curie-Weiss fit:

$$C = 0.513 \pm 0.0027\ cm^3 mol^{-1} K \tag{7.4}$$

$$\theta = -26.3 \pm 0.258\ K \tag{7.5}$$

$$\chi_0 = 7.01 \times 10^{-4} \pm 1.12 \times 10^{-5}\ cm^3 mol^{-1} \tag{7.6}$$

The negative value of θ and the decrease of the susceptibility at low temperatures shows that $catena - CuPy_2Cl_2$ has an antiferromagnetic behaviour, with an antiparallel alignment of the spins. The effective magnetic moment of $2.03\mu_B$ per metal ion is in agreement with the μ_{eff} usually observed for Cu^{2+}.

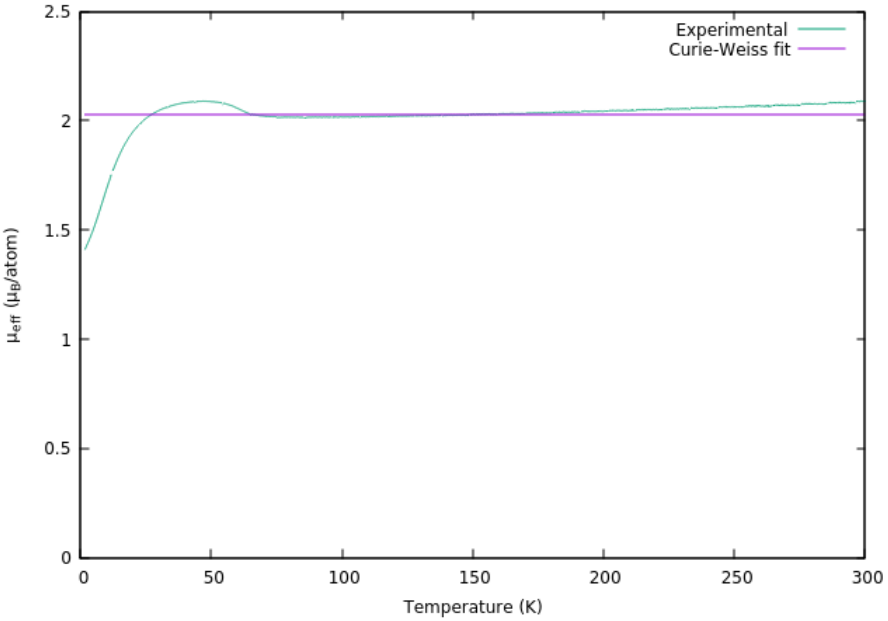

Fig. 7.21 The efective magnetic moment (μ_B/atom) as function of temperature (K).

The fitting of the data (Bonner and Fisher) at the low temperature range yields the value $J/K_B = -12.99 \pm 0.064$ K for the indirect exchange between the metal ions, which is in agreement to those reported by [44].

At the very low temperatures the spins should order like portrayed in the following figure:

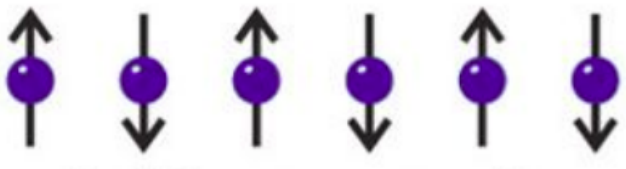

Fig. 7.22 A schematic representation of the antiferromagnetic effect [46].

7.4 Aqua-(1,10-phenanthroline-N,N')-trichloro iron(III)

The crystals of this compound were obtained by adding 0.05 mmol of phenanthroline in 20 ml of methanol, which were subsequently added to 0.05 mmol of iron(III) chloride hexaydrate. After a few weeks, crystals of orange color were obtained.

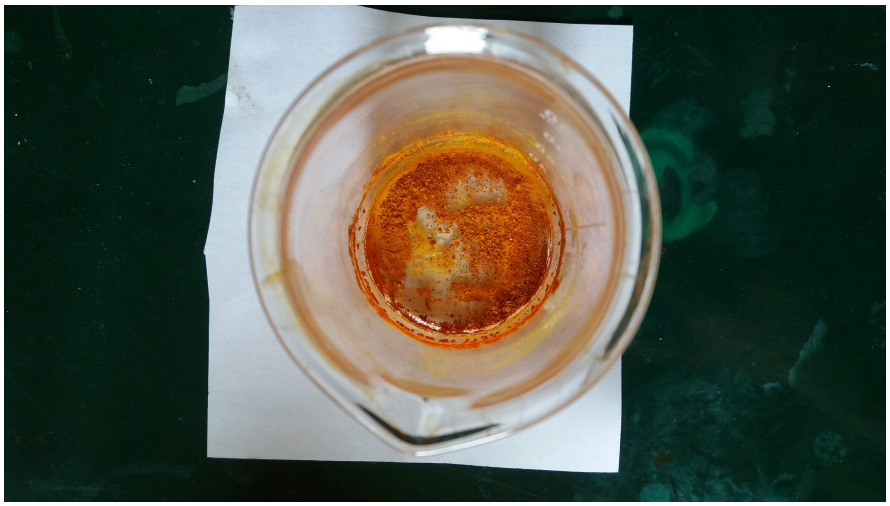

Fig. 7.23 Crystals of Aqua-(1,10 - phenanthroline-N,N')-trichloro iron(III).

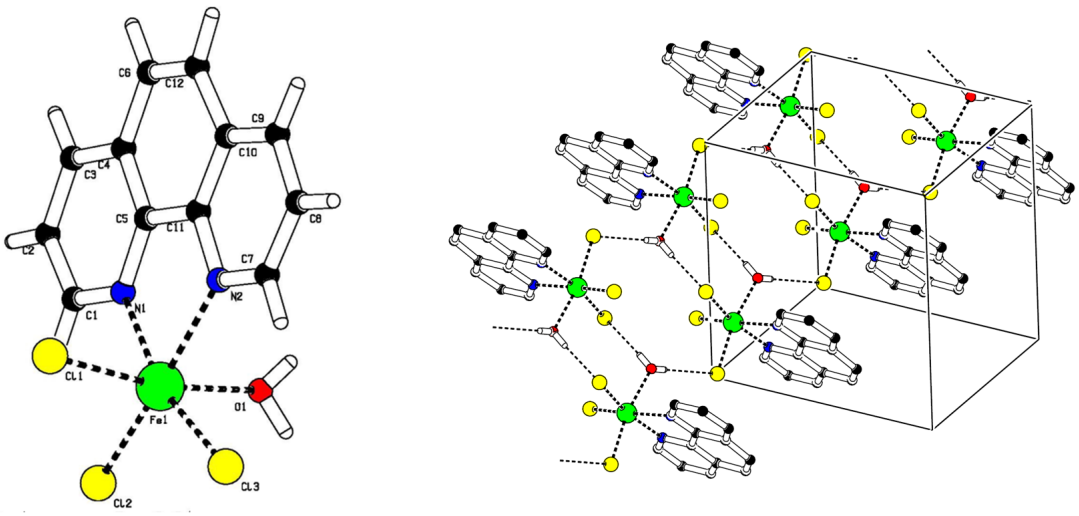

Fig. 7.24 Left: atomic labelling of Aqua-(1,10-phenanthroline-N,N')-trichloro iron(III); right: assembling of the complexes in the solid via H-bonds, depicted as dashed lines.

The crystal structure of the Aqua-(1,10-phenanthroline-N,N')-trichloro iron (III) compound has already been reported [47]. Each asymmetric unit contains one neutral complex

with a six-coordinate iron(III) species, in a distorted octahedral environment, coordinated by one phenanthroline (a bidentate ligand), three chlorine ions and one water molecule. The complexes are joined together by H-bonds: the water hydrogen atoms are shared between the water oxygen and the Cl^- ions. These intermolecular bonds assemble the complexes in double chains that run along the c-axis, see figure 7.24.

Table 7.10 Data collection, refinement and crystal parameters of Aqua-(1,10-phenanthroline-N,N')- Trichloro Iron(III).

Compound	$C_{12}H_{10}Cl_3FeN_2O$
Molecular Weight (g/mol)	360.42
Temperature (K)	283 - 303
Lattice Type	Triclinic
Space Group	P - 1
Crystal Data (Å)	
a	10.591(8)
b	10.227(7)
c	6.613(3)
α	108.21(5)
β	100.69(5)
γ	91.98(6)
Cell Volume ($Å^3$)	665.3(8)
Z	2
Density ($g\,cm^{-3}$)	1.799(2)
$\mu(MoK_\alpha)(mm^{-1})$	1.726
R [I > 2σ(I)]	0.0400

Table 7.11 Atomic coordinates.

Atom	x	y	z
Fe1	0.1534(1)	0.3048(1)	0.098100(2)
Cl1	0.2091(3)	0.2039(3)	0.370300(4)
Cl2	0.1472(3)	0.5228(3)	0.327800(4)
Cl3	-0.060(3)	0.2392(3)	0.006800(5)
O1	0.1373(8)	0.3864(8)	-0.1702(12)
H1	0.146(13)	0.346(12)	-0.270(12)
H2	0.070(11)	0.417(12)	-0.202(19)
N1	0.3588(8)	0.3420(8)	0.1045(12)
C1	0.4992(11)	0.4546(9)	0.2270(15)
H3	0.4050000	0.533000	0.3110000
C2	0.5700(12)	0.4609(11)	0.2360(17)
H4	0.6240000	0.5420000	0.3280000
C3	0.62300(1)	0.3504(13)	0.1117(17)
H5	0.7130000	0.3550000	0.1160000
C4	0.5430(11)	0.2325(10)	-0.0189(17)
C5	0.4106(11)	0.23500(1)	-0.0151(15)
C6	0.5889(10)	0.1103(11)	-0.1447(16)
H6	0.6790000	0.1080000	-0.1430000
N2	0.1960(9)	0.1184(8)	-0.1361(12)
C7	0.1143(10)	0.0079(10)	-0.2556(16)
H7	0.0260000	0.0100000	-0.2480000
C8	0.1532(13)	-0.1106(10)	-0.3917(17)
H8	0.0920000	-0.1870000	-0.4770000
C9	0.2794(13)	-0.1161(10)	-0.4004(17)
H9	0.3070000	-0.1970000	-0.4910000
C10	0.3687(11)	-0.0047(10)	-0.2784(15)
C11	0.3237(11)	0.113600(9)	-0.1450(14)
C12	0.5079(11)	-0.0005(10)	-0.2635(14)
H10	0.5430000	-0.08100000	-0.3430000

Table 7.12 Bond distances (Å).

Fe1−Cl1	2.3370(4)	C2−C3	1.379(17)
Fe1−Cl2	2.2830(4)	C3−C4	1.387(16)
Fe1−Cl3	2.2490(4)	C4−C6	1.426(16)
Fe1−O1	2.1670(8)	C4−C5	1.408(17)
Fe1−N1	2.1860(9)	C5−C11	1.445(15)
Fe1−N2	2.1700(8)	C6−C12	1.328(15)
N1−C1	1.342(13)	C7−C8	1.392(15)
N1−C5	1.336(13)	C8−C9	1.3500(2)
N2−C7	1.331(14)	C9−C10	1.383(16)
N2−C11	1.367(15)	C10−C12	1.457(17)
C1−C2	1.374(17)	C10−C11	1.414(14)

Table 7.13 Bond angles (°).

Cl1−Fe1−Cl2	96.04(12)	N1−C1−C2	122.5(10)
Cl1−Fe1−Cl3	98.66(13)	C1−C2−C3	120.1(10)
Cl1−Fe1−O1	168.80(3)	C2−C3−C4	119.2(10)
Cl1−Fe1−N1	88.800(2)	C3−C4−C5	116.6(10)
Cl1−Fe1−N2	89.000(2)	C3−C4−C6	123.6(11)
Cl2−Fe1−Cl3	98.10(14)	C5−C4−C6	119.8(10)
Cl2−Fe1−O1	89.300(2)	C4−C5−C11	118.7(10)
Cl2−Fe1−N1	92.500(2)	N1−C5−C11	116.9(10)
Cl2−Fe1−N2	167.30(3)	N1−C5−*C*4	124.4(10)
Cl3−Fe1−O1	90.200(3)	C4−C6−C12	120.9(10)
Cl3−Fe1−N1	166.30(2)	N2−C7−C8	122.8(10)
Cl3−Fe1−N2	92.700(3)	C7−C8−C9	119.2(11)
O1−Fe1−N1	81.200(3)	C8−C9−C10	120.5(11)
O1−Fe1−N2	83.900(3)	C11−C10−C12	116.10(9)
N1−Fe1−N2	75.900(3)	C9−C10−C11	118.0(11)
Fe1−N1−C5	115.20(7)	C9−C10−C12	125.8(10)
C1−N1−C5	117.20(9)	N2−C11−C5	117.40(9)
Fe1−N2−C7	127.30(8)	N2−C11−C10	121.30(9)
Fe1−N2−C11	114.30(6)	C5−C11−C10	121.3(11)
C7−N2−C11	118.30(9)	C6−C12−C10	123.1(10)

7.4.1 Powder X-ray Diffraction

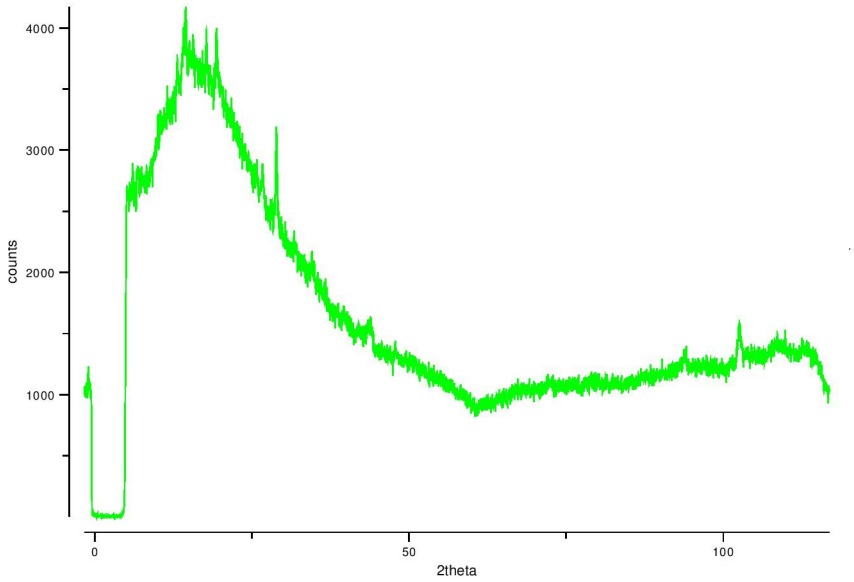

Fig. 7.25 Powder spectra of Aqua-(1,10-phenanthroline-N,N')-trichloro iron (III).

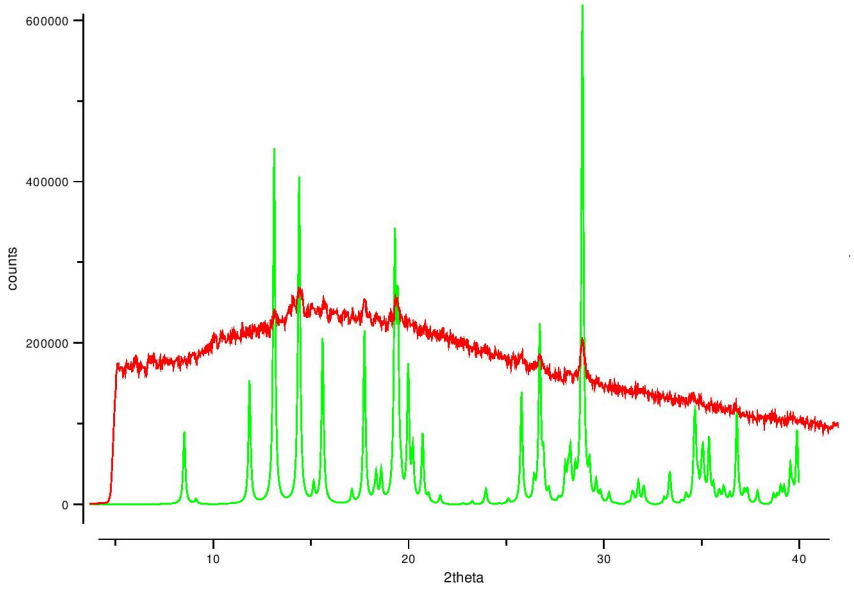

Fig. 7.26 Powder simulation spectra (green) and experimental spectra of Aqua-(1,10-phenanthroline-N,N')-trichloro iron (III).

Although the background radiation is significant, the experimental results are in agreement with the simulation of the powder diffraction.

7.4.2 Magnetometry

For an ion with 5 electrons in the 3d orbital, like Mn^{2+} or Fe^{3+}, in an octahedral environment, two spin states are possible: S=5/2 and S=1/2 depending on the strengthen of the crystalline field, see figure below.

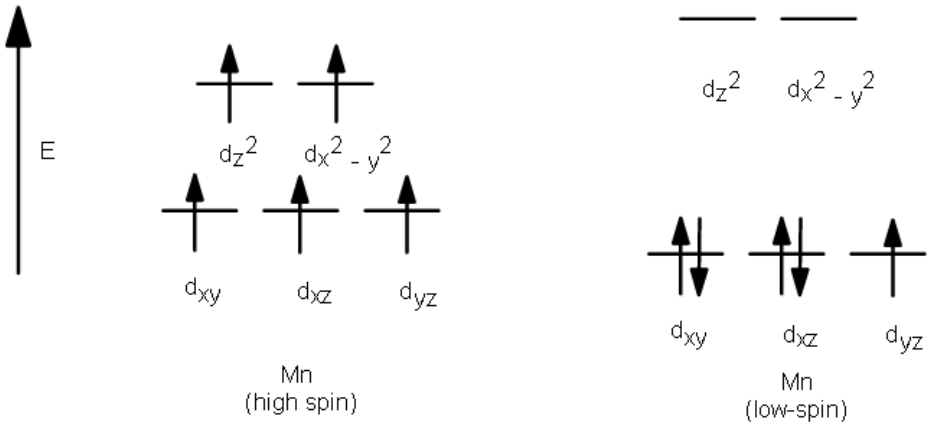

Fig. 7.27 Schematic representation of high spin and low spin for Mn^{2+}/Fe^{3+} [48].

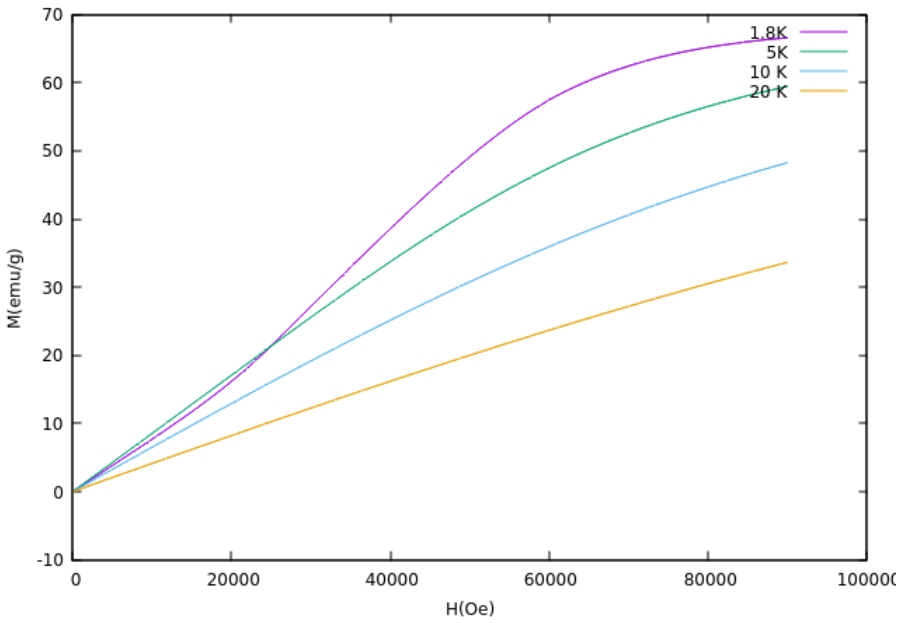

Fig. 7.28 Magnetization (emu/g) as function of field (Oe) at 1.8K, 5K, 10K and 20K.

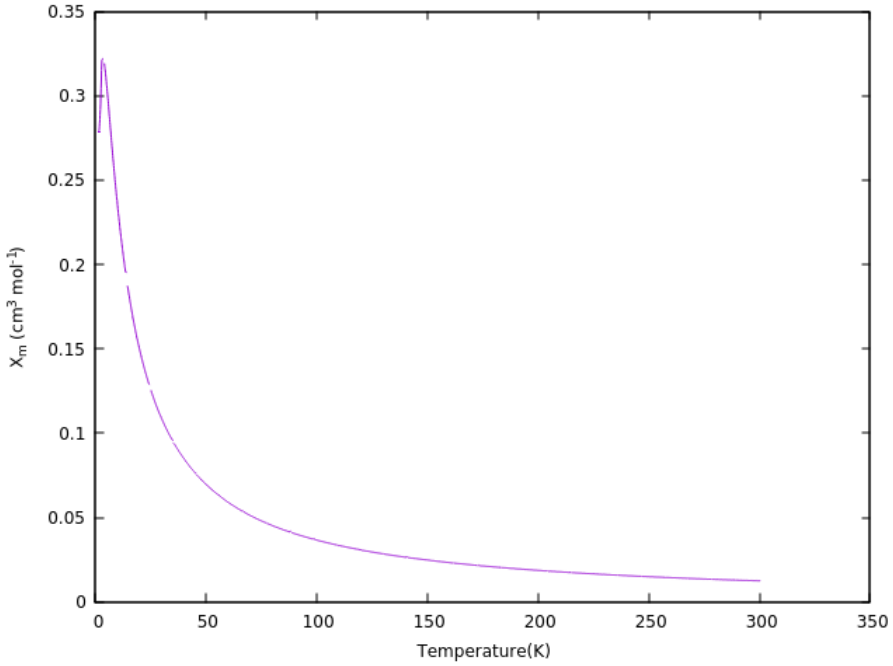

Fig. 7.29 Molar magnetic susceptibility ($cm^3\,mol^{-1}$) as function of temperature (K).

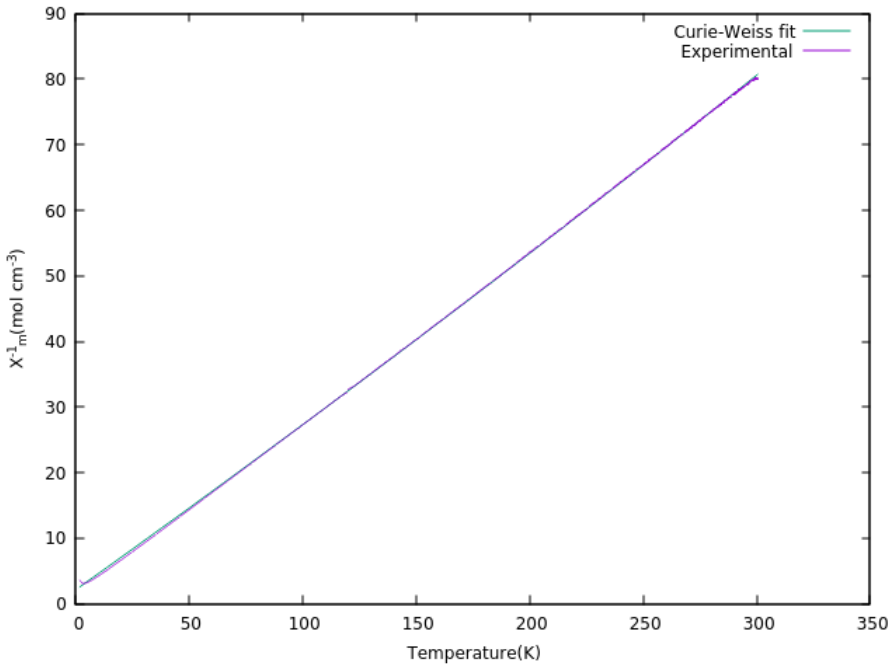

Fig. 7.30 Inverse of molar magnetic susceptibility ($mol\,cm^{-3}$) as function of temperature (K).

From the Curie-Weiss fit:

$$C = 4.06 \pm 3.73 \times 10^{-3}\ cm^3 mol^{-1} K \tag{7.7}$$

$$\theta = -8.50 \pm 6.27 \times 10^{-2}\ K \tag{7.8}$$

$$\chi_0 = -7.34 \times 10^{-4} \pm 1.15 \times 10^{-5}\ cm^3 mol^{-1} \tag{7.9}$$

The value of θ (small and negative) shows that the sample has a weak antiferromagnetic behaviour and an effective magnetic moment of $5.7\mu_B$, which is in agreement with the μ_{eff} predicted for Fe^{3+}, high spin. The interaction between neighbouring spins is conceivable through the path Fe-water-Cl-Fe, an observation already reported for comparable systems [49].

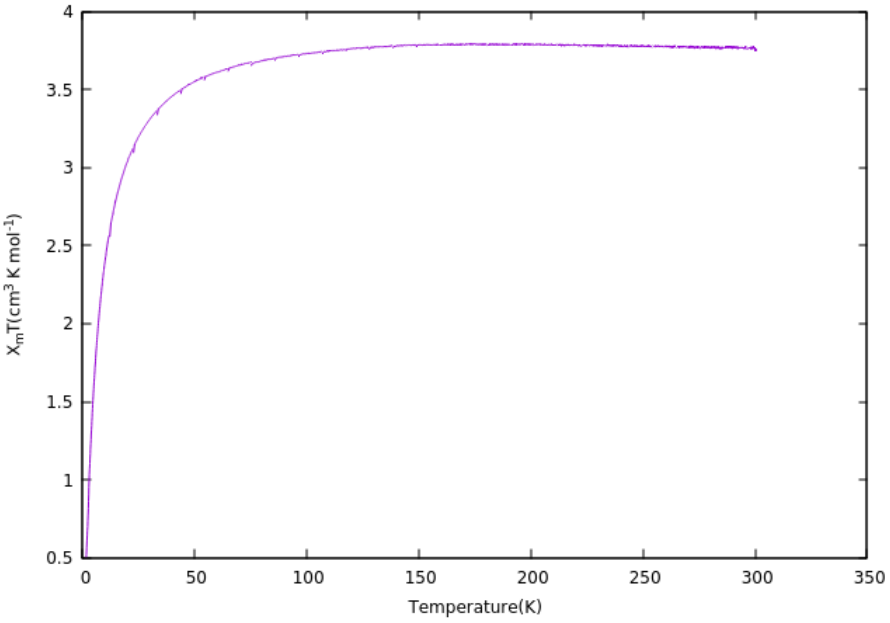

Fig. 7.31 Product of molar magnetic susceptibility and temperature ($cm^3\,K\,mol^{-1}$) as function of temperature (K).

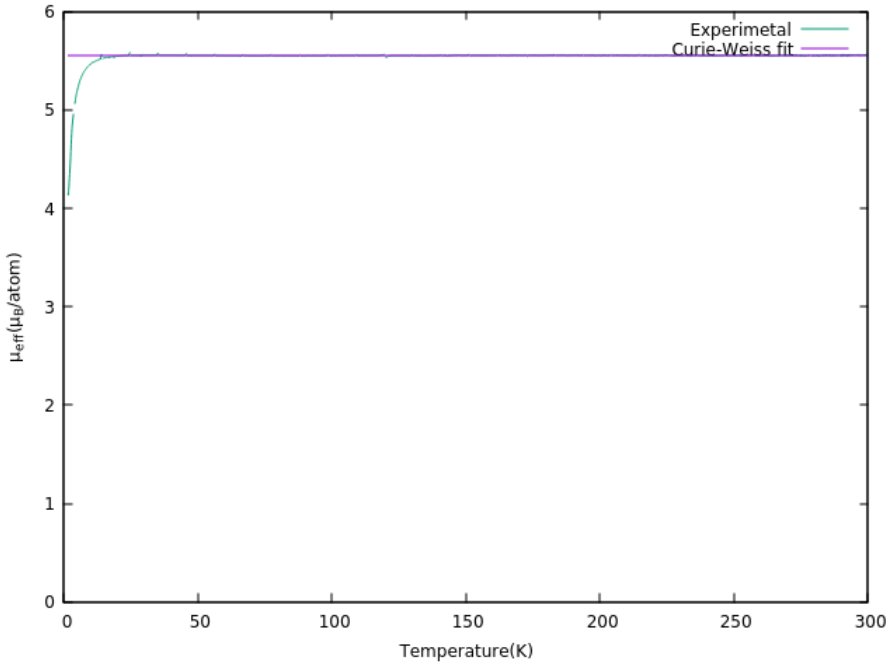

Fig. 7.32 Effective magnetic moment (μ_B/atom) as function of temperature (K).

7.4.3 UV-Visible Spectroscopy

To measure the UV-Vis absorption of this iron complex, two measurements were essayed: one with the solid sample as a thin powder, by spraying a bit of powder into the empty cuvette and fixing it with scoth tape; another with the complex dissolved in methanol.

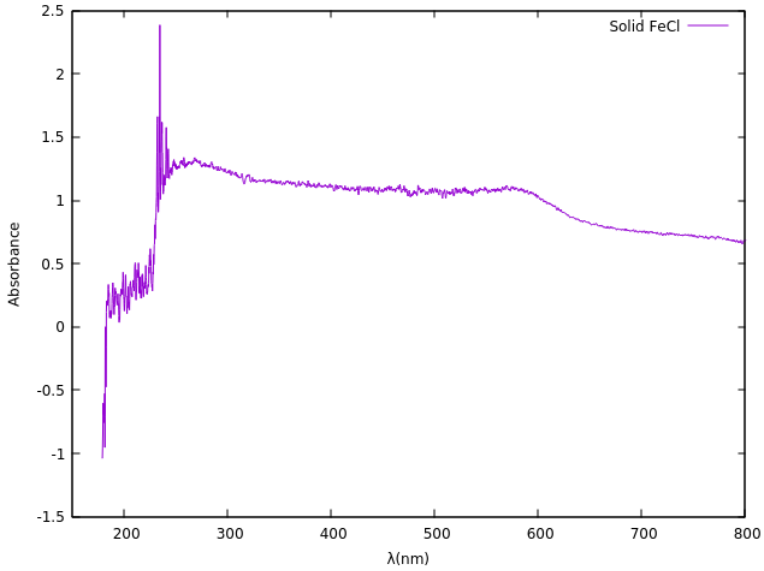

Fig. 7.33 UV-Visible spectra of Aqua-(1,10-phenanthroline-N,N')-trichloro iron (III) in the solid state.

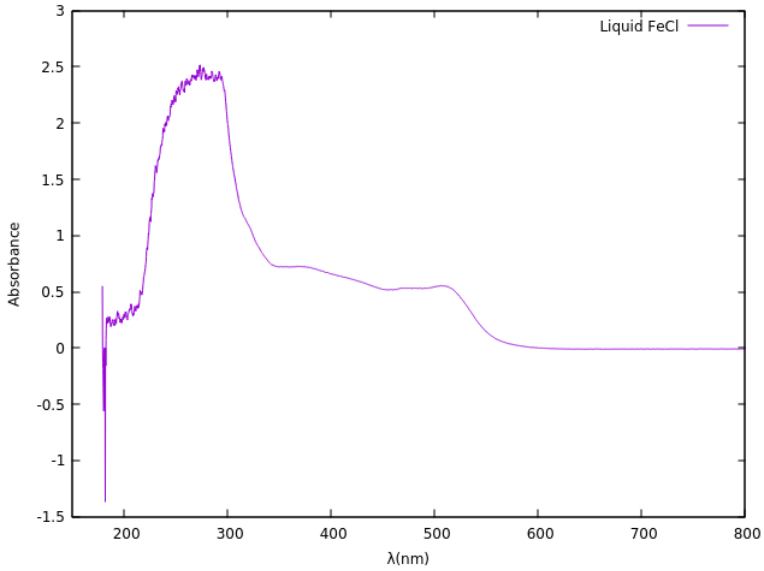

Fig. 7.34 UV-Visible spectra of Aqua-(1,10 - phenanthroline-N,N')-trichloro iron (III) in a solution diluted by methanol.

Both graphs show strong absorption before 300 nm, which is due to the organic ligand (phenanthroline molecules) and another absorption peak between 500 and 600 nm. In the solid form the peak is displaced towards higher wavelengths, that is, smaller energies. This most likely means a rearrangement of the ligands in solution form.

The spectra of the complex in solution shows that the sample absorbs at the region of 510 nm. The crystal field splitting, Δ, can now be calculated, knowing that $h = 6.626\,070\,040(81) \times 10^{-34}\ J\ s^{-1}$, $c = 299\,792\,458\,\mathrm{m\,s^{-1}}$ and $\lambda = 510\,\mathrm{nm}$.

$$\Delta = \frac{hc}{\lambda} = 3.89 \times 10^{-19}\,\mathrm{J} = 2.43\,\mathrm{eV} \tag{7.10}$$

The crystal field splitting value is in agreement with the crystal field splitting usually found in similar compounds.

7.5 Oxo-bridged iron dimer

The crystals of the $\mu - oxo - bis[bis(2,2' - bipyridyl - N,N' - triaqua - iron(III))]$ tetranitrate trihydrate methanol solvate compound were obtained by adding 0.15 mmol of 2,2'-Bipyridyl in 20 ml of methanol, which were subsequently added to 0.05 mmol of iron(III) nitrate nonahydrate. After a few weeks, crystals of red color were obtained.

The complex is dinuclear, the two iron atoms are bridged by an oxygen ion, O^{2-}. Each iron is also coordinated by a bipyridyl molecule and three water molecules, with neutral charge. The complex has thus an overall positive charge of $2 \times (3+) + (2-) = 4+$. For each complex, 4 mononegative nitrate ions, 3 water molecules and one methanol molecule are also present in the unit cell.

Fig. 7.35 Crystals of the oxo-bridged iron dimer.

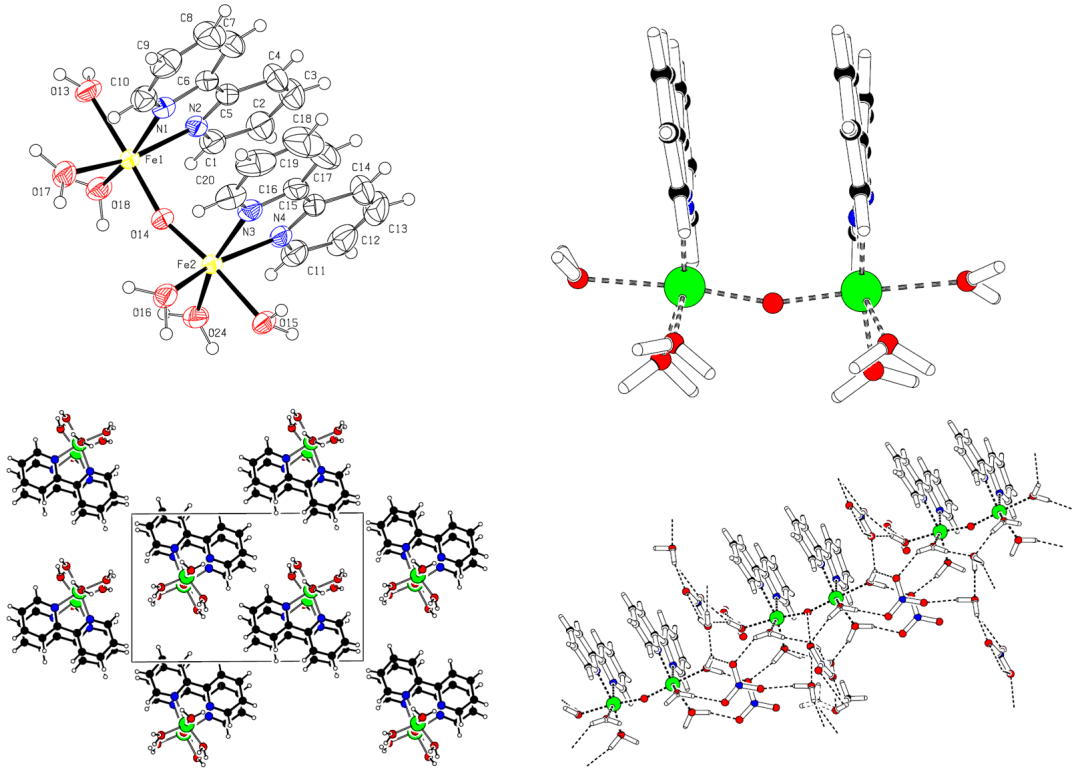

Fig. 7.36 Representation of the oxo-bridged iron dimer with the PLATON program. Top left: ORTEP diagram showing the thermal ellipsoids and the atomic labelling; Top right: a view of the complex showing the oxo-bridged; Bottom right: crystal packing of the iron dimers viewed along a; H-bonds linking molecules and ions portrayed as dashed lines.

Table 7.14 Data collection, refinement and crystal parameters of the oxo-bridged iron dimer.

Compound	$C_{21}H_{38}Fe_2N_8O_{23}$
Molecular Weight (g/mol)	882.29
Temperature (K)	293(2)
Lattice Type	Triclinic
Space Group	P-1
Crystal Data (Å)	
a	10.3001(4)
b	10.9902(4)
c	16.4627(7)
α	88.150(2)
β	83.192(2)
γ	72.016(2)
Cell Volume ($Å^3$)	1760.01(12)
Z	2
Density ($g\,cm^{-3}$)	1.6630(1)
$\mu(MoK_\alpha)(mm^{-1})$	0.926
Diffractometer	Bruker APEX II CCD
h interval	-13 < 13
k interval	-14 < 14
l interval	-21 < 21
θ interval	2.31 < 27.88
Number of reflections	35958
Computing Structure Solution	SHELXS-97
Computing Structure Refinement	SHELXL-97
Number of refined parameters	546
Minimum Density ($e^-Å^{-3}$)	-0.809
Maximum Density ($e^-Å^{-3}$)	1.055
χ^2	1.057
R [I > 2σ(I)]	0.0541
wR^2 [I > 2σ(I)]	0.1459

Table 7.15 Atomic coordinates.

Atom	x	y	z	Atom	x	y	z
Fe1	0.3951(3)	0.4795(3)	0.2248(19)	H13	0.249800	-0.10000	0.114300
Fe2	0.0760(3)	0.4240(3)	0.2365(19)	C14	0.2265(3)	0.0105(3)	0.2130(2)
O13	0.597(19)	0.489(10)	0.21867(6)	H14	0.251000	-0.05570	0.250400
H13A	0.6292(2)	0.539(14)	0.2537(8)	C15	0.1894(2)	0.1367(2)	0.238(17)
H13B	0.671(17)	0.4598(2)	0.1757(10)	C16	0.1824(2)	0.1755(2)	0.324(17)
O14	0.223(13)	0.477(14)	0.22501(9)	C17	0.2207(4)	0.0896(3)	0.3865(2)
O15	-0.11(12)	0.3826(9)	0.25547(5)	H17	0.252500	0.002100	0.376100
H15A	-0.122(4)	0.3420(2)	0.30742(5)	C18	0.2110(4)	0.1358(4)	0.4644(2)
H15B	-0.129(3)	0.327(19)	0.21674(8)	H18	0.235900	0.079200	0.507200
O16	-0.037(8)	0.5762(8)	0.30836(9)	C19	0.1646(3)	0.2653(4)	0.479(19)
H16A	-0.008(9)	0.648(11)	0.3204(19)	H19	0.158000	0.298000	0.531600
H16B	-0.13(11)	0.6136(2)	0.2907(17)	C20	0.1285(2)	0.3441(3)	0.415(16)
O17	0.3432(7)	0.650(10)	0.28310(9)	H20	0.097400	0.431900	0.423900
H17A	0.2534(7)	0.6966(3)	0.3084(2)	O1	-0.137(2)	0.1032(2)	0.064(15)
H17B	0.404(10)	0.6888(2)	0.3039(2)	O2	-0.139(3)	0.1466(3)	0.191(15)
O18	0.4065(7)	0.555(10)	0.10975(7)	O3	-0.183(2)	0.297(18)	0.105(13)
H18A	0.3286(8)	0.5818(2)	0.0793(11)	N5	-0.154(2)	0.1799(2)	0.120(15)
H18B	0.461(11)	0.609(15)	0.0912(2)	O4	0.565(18)	0.721(18)	0.090(14)
O24	0.0156(8)	0.496(10)	0.12641(6)	O5	0.7525(2)	0.5634(2)	0.080(18)
H24A	0.0562(9)	0.555(12)	0.0978(15)	O6	0.7580(3)	0.7426(3)	0.1024(3)
H24B	-0.05(12)	0.4890(2)	0.0931(12)	N6	0.6906(2)	0.676(19)	0.091(14)
N1	0.446(17)	0.370(17)	0.3333(12)	O7	0.8308(4)	0.2076(5)	0.5104(3)
N2	0.485(17)	0.289(17)	0.1809(12)	O8	0.8456(4)	0.2381(4)	0.3912(3)
N3	0.135(17)	0.302(18)	0.3385(12)	O9	0.8082(4)	0.3865(4)	0.4659(4)
N4	0.156(17)	0.233(17)	0.1850(12)	N7	0.8277(3)	0.2806(4)	0.458(19)
C1	0.4892(2)	0.2547(2)	0.1033(16)	O10	0.494(18)	0.797(17)	0.322(14)
H1	0.465700	0.318500	0.0643000	O11	0.681(18)	0.640(17)	0.316(14)
C2	0.5275(3)	0.1290(2)	0.0788(18)	O12	0.6810(2)	0.827(18)	0.348(15)
H2	0.530100	0.108000	0.0243000	N8	0.618(19)	0.756(18)	0.328(13)
C3	0.5613(3)	0.0365(3)	0.1356(2)	O20	0.9608(9)	0.8488(8)	0.150(11)
H3	0.586800	-0.04920	0.1205000	H20A	0.9165(2)	0.9281(9)	0.124(15)
C4	0.5579(3)	0.0696(2)	0.2155(2)	H20B	0.893(13)	0.804(14)	0.1571(3)
H4	0.581400	0.006600	0.2549000	O21	0.080(16)	0.7565(8)	0.3353(7)

C5	0.5192(2)	0.1972(2)	0.2370(15)	H21A	0.0679(4)	0.722(11)	0.285(10)
C6	0.5070(2)	0.2433(2)	0.3225(15)	H21B	0.0257(4)	0.845(10)	0.335(15)
C7	0.5517(3)	0.1648(3)	0.3869(18)	O22	0.156(13)	0.6567(9)	0.0611(6)
H7	0.594800	0.077700	0.3783000	H22A	0.097(19)	0.7107(2)	0.1040(7)
C8	0.5324(3)	0.2158(3)	0.4638(19)	H22B	0.1722(3)	0.715(18)	0.019(11)
H8	0.562500	0.163800	0.5078000	O25	-0.086(4)	0.9919(3)	0.3347(2)
C9	0.4682(3)	0.3444(3)	0.4753(17)	H25	-0.01(12)	0.997(3)	0.304(16)
H9	0.452700	0.380500	0.5272000	C21A	-0.01(10)	0.954(11)	0.4061(5)
C10	0.4273(2)	0.4185(2)	0.4089(15)	H21C	-0.06970	0.979200	0.455500
H10	0.384900	0.505800	0.4166000	H21D	0.062200	0.994000	0.403400
C11	0.1582(2)	0.2061(2)	0.1059(17)	H21E	0.032500	0.862300	0.405800
H11	0.135900	0.273200	0.0690000	C21B	-0.140(7)	0.897(14)	0.378(17)
C12	0.1927(3)	0.0821(3)	0.0773(2)	H21F	-0.17970	0.928400	0.432100
H12	0.192800	0.065600	0.0222000	H21G	-0.06680	0.818900	0.381800
C13	0.2266(3)	-0.016(3)	0.1319(2)	H21H	-0.20920	0.882300	0.349000

Table 7.16 Bond distances (Å).

Fe1 – O14	1.7783(14)	C15 – C16	1.478(4)
Fe1 – O17	2.0207(11)	C16 – N3	1.345(3)
Fe1 – O18	2.0473(12)	C16 – C17	1.378(4)
Fe1 – O13	2.1068(10)	C17 – C18	1.375(5)
Fe1 – N2	2.1246(17)	O25 – C21B	1.453(9)
Fe1 – N1	2.1470(19)	C18 – C19	1.374(5)
C14 – C15	1.38400(4)	C19 – C20	1.364(4)
Fe2 – O14	1.7739(15)	C7 – C8	1.368(4)
Fe2 – O24	2.0429(10)	C20 – N3	1.333(3)
Fe2 – O16	2.0375(10)	C8 – C9	1.371(4)
Fe2 – O15	2.1155(12)	N5 – O1	1.219(3)
Fe2 – N3	2.1384(19)	N5 – O2	1.230(3)
Fe2 – N4	2.1627(18)	N5 – O3	1.244(3)
C1 – N2	1.33400(3)	N6 – O6	1.191(4)
C1 – C2	1.37400(3)	N6 – O5	1.209(3)
C15 – N4	1.34100(3)	N6 – O4	1.237(3)
C2 – C3	1.35100(4)	N7 – O9	1.128(5)
C13 – C14	1.37400(5)	N7 – O7	1.159(5)
C3 – C4	1.37000(4)	N7 – O8	1.176(5)
C12 – C13	1.36600(5)	N8 – O12	1.230(3)
C4 – C5	1.38100(3)	N8 – O10	1.235(3)
C11 – C12	1.38100(4)	N8 – O11	1.249(2)
C5 – N2	1.33800(3)	C9 – C10	1.369(4)
C5 – C6	1.48900(3)	C10 – N1	1.338(3)
C6 – N1	1.34800(3)	C11 – N4	1.341(3)
C6 – C7	1.37700(4)	O25 – C21A	1.478(7)

Table 7.17 Angles between the bonds (°)

O14 – Fe1 – O17	95.180(5)	C13 – C12 – C11	118.300(3)
O14 – Fe1 – O18	94.620(6)	C12 – C13 – C14	120.100(3)
O17 – Fe1 – O18	95.930(5)	C8 – C9 – C10	118.700(3)
O14 – Fe1 – O13	176.81(6)	C9 – C8 – C7	119.400(3)
O17 – Fe1 – O13	84.400(4)	C13 – C14 – C15	119.000(3)
O18 – Fe1 – O13	82.270(4)	C8 – C7 – C6	119.500(3)

O14 – Fe1 – N2	94.230(7)	C7 – C6 – C5	123.900(2)
O17 – Fe1 – N2	167.31(6)	N4 – C15 – C14	121.200(3)
O18 – Fe1 – N2	92.770(6)	N4 – C15 – C16	115.400(2)
O13 – Fe1 – N2	86.670(6)	C14 – C15 – C16	123.500(3)
O14 – Fe1 – N1	99.130(7)	N3 – C16 – C17	121.300(3)
O17 – Fe1 – N1	93.900(6)	N3 – C16 – C15	115.300(2)
O18 – Fe1 – N1	162.90(5)	C17 – C16 – C15	123.400(3)
O13 – Fe1 – N1	84.060(6)	C18 – C17 – C16	118.800(3)
N2 – Fe1 – N1	76.200(7)	C4 – C5 – C6	123.700(2)
C2 – C3 – C4	119.60(3)	C17 – C18 – C19	120.300(3)
N2 – C5 – C4	120.80(2)	C18 – C19 – C20	117.500(3)
N2 – C5 – C6	115.4(19)	N3 – C20 – C19	123.700(3)
N1 – C6 – C7	121.30(2)	C10 – N1 – C6	118.500(2)
N1 – C6 – C5	114.80(2)	C10 – N1 – Fe1	125.31(16)
N1 – C10 – C9	122.60(2)	C6 – N1 – Fe1	116.14(16)
O14 – Fe2 – O24	93.650(6)	C1 – N2 – C5	118.900(2)
O14 – Fe2 – O16	93.090(5)	C1 – N2 – Fe1	123.53(15)
O24 – Fe2 – O16	98.330(5)	C5 – N2 – Fe1	116.86(15)
O14 – Fe2 – O15	173.35(5)	C20 – N3 – C16	118.400(2)
O24 – Fe2 – O15	85.710(4)	C20 – N3 – Fe2	124.27(17)
O16 – Fe2 – O15	80.470(4)	C16 – N3 – Fe2	117.28(17)
O14 – Fe2 – N3	95.380(7)	C15 – N4 – C11	119.100(2)
O24 – Fe2 – N3	164.60(6)	C15 – N4 – Fe2	116.41(16)
O16 – Fe2 – N3	93.620(6)	C11 – N4 – Fe2	124.08(16)
O15 – Fe2 – N3	86.730(6)	O1 – N5 – O2	122.400(3)
O14 – Fe2 – N4	102.37(7)	O1 – N5 – O3	120.700(2)
O24 – Fe2 – N4	90.590(6)	O2 – N5 – O3	116.900(2)
O16 – Fe2 – N4	161.64(6)	O6 – N6 – O5	116.000(2)
O15 – Fe2 – N4	84.270(5)	O6 – N6 – O4	120.400(2)
N3 – Fe2 – N4	75.300(7)	O5 – N6 – O4	123.600(2)
N2 – C1 – C2	122.40(2)	O9 – N7 – O7	125.200(5)
N4 – C11 – C12	122.30(3)	O9 – N7 – O8	119.200(5)
O10 – N8 – O11	119.80(2)	O7 – N7 – O8	115.600(5)
C3 – C2 – C1	118.70(3)	O12 – N8 – O10	121.07(19)
C5 – C4 – C3	119.50(3)	O12 – N8 – O11	119.100(2)
Fe2 – O14 – Fe1	161.72(9)	C15 – N4 – C11	119.100(2)

C21B – O25 – C21A	74.00(12)

7.5.1 Powder X-ray Diffraction

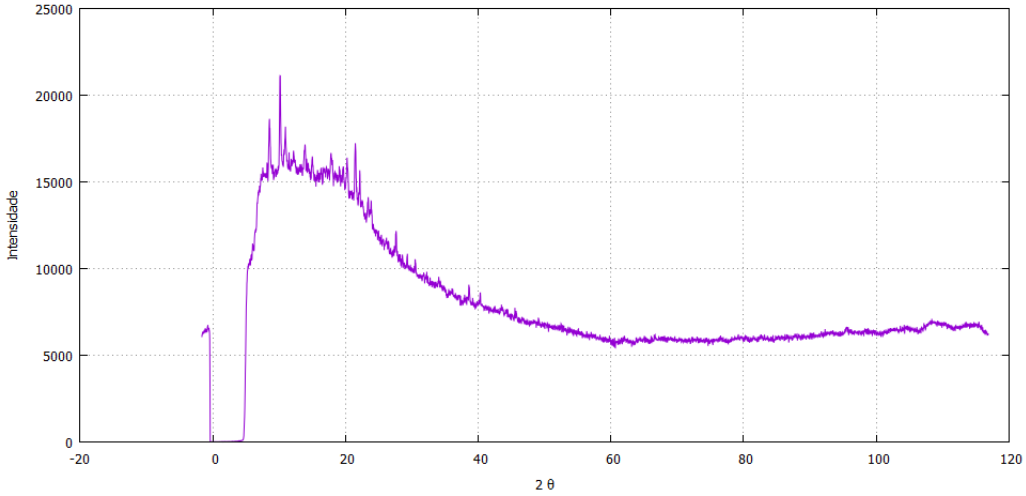

Fig. 7.37 Powder spectra of the oxo-bridged iron dimer.

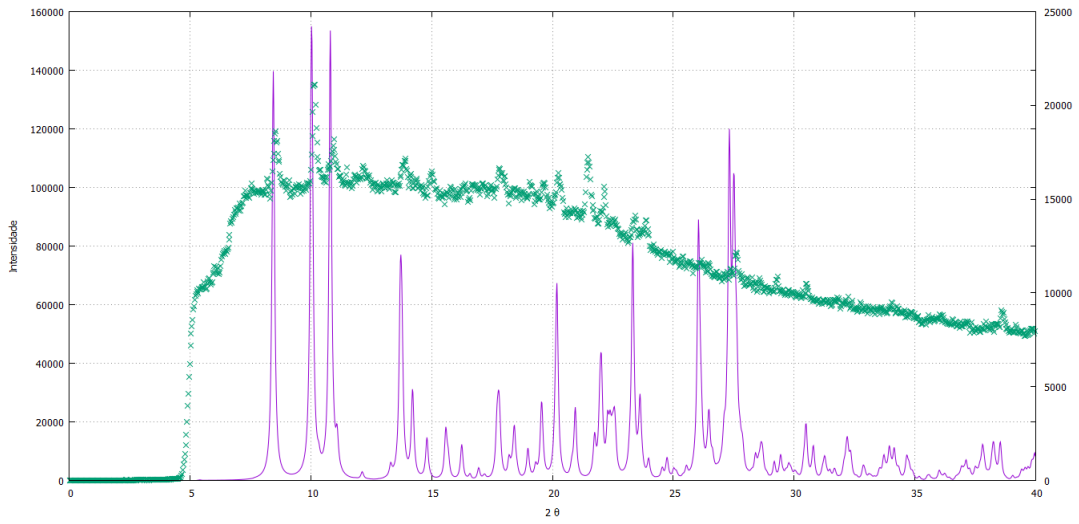

Fig. 7.38 Powder simulation diffractogram (purple) and experimental diffractogram (green) of the oxo-bridged iron dimer.

The experimental results are in agreement with the simulation of the powder diffractogram for single crystal data.

7.5.2 Magnetometry

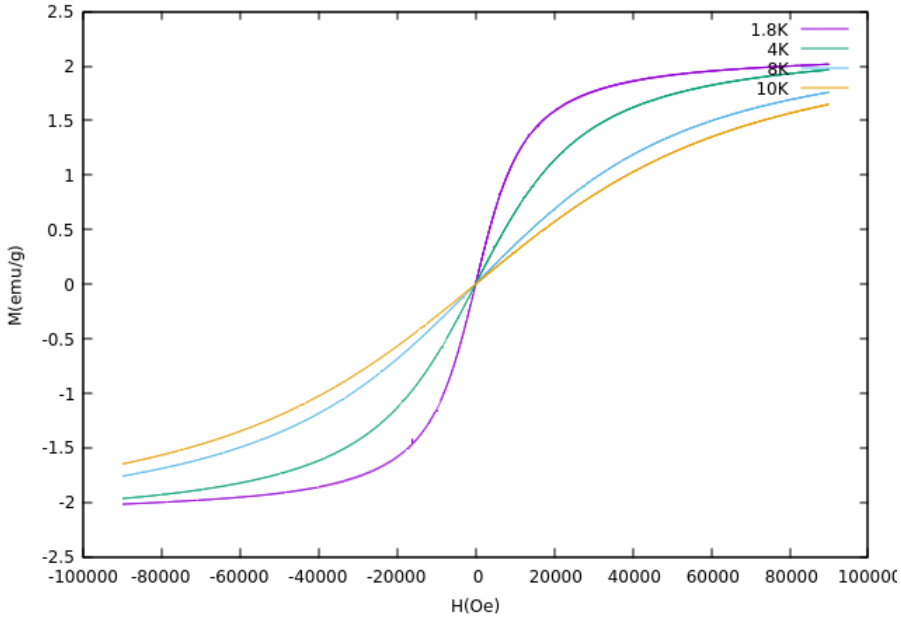

Fig. 7.39 Magnetization (emu/g) as function of field (Oe) at 1.8, 4, 8 and 10 K.

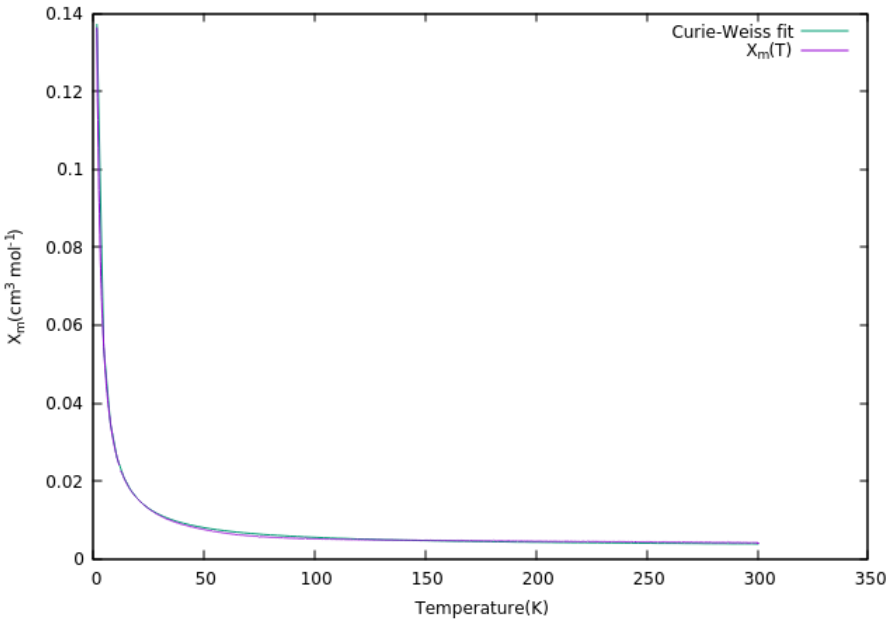

Fig. 7.40 Molar magnetic susceptibility ($cm^3\,mol^{-1}$) as function of temperature (K).

For high-temperatures (150 K − 300 K), it was used the Curie-Weiss fit. The sample has a strong antiferromagnetic behaviour and an effective magnetic moment of $6.3\mu_B$. Altough the

magnetic moment value is a little far from the interval $5.65 - 6.10$ it is still in agreement for Fe^{3+}, high spin. This is probably due to iron(III) nitrate, which is in excess.

7.5.3 Mössbauer Spectroscopy

The Mössbauer spectra shows two symmetric absorption peaks at 295 K and 4 K, which are fitted with a single quadrupole doublet. The estimated isomer shifts (IS), which corresponds to the metallic αFe at room temperatures, and the quadrupole splitting (QS) are consistent with Fe^{3+} having $S = \frac{5}{2}$ in an octahedral geometry coordinated by six oxygens [50]. A non-zero QS is observed due to the non-cubic charge distribution symmetry around the Fe cations. As QS does not vary with temperature, this means that there is no electronic contribution to the electrical field gradient, so a low-spin state for Fe^{3+} is unlikely. The increase of IS with decreasing temperature is explained by the second order Doppler shift. The estimated parameters are similar to those reported for Fe^{3+} in the $[Fe_3O(CNCH_2COO)_2(H_2O)_3] \cdot [NO_3] \cdot 5H_2O$ [51] as well as in $Fe_3(\mu_3 - O)$ trinuclear complexes [52–58].

Unlike most of these trinuclear complexes, no slowing down of the relaxation of the Fe^{3+} magnetic moments direction is observed down to 4 K, which suggests that the magnetic exchange interactions are weaker in the title compound. Estimated errors are $\leq 0.02\,\mathrm{mm\,s^{-1}}$ for IS and QS.

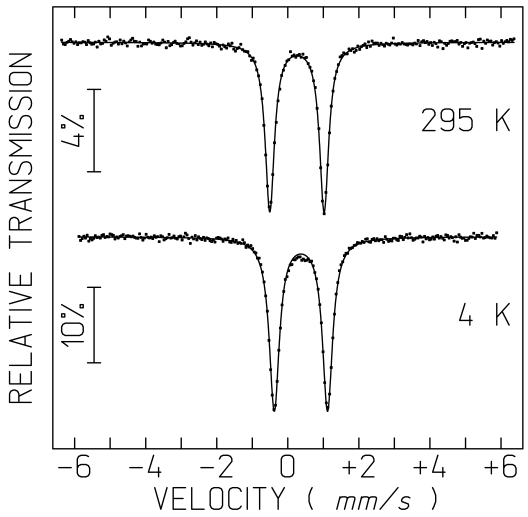

Fig. 7.41 Mössbauer spectra at 295 K and 4 K.

Table 7.18 Estimated parameters from the Mössbauer spectra.

T (K)	IS (mm/s)	QS (mm/s)
296	0.37	1.53
4	0.48	1.50

The magnetic properties displayed by μ-oxo-bis[bis(2,2'-bipyridyl-N,N'-triaqua-iron(III))] tetranitrate trihydrate methanol solvate, that is, the apparent absence of interaction between the neighbouring metal centers, are not in sync with those of similar compounds. In literature, one can find several examples of oxo-bridged dinuclear iron complexes with exchange integrals in the range $-J = 170 - 230\ cm^{-1}$, regardless of the $Fe - O - Fe$ geometry [22].

Chapter 8

Conclusion and Further Work

The initial plan for this thesis had to re-adapted during its execution due to a long-term malfunction of the single-crystal diffractometer, the main intended technique for detailed structural characterization. Also, the extreme difficulty of achieving expedite purchases of new reagents limited the synthetic activities to left-over reagents of the CFisUC research center.

Anyhow, despite the difficulties, the main goals of the project were attained. It was possible to study diverse metal complexes going from the synthesis to the magnetic properties. Amongst the hundreds of attempted syntheses, 4 compounds were selected for subsequent studies, containing pyridine, bipyridine or phenanthroline and Cu^{2+} or Fe^{3+}. One of the compounds has never been reported before and it will be the subject of a following manuscript, currently in preparation for submission. Different coordination geometries were found for the metal centers ranging from square pyramidal to octahedral. Distinct low dimension assemblings were also identified in the studied compounds: monomers, dimers and chains. An approximated rule was perceived for syntheses of the executed type, going from smaller (pyridine) to bulkier (phenanthroline) organic ligands, one achieves larger (1D-chains) to smaller (0D-monomers) molecular magnet dimensions.

For the catena-$CuPy_2Cl_2$, a strong antiferromagnetic interaction between the spin centers S=1/2 is clearly seen in the χ versus T dependence with a decrease at low temperatures. The exchange integral was extracted through a fitting with the Bonner-Fisher expression for equally spaced chains.

The structure of aqua-phenanthroline-trichloro iron(III) revealed the formation of monomers weakly bonded by intermolecular H-bonds. Surprisingly, a significant antiferromagnetic interaction is found in magnetic measurements of a polycrystalline sample. This ordering of the magnetic moments deserves a more thorough study: for instance, performing magnetic measurements in a oriented single-crystal to figure out the type of interaction within the solid

(easy axes, etc). In the synthetic level, substituting of the water molecule with another coordinating ligand without H donors, would be extremely interesting to see if the super-exchange is hindered.

Finally, the oxo-bridged iron dimer, did not show any significant magnetic interactions, at least, until the lowest temperature attained. This behaviour checked with VSM magnetometry and Mössbauer spectroscopy differs completely from that observed in similar compounds and a full explanation is still pursued.

In summation, the project performed over the last months allowed the investigation of the pysical properties of metallic complexes and fostered a rewarding opportunity to get acquainted to the methods and ways of modern scientific research.

References

[1] C. J. Jones. *d- and f- Block Chemistry*. The Royal Society of Chemistry, Great Britain, 2002.

[2] R. Chang. *Chemistry*. McGraw-Hill, New York, 2010.

[3] A. Mishra. *Transition Metals: Characteristics, Properties and Uses*. Nova Science Publishers, Inc., New York, 2012.

[4] N. Toshima and S. Hara. Gas Separation by Metal Complexes: Membrane Separations. *Encyclopedia of Separation Science*, pages 2933–2938, 2000.

[5] R. B. Chavan. Environmentally friendly dyes. *Handbook of Textile and Industrial Dyeing*, 1:515–561, 2011.

[6] V. Isaeva, V. Sharf, N. Nifant'ev, V. Chernetskii and Z. Dykh. Preparation of the Metal Complex Catalysts Immobilized on Chitosan for Carbonyl Compounds Transfer Hydrogenation. *Studies in Surface Science and Catalysis*, 118:237–243, 1998.

[7] Professor S. Al-Malaika, Dr. F. Axtell, Professor R. Rothon and Professor M. Gilbert. Additives for Plastics. *Brydson's Plastics Materials*, pages 127–168, 2017.

[8] I. Ott. Medicinal Chemistry of Metal N-Heterocyclic Carbene (NHC) Complexes. *Inorganic and Organometallic Transition Metal Complexes with Biological Molecules and Living Cells*, pages 147–179, 2017.

[9] L. Valade and C. Vaulmann. *Conductive Materials Based on M(dmit)2 Complexes and Their Combination with Magnetic Complexes*, volume 27. Springer, 2009.

[10] H. Tamaki, Z. J. Zhong, N. Matsumoto, S. Kida, M. Koikawa, N. Achiwa, Y. Hashimoto, and H. Okawa. Design of metal-complex magnets. Syntheses and magnetic properties of mixed-metal assemblies NBu4[MCr(ox)3]x (NBu4+ = tetra(n-butyl)ammonium ion; ox2- = oxalate ion; M = Mn2+, Fe2+, Co2+, Ni2+, Cu2+, Zn2+). *J. Am. Chem. Soc.*, 114(18):6974–6979, 1992.

[11] P. W. Atkins, T. L. Overton, J. P. Rourke, M. T. Weller and F. A Armstrong. *Inorganic Chemistry*. Oxford University Press, Great Britain, 2010.

[12] Prateek Jha. Dipole Moment and Its Applications, 2017. https://www.toppr.com/bytes/dipole-moment-and-applications/. [Online; accessed 2018-08-13].

[13] Compound Interest. Colours of Transition Metal Ions in Aqueous Solution, 2014. http://www.compoundchem.com/2014/03/05/colours-of-transition-metal-ions-in-aqueous-solution/. [Online; accessed 2018-08-13].

[14] R. H. Crabtree. *The Organometallic Chemistry of the Transition Metals*. John Wiley & Sons Inc., New Jersey, 2014.

[15] S. Blundell. *Magnetism in Condensed Matter*. Oxford University Press, Great Britain, 2001.

[16] C. Suryanarayana and M. G. Norton. *X-Ray Diffraction: A Practical Approach*. Springer Science, New York, 1998.

[17] C. Giacovazzo, H. L. Monaco, D. Viterbo, F. Scordari, G. Gilli, G. Zanotti and M.Catti. *Fundamentals of Crystallography*. Oxford University Press, New York, 1992.

[18] A. L. Spek T. R. Schneider P. Müller, R. Herbst-Irmer and M. R Sawaya. *Crystal Structure Refinement: A Crystallographer's Guide to SHELXL*. Oxford University Press, New York, 2006.

[19] J. Coey. *Magnetism and Magnetic Materials*. Cambridge University Press, New York, 2009.

[20] H. D. Young. *University Physics*. Addison Wesley, California, 8th edition, 1992.

[21] M. Getzlaff. *Fundamentals of Magnetism*. Springer-Verlag, Berlin, 2008.

[22] O. Khan. *Molecular Magnetism*. VCH Publishers, Inc., New York, 1993.

[23] A. Magalhães. Compostos de Cobre(II) de Baixa Dimensão com Ácidos Carboxílicos como Ligandos. Master's thesis, Coimbra University, Department of Physics, 2011.

[24] N. W. Ashcroft and N.D. Mermin. *Solid State Physics*. Harcourt, Inc., Florida, 1976.

[25] Bruker Advanced X ray Solutions. *APEX 2 Version 2: User manual*. Bruker AXS Inc., 2006.

[26] J. Da Silva. Estudo do Fosfito de Betaína por Métodos de Difração de Raios-X. Master's thesis, Coimbra University, Department of Physics, 1998.

[27] V. K. Pecharsky and P. Y. Zavalij. *Fundamentals of Powder Diffraction and Structural Characterization of Materials*. Springer Science, New York, 2009.

[28] P.S.P Da Silva. *Atropisomerismo em Compostos de Difenilguanidina: Estudo Estrutural por Difracção de Raios-X*. PhD thesis, Coimbra University, Department of Physics, 1999.

[29] *Physical Property Measurement System: DynaCool User's Manual*. California, 1 edition, 2011.

[30] M. Henriques. Synthesis and Characterisation of FeSe Superconductors. Master's thesis, Coimbra University, Department of Physics, 2015.

[31] A. Zieba and S. Foner. *Detection Coil, Sensitivity Function and Sample Geometry Effects For Vibrating Sample Magnetometers*. Review of Scientific Instruments, 1982.

[32] D. Jiles. *Introduction to Magnetism and Magnetic Materials*. Thomson Press, New Delhi, 1991.

[33] G. J. Long, T. E. Cranshaw and G. Longworth. The Ideal Mössbauer Effect Absorber Thicknesses. *Mossb. Effect. Ref. Data J.*, 6:42–49, 1983.

[34] J. C. Waerenborgh, D. P. Rojas, A. L. Shaula, G. C. Mather, M. V. Patrakeev, V. V. Kharton and J. R. Frade. Phase Formation and Iron Oxidation State in $SrFe(Al)O_{3-\delta}$ perovskites. *Mater. Lett.*, 59:1644–1648, 2005.

[35] Sobarwiki. *Schematic of UV-visible Spectrophotometer*. 2013.

[36] *Deuterium Tungsten-Halogen Calibration Light Source: Installation and Operation Manual*. Ocean Optics, Inc., Florida, 2009.

[37] A. Speck. *PLATON - A Mulipurpose Crystallographic Tool*. Utrecht University, 1999.

[38] G. Murphy, C. Murphy, B. Murphy and B. Hathaway. Crystal Structures, Electronic Properties and Structural Pathways of two $[Cu(phen)_2(OH_2)][Y]_2$ complexes (phen = 1,10-phenanthroline, Y = $[CF_3SO_3^-]$ or ClO_4^-). *J. Chem. Soc., Dalton Trans.*, 1997.

[39] Mahmoud Naim. Coordination Numbers of Inorganic Compounds, 2017. https://uomustansiriyah.edu.iq/media/lectures/6/6_2017_11_04!07_05_55_PM.pdf/. [Online; accessed 2018-09-01].

[40] YanA at English Wikipedia. Trigonal bipyramidal CFT splitting, 2007. https://commons.wikimedia.org/wiki/File:Trigonal_bipyramidal.png/. [Online; accessed 2018-09-01].

[41] YanA at English Wikipedia. Square pyramidal CFT splitting, 2007. https://commons.wikimedia.org/wiki/File:Square_pyramidal.png/. [Online; accessed 2018-09-01].

[42] J. D. Dunitz. The Crystal Structures of Copper Dipyridine Dichloride and the Violet Form of Cobalt Dipyridine Dichloride. *Acta Cryst.*, 10:307–313, 1957.

[43] B. Morosin. Structure Refinements on dichloro- and dibromobis(pyridine)copper(II). *Acta Cryst.*, B31:632–634, 1975.

[44] P. M. Richards, D. L. Strandburg, W. Duffy, Jr. and J. E. Venneman. Magnetic and thermal studies of antiferromagnetic linear chains in dichlorobis(pyridine)copper(II). *Physical Review B*, 9(5):2220–2227, 1974.

[45] YanA at English Wikipedia. Octahedral CFT splitting, 2008. https://commons.wikimedia.org/wiki/File:Octahedral_crystal-field_splitting.png/. [Online; accessed 2018-09-01].

[46] J. Simon, W. S. Bakr, R. Ma, M. E. Tai, P. M. Preiss and M. Greiner. Quantum Simulation of Antiferromagnetic Spin Chains in an Optical Lattice. *Nature*, 472:307–312, 2011.

[47] J. M. Patrick, B. W. Skelton, A. H. White and P. C. Healy. Structural Studies in the Iron(III)/Chloride/α,α'-Diimine System. The Six-Coordinate Mononuclear fac-[$FeCl_3$(phen)X] System, X = MeOH, H_2O, Cl^-. *Aust. J. Chem.*, 36:2031–2041, 1983.

[48] Chemistry Socratic. Which transition metal can form both a high and low spin complex?, 2016. https://socratic.org/questions/5666dcbe581e2a2d1d3f1adf/. [Online; accessed 2018-09-01].

[49] W. M. Reiff, E. H. Witten, J. Takacs, J. H. Zhang and C. C. Torardi. Novel motifs for magnetic exchange interactions as exemplified in one dimensional magnets based on the $FeCl_3$-α-di-imine system: Nuclear gamma resonance evidence of slow paramagnetic relaxation and 3D-ordering. *Hyperfine Interactions*, 56:1723–1728, 1990.

[50] N.N. Greenwood and T.C. Gribb. *Mössbauer Spectroscopy*. Chapman and Hall, London, 1971.

[51] S. Shova, I. Kadelnik, F. Zhovomir, I. Bulgak, V. Bel'skii and K. Turte. Synthesis and Study of a Trinuclear Complex of Iron (III) with Cyanoacetic Acid. *Russian Journal of Coordination Chemistry C/C Koordinatsionnaia Khimiia*, 23:629–635, 1997.

[52] A. K. Boudalis, Y. Sanakis, C. P. Raptopoulou, A. Terzis, J. P. Tuchagues and S. P. Perlepes. A Trinuclear Cluster Containing the $[Fe_3(\mu_3-O)]^{7+}$ Core: Structural, Magnetic and Spectroscopic (IR, Mössbauer, EPR) Studies. *Polyhedron*, 24:1540–1548, 2005.

[53] M. François, M. I. Saleh, P. Rabu, M. Souhassou, B. Malaman and J. Seteinmetz. Structural Transition at 225 K of the Trinuclear Fe(III) Heptanoate $[Fe_3O(O_2CC_6H_{13})_6(H_2O)_3]NO_3$. *Solid State Sciences*, 7:1236–1246, 2005.

[54] L. N. Mulay and G. H. Ziegenfuss. Exchange Interactions in Isolated Trinuclear Clusters of Fe^{3+}: Magnetic and Mössbauer studies. *AIP. Conf. Pres.*, 24:213–214, 1975.

[55] D. Pinero, P. Baran, R. Boca, R. Herchel, M. Klein, R. G. Raptis, F. Renz and Y. Sanakis. A Pyrazolate-Supported $Fe_3(\mu_3-O)$ Core: Structural, Spectroscopic, Electrochemical and Magnetic Study. *Inorg. Chem.*, 46:10981–10989, 2007.

[56] M. R. Silva, J. Coutinho, L.C.J. Pereira, P. Martín-Ramos and J. C. Waerenborgh. Magnetic Coupling through Cyanoacetate Bridges: Synthesis, Structure and Physical Properties of two Low Dimensional Compounds. *Spectrochimica Acta A.*, 172:9–13, 2017.

[57] M. R. Silva, L.C.J. Pereira, J. C. Waerenborgh, J. N. J. Nogueira, P. A. O. Silva and C. Yuste-Vivas. Oxo-Bridged Trinuclear Fe(III) Complexes: Structural and Magnetic Properties. *Solid State Phenomena*, 194:162–170, 2013.

[58] C. P. Raptopoulou, V. Tangoulis and V. Psycharis. Synthesis and Structural, Spectroscopic and Magnetic Characterization of $(NH_4)[Fe_3(\mu_3-OH)(H_2L)_3(HL)_3]$ (H_3L = Orotic Acid) Presenting Two Novel Metal-Binding Modes of the Orotate Ligand: The case of a Spin-Frusted System. *Inorg. Chem.*, 39:4452–4459, 2000.

Appendix A

1,2-bis(4-pyridinium) ethylene dinitrate

During the X-ray diffraction experiments, one of the samples was crystalline but only the salt crystallized. The ligand used was 1,2-Di (4-pyridyl) ethylene ($C_{12}H_{10}N_2$) and the solvents were distilled water (H_2O), methanol (CH_3OH) and nitric acid (HNO_3).

It was possible to determine and refine the crystal structure using the SHELXS-97 and the SHELXL-97 program. The PLATON program [37] analyzed the structure and provided the images of the molecule. In the following tables and images, the crystal characteristics are presented, since it is interesting that this molecule was not found in the database.

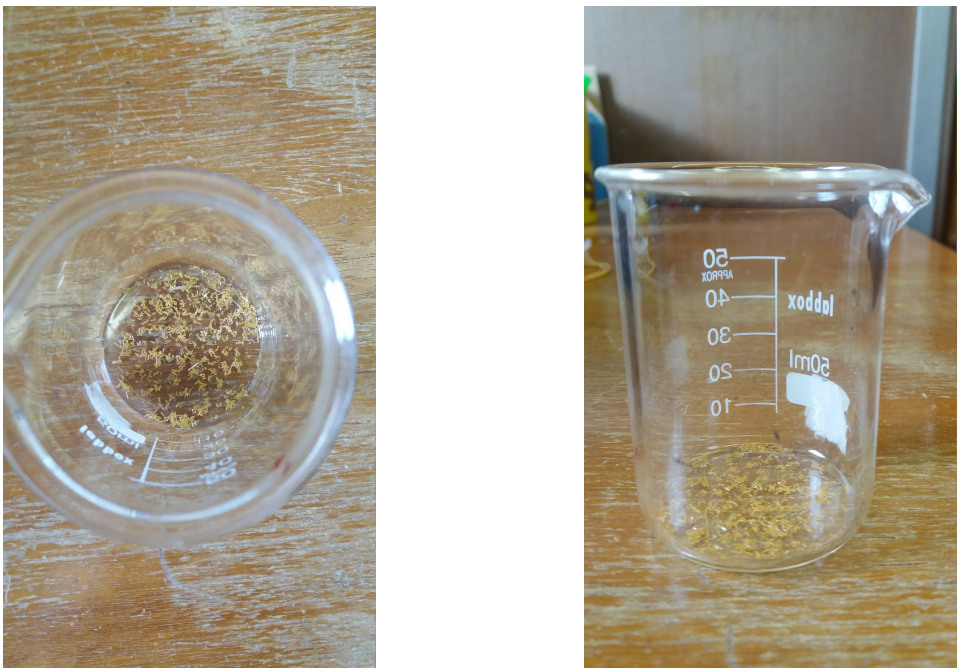

Fig. A.1 Crystals of 1,2-bis(4-pyridinium) ethylene dinitrate.

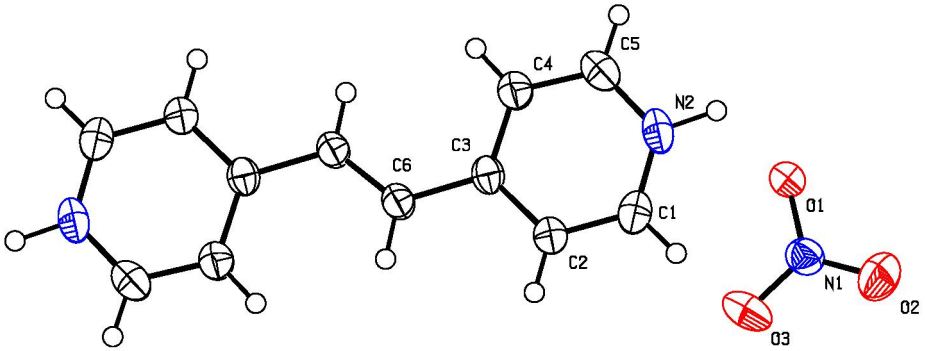

Fig. A.2 Representation of the molecule in the PLATON program.

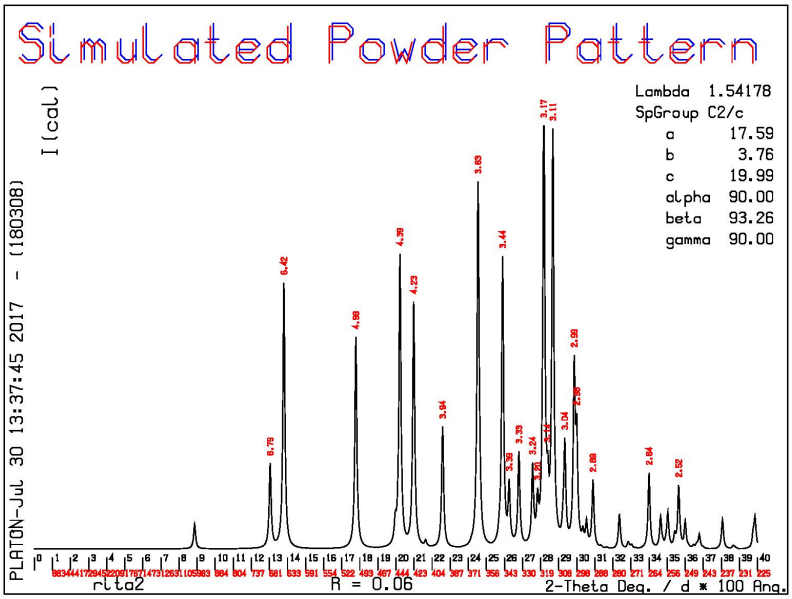

Fig. A.3 Powder spectra simulation of 1,2-bis(4-pyridinium) ethylene dinitrate.

Table A.1 Data collection, refinement and crystal parameters of 1,2-bis(4-pyridinium) ethylene dinitrate.

Compound	$C_6H_6N_2O_3$
Molecular Weight (g/mol)	246
Temperature (K)	154.13
Lattice Type	Monoclinic
Space Group	C2/c
Crystal Data (Å)	
a	17.5875(14)
b	3.76420(3)
c	19.9879(15)
α	90°
β	93.261° (3°)
γ	90°
Cell Volume (Å^3)	1321.11(18)
Z	8
Density (g/cm^3)	1.5498(2)
μ (MoK_α) (mm^{-1})	0.127
Diffractometer	Bruker APEX II CCD
h interval	-20 < 20
k interval	-4 < 3
l interval	-21 < 24
θ interval	2.04° < 25.63°
Number of reflections	1252
Number of refined parameters	100
Minimum Density (e^-Å^{-3})	-0.604
Maximum Density (e^-Å^{-3})	0.562
χ^2	1.044
R [I > 2σ(I)]	0.0362
wR^2 [I > 2σ(I)]	0.0916

Table A.2 Bond distances (Å).

N2 – C1	1.333(2)
N2 – C5	1.338(2)
C1 – C2	1.367(2)
C2 – C3	1.395(2)
C3 – C4	1.399(2)
C3 – C6	1.461(2)
C4 – C5	1.366(2)
C6 – C6	1.327(3)
O1 – N1	1.26(17)
N1 – O3	1.24(18)
N1 – O2	1.24(18)

Table A.3 Angles between the bonds (°).

C1 – N2 – C5	121.84(14)
N2 – C1 – C2	119.68(15)
C2 – C3 – C4	117.54(14)
C2 – C3 – C6	119.53(14)
C4 – C3 – C6	122.92(14)
N2 – C5 – C4	120.81(16)
C6 – C6 – C3	125.09(18)
O3 – N1 – O2	121.39(14)
O3 – N1 – O1	119.05(14)
O2 – N1 – O1	119.55(14)

Table A.4 Atomic coordinates and displacement parameters (Å^2).

Atom	x	y	z	U_{iso}
N2	0.34189(8)	0.7754(4)	0.16970(7)	0.0391(4)
C1	0.31239(9)	0.8660(4)	0.10920(8)	0.046000
H1	0.2647000	0.9729000	0.1046000	0.046000
C2	0.35257(9)	0.8010(4)	0.05391(8)	0.0348(4)
H2	0.3320000	0.8643000	0.0117000	0.042000
C3	0.42415(8)	0.6407(4)	0.06014(7)	0.0298(4)
C4	0.45255(9)	0.5486(4)	0.12463(8)	0.0366(4)
H4	0.4999000	0.440300	0.1310000	0.044000
C5	0.4100(10)	0.6190(5)	0.17820(8)	0.0417(4)
H5	0.4287000	0.557500	0.2211000	0.050000
C6	0.46586(9)	0.5749(4)	0.00024(7)	0.0321(4)
H6	0.4428000	0.643300	-0.040800	0.039000
O1	0.20436(6)	0.3022(4)	0.20087(5)	0.0455(4)
N1	0.15133(8)	0.4221(4)	0.16255(7)	0.0376(4)
O2	0.09506(7)	0.5597(4)	0.18679(7)	0.0603(4)
O3	0.15623(8)	0.3974(4)	0.10120(6)	0.0636(4)
H2	0.3160(13)	0.8150(6)	0.2110(12)	0.0710(6)

Table A.5 Displacement parameters of the atoms (Å^2).

Atom	U_{11}	U_{22}	U_{33}	U_{23}	U_{13}	U_{12}
N2	0.0404(8)	0.0442(8)	0.0344(8)	-0.0055(6)	0.0156(6)	-0.0045(6)
C1	0.0319(8)	0.0417(9)	0.043(10)	-0.0039(8)	0.0095(7)	-0.0003(7)
C2	0.0334(9)	0.0399(9)	0.0314(9)	0.00100(7)	0.0052(7)	0.00220(7)
C3	0.0326(8)	0.0272(8)	0.0302(8)	-0.0016(6)	0.0068(6)	-0.0028(6)
C4	0.0367(9)	0.0403(9)	0.0332(9)	-0.0006(7)	0.0052(7)	0.00420(7)
C5	0.0495(10)	0.0468(10)	0.0239(9)	0.00050(7)	0.0050(7)	-0.0027(8)
C6	0.0348(8)	0.0350(9)	0.0270(8)	-0.0011(6)	0.0053(6)	0.00070(6)
O1	0.0363(6)	0.0714(9)	0.0288(6)	0.00420(6)	0.0021(5)	0.00890(6)
N1	0.0381(8)	0.0411(8)	0.0334(8)	0.00460(6)	0.0013(6)	-0.0035(6)
O2	0.0459(8)	0.0705(10)	0.0652(9)	0.00420(7)	0.0091(7)	0.01970(7)
O3	0.0741(10)	0.0881(11)	0.0280(7)	0.00730(7)	-0.003(6)	0.00600(8)